GRAIN BOUNDARIES OF NANOPHASE MATERIALS

Thesis by

Hao Ouyang

In Partial Fulfillment of the Requirements
for the Degree of
Doctor of Philosophy

California Institute of Technology
Pasadena, California
1993
(Defended October 12, 1992)

To my parents

Acknowledgements

It is my pleasure to thank all the people who have contributed to my education.

I gratefully acknowledge the help and advice of my advisor, Professor Brent Fultz, including grammatical and scientific corrections to this thesis. His genuine interest in science and seemingly endless store of ideas greatly facilitated my studies at Caltech.

I would like to thank the past and present Fultz's group, especially the visiting Professor H. Kuwano, Z. Gao, Dr. Douglas Pearson, Lawrence Anthony, James Okamoto and Tab Stephens for their help and friendship and for making my stay in this country unforgettable.

I am indebted to other members of the Caltech community, most notably Professor Bill Johnson and his group.

A special acknowledgement goes to Professor Sanboh Lee for introducing me to his research programs. His guidance and encouragement throughout my undergraduate years have helped me greatly.

I am also grateful to Dr. Channing Ann for generously sharing his research experience and for the stimulating discussions we have had.

I would also like to thank Carol Garland for her technical assistance.

Special thanks go to my officemates Dr. Douglas Pearson and Dave Lee for helping me understand American culture.

I am deeply grateful to Pha-Ping Lo, Wern-Jeng Yaur and Ijan Yeh for their friendship and fruitful suggestions.

My sincere thanks goes to my sister, Wen Ouyang, for her invaluable assistance.

Most of all, I would like to dedicate this thesis to my parents, especially my mother. Without her, none of this would have been possible.

This work was largely supported by the NSF-funded Caltech MRG under grant DMR-8811795. Upon termination of the MRG, support was provided by a Grant for International Research from NEDO, Japan. Further support was provided by a Presidential Young Investigator award No. DMR-8858226. Support for some of the laboratory work was provided by the U. S. Department of Energy under contract DE-FG03-86ER45270, and the U.S. DoE URIP equipment grant No. DE-FG05-89ER75511.

Abstract

Several iron alloys with nanometer-scale grain sizes were prepared by mechanical attrition in a high energy ball mill. Mössbauer spectrometry was used to measure the internal hyperfine magnetic fields. X-ray diffractometry (XRD) and transmission electron microscopy (TEM) were used to measure the grain size. The proposed structures of nanophase materials consist of two components of comparable volume fractions: a crystalline component and an interfacial component. By correlating features in the Mössbauer spectra to the structural results of XRD and TEM, we identified the hyperfine magnetic fields of ^{57}Fe atoms at grain boundaries. Once identified, the fractions of ^{57}Fe atoms at grain boundaries were determined by the intensities of their magnetic signatures seen in Mössbauer spectra. With data on the fraction of ^{57}Fe atoms at grain boundaries versus grain size, a model of the microstructure can be used to obtain the average width of the grain boundaries. Data from the model were obtained by Monte Carlo simulations. The average grain boundary widths of the fcc alloys Fe-Mn and Ni-Fe are approximately 0.5 nm, but the average widths of grain boundaries in the bcc alloys Cr-Fe and Fe-Ti are larger, approximately 1 nm.

The Debye temperature is a physical parameter of the vibrational spectrum of the solid. The difference in the Debye temperatures between the grain boundaries and the crystalline regions was found. The Debye temperature of the crystallites in nanophase Cr-Fe is 470 K, which is larger than that of grain boundary component, 370 K.

Table of Contents

List of Figures

List of Table

Chapter 1 Introduction

This chapter serves as an introduction to the thesis. In § 1.1 an introduction to nanophase materials is presented. In § 1.2 a description of the method by which the nanophase materials were synthesized is presented. The motivation of this work is discussed in § 1.3.

1.1 Nanophase Materials

Nanophase materials (1-5) are polycrystals with crystal sizes of a few nanometers. These materials with nanometer-sized features have been proposed as materials with a high density of defects, predominantly incoherent interfaces. Nanophase materials are characterized by a high degree of metastability and an atomic structure which is primarily controlled by the structure in the core of the interfaces (Fig. 1.1). The volume fraction of grain boundaries is comparable to that of the crystallites. The boundary core regions are characterized by a reduced atomic density and interatomic spacings deviating from the ones in the perfect lattice. The physical reason for the reduced density and non-lattice spacings between the atoms in the boundary cores is the misfit between the crystal lattices of different orientation joined along common interfaces or boundaries. Even though crystalline material may be in a low energy state, the grain boundaries account for a significant volume fraction of the total material and much of the misfit energy is located in these grain boundaries. A nanophase material may therefore lie far from its state of thermodynamic equilibrium.

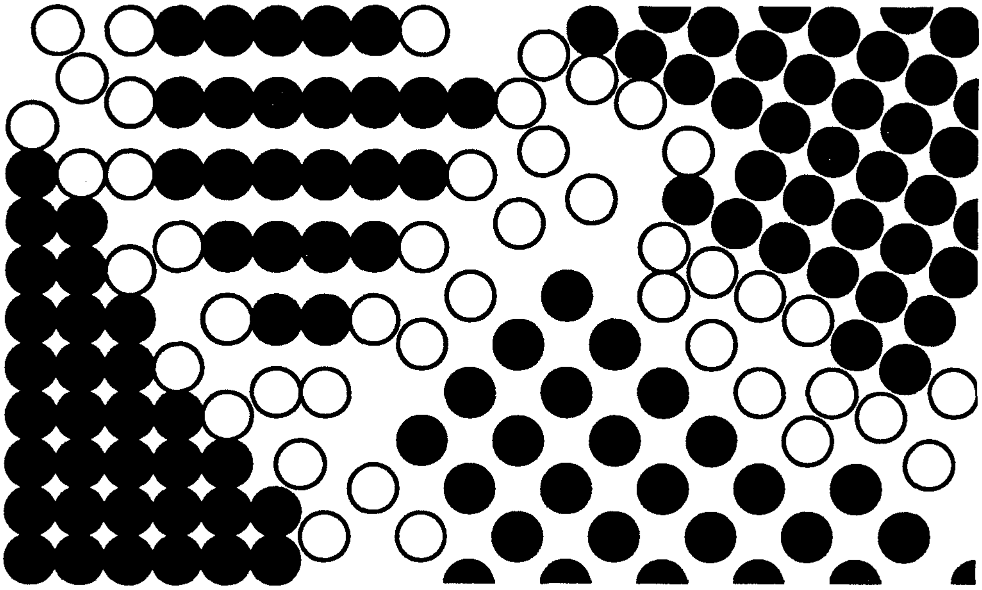

Figure 1.1. Schematic representation of a nanocrystalline metal distinguishing between the atoms associated with the individual crystal grains (filled circles) and those constituting the boundary network (open circles). (5)

Experimental studies of microstructure of nanocrystalline materials have been carried out by means of x-ray diffraction (2,6), transmission electron microscopy (7-8), neutron diffraction (9-10), EXAFS (3), differential scanning calorimetry (11), Auger electron spectroscopy, mass spectroscopy, x-ray fluorescence, positron lifetime spectroscopy, Mössbauer spectroscopy (12-14), hydrogen absorption, Raman spectroscopy (15), and so on. Reviews of these instruments are presented in references (5, 16-17).

Nanocrystalline materials are considered to comprise of two structural components: crystallites with long range translational order ,and the disordered interfacial component representing the variety of atomic spacings in the different types of interfaces (1). A structure of similar heterogeneity is not formed in disordered solids such as glasses. However, early ideas of a highly disordered, "gas-like" structure at interfaces or grain boundaries (1-5) have not been confirmed by more recent diffraction studies (6) or high resolution transmission electron microscopy (HREM) studies of fcc materials (7, 16, 18-19). The results from HREM must be interpreted with great care, however. For example, the influence of the high-energy electron beam on the shape and stability of the interfaces is uncertain. Since thin specimens are required for HREM, the crystal structure of a bulk nanophase specimen may be distorted during specimen preparation. This process might change the grain boundary structure as it alters the forces between neighboring crystals and induces new forces due to the energy of the free surface of the thin film specimen (17). Furthermore, because of high diffusivity in nanocrystalline materials (20), atoms may diffuse from the free surface of a thin specimen into the grain boundaries during sample preparation. This phenomena could also lead to the change of grain boundary structure. Results from HREM have a built-in bias. To see a grain boundary in high resolution, crystallites on both sides of the boundary must be properly oriented. Therefore, only special grain boundaries can be studied by the HREM.

Even though there are different arguments about the fundamental structure of grain boundary regions, the structures between boundaries and perfect lattices are still different (8). Due to the structural difference between nanometer-sized material and conventional polycrystalline material (CPM), it is not surprising to learn that the properties of nanocrystalline material are different from those of CPM. The novel characteristics include, for example, anomalously high diffusivity, enhanced solid solubility, excess specific heat (11,21), improved hardness and fracture stress (17,22), supermodulus (17), lower Debye temperature (12-13), and different magnetic properties (23-24). The details are discussed in references (5, 20, 25).

1.2 Mechanical Attrition/ Alloying

To date, the synthesis of nanocrystalline materials has been carried out in several ways. The most frequent method is to assemble pre-generated small clusters by means of in-situ consolidation and sintering (5). However, in our work, we mainly employed mechanical attrition to prepare nanocrystalline materials. Little effort was spent on sample preparation by vapor evaporation.

More than ten years ago, ball milling was developed by Benjamin as a way to overcome the limitations of conventional alloying (26). In mechanical alloying, a suitable amount of powder particles is placed in a high-energy mill with a convenient grinding medium (usually hardened steel balls). During this metallurgical process, the powder materials are trapped by colliding steel balls and repeatedly deformed, cold welded and fractured (Fig. 1.2). Refinement of the microstructure is approximately a logarithmic function of time (27), and depends on the mechanical energy input to the process and the work hardening of materials being processed. This so-called mechanical alloying process is mainly used to combine materials otherwise immiscible, e.g., dispersion-hardened superalloys or other metal-ceramic composites (26,28), which are not easy to produce by conventional techniques due to their high melting temperature, or very high reactivity (28). A few years ago it was shown that it is possible to produce amorphous metals by mechanical alloying (29-32). In the course of studying crystal-amorphous transformations during ball milling, formation of nanocrystalline metals, and nanocrystalline intermetallic compounds were reported (33-36). However, there is still little understanding about the fundamental process of mechanical alloying (28). Therefore, it is hard to analyze and predict this process in a quantitative way.

Usually there are three types of ball milling (26,28): (a) attritor, which contains hardened balls driven by a central impeller shaft (37). Moderate volumes of powder can be alloyed in this device in moderate milling times. (b) SPEX vibratory (or shaker) mill, which contains grinding balls (in our case two with 0.25 inch diameter and two with 0.50 inch diameter). The device is vibrated at a high frequency involving motion in three orthogonal directions, but the vibrating amplitude is largest in one direction. It can produce small volumes of powder (several grams) in short ball milling times. (c) Conventional horizontal ball mill, which is a large device producing large volumes of powder in long ball milling times. In our work, only the vibratory mill is employed (Figure. 1.3). This shaker mill (SPEX 8000 mixer/mill) can produce enough powder (usually around 5 grams) in reasonably short times (maybe an hour or a day, depending on the final

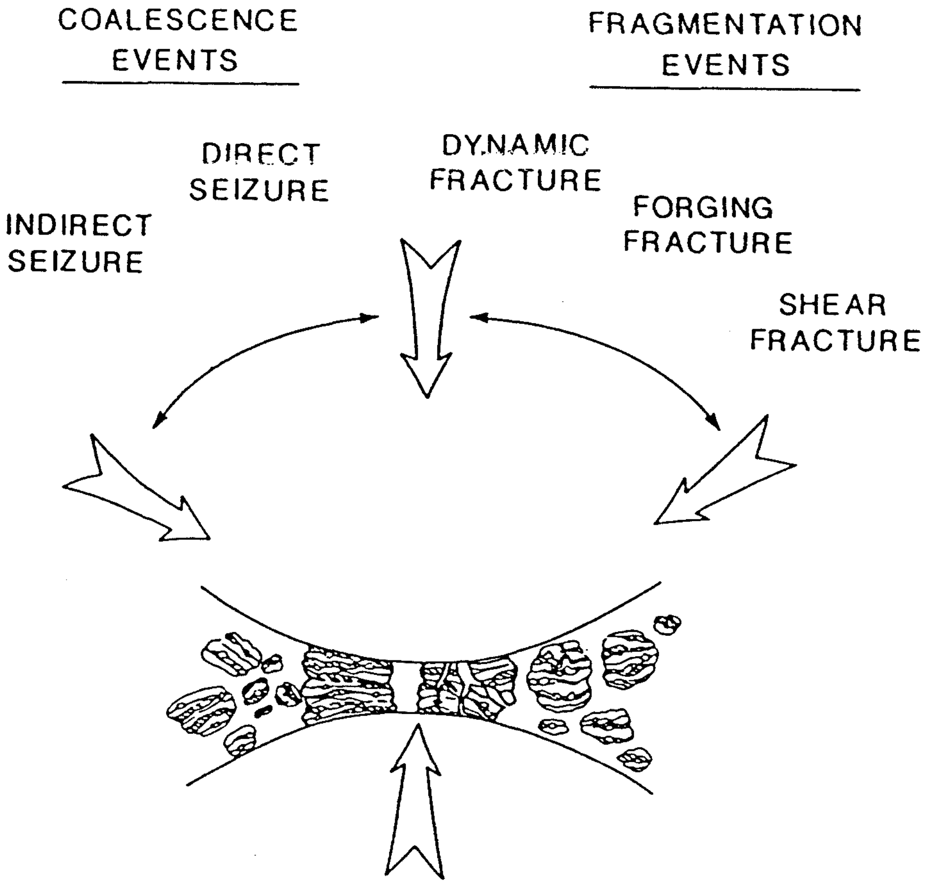

Figure 1.2. The illustration (37) schematizes the repeated fragmentation and coalescence processes characteristic of mechanical alloying. The lettering indicates the various kinds of these events that can be imagined to occur, as these processes depend on the impact angle of the samples and balls.

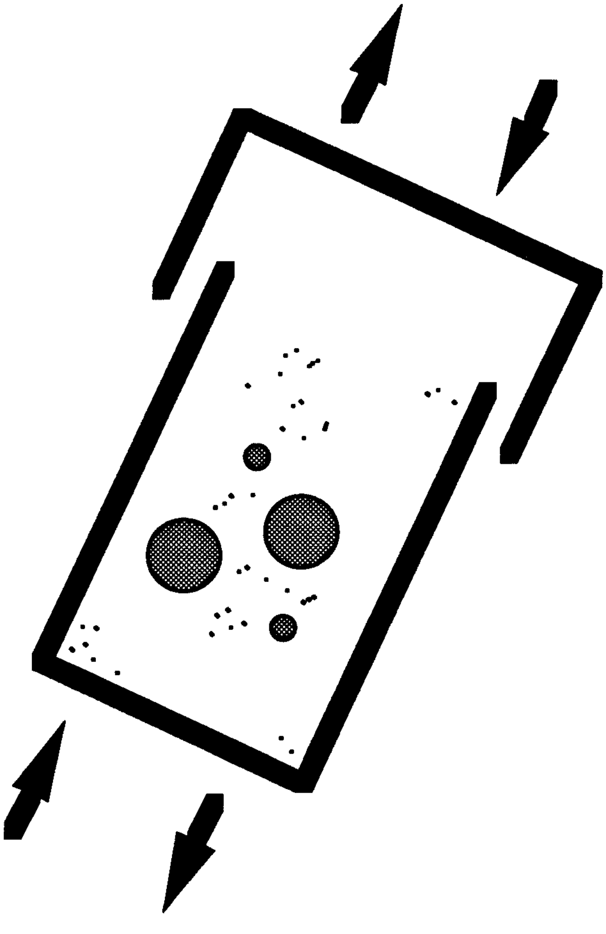

Figure 1.3. Schematic drawing of a vibratory mill.

conditions achieved for our microstructural studies). Qualitatively the synthesis of nanocrystalline materials can be described as followed: during mechanical ball milling, the deformation of powders is localized at the early stage in shear bands with a thickness of about 1 μm (31,33). Nanometer-sized grains are nucleated within these shear bands. For longer times of ball milling, this process results in an extremely fine-grained microstructures with randomly oriented grains separated by high angle grain boundaries. The major advantage of this method for producing nanocrystalline materials is that it is a mass production process. It is much quicker and easier than the gas condensation method, in particular. Ball milling can synthesize several grams of material in tens of hours.

1.3 Motivation

There are many models of grain boundary structure (38-40). A grain boundary can be defined as the accommodation area between crystallites with a high specific energy. Therefore, to minimize energy we expect the grain boundary width to be constrained to some value. In this work, we sought to investigate the relationship between grain boundary width and crystal structure. However, the atomic structure of grain boundary is known to depend on the orientation relationship between adjacent crystals and the interface inclination. If the crystallites are oriented at random, all of the grain boundaries have different atomic structures characterized by, for example, different interatomic spacings. Then those small features, like crystallite orientations, which characterize certain specific grain boundary structures, will be averaged out statistically. Therefore, nanophase material is the best candidate to study the relationship between grain boundary width and crystal structure. It is also easy to measure the grain boundary effect in nanophase material since many of the atoms are situated in grain boundaries.

If the average widths of grain boundaries are only a few angstroms, a high degree of disorder at the grain boundaries is probably impossible. If, on the other hand, the widths of the grain boundaries are 1 nm or more, it is possible for local atomic arrangements at grain boundaries to be highly disordered. In many Fe-based transition metal alloys, the low energy difference between the fcc and hcp structures suggests that microstructural gaps between crystallites in fcc alloys should be packed with atoms as densely as possible. The bcc structure, on the other hand, is more open than the fcc structure, and the bcc structure is influenced by the directional bonding characteristics of d-electrons (41-42). It is reasonable that the microstructural gaps between crystallites in bcc alloys are not packed as densely as possible, but some angular accommodation of atoms in the grain boundaries may be necessary. Unlike the case for fcc alloys, atoms cannot be simply attached to a bcc crystallite until the crystallites impinge. This difference could lead to a greater width of bcc grain boundaries, or strong relaxations at the edges of bcc crystallites. It is our goal to study the relation between grain boundary width and crystallite structure.

Microstructural information obtained by Mössbauer spectrometry is frequently magnetic in origin; phases and local atomic environments are distinguished most clearly when they cause different magnetic polarizations of electrons at ^{57}Fe atoms because these polarized electrons cause strong perturbations of ^{57}Fe nuclear energy levels. There were some reports that the atomic structure of the nanophase materials was found by Mössbauer spectroscopy to be different from the structure of the polycrystal (13) or a metallic glass material (43), and the volume fraction of interfacial component is linearly proportional to the spectral fraction obtained from Mössbauer spectroscopy (43). Therefore, Mössbauer spectroscopy is very useful to study the relation between crystal structure and grain boundary width.

References for Chapter 1

1. R. Birringer, H. Gleiter, H. P. Klein, and P. Marquardt, Phys. Lett., A **102**, 365 (1984).

2. X. Zhu, R. Birringer, U. Herr, and H. Gleiter, Phys. Rev. B, **35**, 9085 (1987).

3. T. Haubold, R. Birringer, B. Lengeler, and H. Gleiter, Phys. Lett. A, **135**, 461 (1989).

4. R. Birringer, Mater. Sci. Engr. A, **117**, 33 (1989).

5. H. Gleiter, Prog. Mater. Sci., **33**, 223-315 (1989).

6. M. R. Fitzsimmons, J. A. Eastman, M. Mullerstach, and G. Wallner, Phys. Rev. B, **44**, 2452 (1991).

7. G. J. Thomas, R. W. Siegel, and J. A. Eastman, Scripta Metall. Mater., **24**, 201 (1990).

8. R. W. Siegel and G. J. Thomas, Ultramicroscopy, **40**, 376 (1992).

9. W. Wagner, R. S. Averback, H. Hahn, W. Petry, and A. Wiedenmann, J. Mater. Res., **6**, 2193 (1991).

10. E. Jorra, H. Franz, J. Peisl, G. Wallner, W. Petry, R. Birringer, H. Gleiter and T. Haubold, Philos. Mag. B, **60**, 159 (1989).

11. H. J. Fecht, E. Hellstern, Z. Fu, and W. L. Johnson, Metall. Trans. A, **21A**, 2333 (1990).

12. H. Kuwano, H. Ouyang and B. Fultz, Materials Science Forum, **88-90**, 561 (1992).

13. U. Herr, J. Jing, R. Birringer, U. Gonser, and H. Gleiter, Appl. Phys. Lett., **50**, 472 (1987).

14. U. Herr, J. Jing, U. Gonser and H. Gleiter, Solid State Commun., **76**, 197 (1990).

15. C. A. Melendres, A. Narayanasamy, V. A. Maroni, and R. W. Siegel, J. Mater. Res., **4**, 1246 (1989).

16. R. W. Siegel, MRS Bulletin, **15**, 60 and cover (1990).

17. C. Suryanarayana and F. H. Froes, Metall. Trans. A, **23A**, 1071 (1992).

18. W. Wunderlich, Y. Ishida, and R. Maurer, Scripta Metall. Mater., **24**, 1675 (1990).

19. S. K. Ganapathi and D. A. Rigney, Scripta Metall. Mater. **24**, 1675 (1990).

20. H. Gleiter, Phase Transitions, **24-26**, 15 (1990).

21. R. S. Averbach, H. Hahn, H. J. Höfler, and J. C. Logas, Appl. Phys. Lett., **57**, 1745 (1990).

22. M. J. Mayo, R. W. Siegel, A. Narayanasamy, and W. D. Nix, J. Mater. Res., **5**, 1073 (1990).

23. C. L. Chien, Gang Xiao and S. H. Liou, Journal de Physique, **C8**, 1821 (1988).

24. G. Herzer, IEEE Trans. Magn., **25**, 3327 (1989).

25. H. E. Schaefer, R. Würschum, R. Birringer and H. Gleiter, Journal of the Less-Common Metals, **140**, 161 (1988).

26. J. S. Benjamin, Sci. Amer., **234**, 40 (1976).

27. J. S. Benjamin and T. E. Volin, Metall. Trans., **5**, 1929 (1974).

28. D. R. Maurice and T. H. Courtney, Metall. Trans. A, **21A**, 289 (1990).

29. C. C. Koch, O. B. Cavin, C. G. McKamey and J. O. Scarbrough, Appl. Phys. Lett., **43**, 1017 (1983).

30. C. Politis and W. L. Johnson, J. Appl. Phys., **60**, 1147 (1986).

31. E. Hellstern and L. Shultz, Philos. Mag. B, **56**, 443 (1987).

32. R. B. Schwartz, R. R. Petrich and C. K. Saw, J. Non-Cryst. Sol., **76**, 281 (1985).

33. E. Hellstern, H. J. Fecht, Z. Fu and W. L. Johnson, J. Mater. Res., **4**, 1292 (1989).

34. H. J. Fecht, E. Hellstern, Z. Fu and W. L. Johnson, Adv. Powder Metall., **1-2**, 111 (1989).

35. B. Fultz, G. Le Caër and P. Matteazzi, J. Mater. Res., **4**, 1450 (1989).

36. H. Kuwano, H. Ouyang and B. Fultz, Nanostructured Materials, **1**, 143 (1992).

37. P. S. Gilman and J. S. Benjamin, Annu. Rev. Mater. Sci., **13**, 279 (1983).

38. G. Herrmann, H. Gleiter and G. Bäro, Acta Metall., **24**, 353 (1976).

39. H. Gleiter, Mater. Sci. Eng., **52**, 91 (1982).

40. Editors R. W. Cahn, P. Haasen, Physical Metallurgy (Elsevier Science Publishers B. V., 1983), chapter 10 B.

41. E. S. Machlin and J. Shao, J. Phys. Chem. Solids, **44**, 435 (1983).

42. J. M. Willis, Olle Eriksson, Per Söderlind, and A. M. Boring, Phys. Rev. Lett., **68**, 2802 (1992).

43. J. Jing, A. Krämer, R. Birringer, H. Gleiter and U. Gonser, J. Non-Cryst. Solids, **113**, 167 (1989).

Chapter 2 General Theory of Mössbauer Effect

This chapter discusses the fundamental features of the Mössbauer effect used in our work. It is based on the references (1-4). The origin of the Mössbauer effect is described in § 2.1. The hyperfine magnetic effects are described in § 2.2. The recoil-free fraction is discussed in § 2.3. The transmission intensity is described in § 2.4. The isomer shift is described in § 2.5. The second-order Doppler shift is described in § 2.6. Superparamagnetism is discussed in § 2.7.

2.1 Introduction

Mössbauer spectroscopy is a technique to study the absorption of gamma–rays by the nuclei of atoms. Recoilless nuclear resonance was discovered and interpreted in 1958 by Rudolf L. Mössbauer, using the 129 KeV gamma–ray of ^{198}Ir (5). The vast majority of research with this technique has been in the fields of solid state physics, chemistry, metallurgy, and biophysics.

Under normal situations, it is not easy to observe the phenomena of resonance fluorescence from nuclear gamma-rays since some recoil energy is lost by the photon during the processes of emission and absorption. This recoil energy loss is usually large enough to displace the emission and absorption lines, which, therefore, break down the resonance conditions. However, the recoil momentum does not always induce a change in phonon spectrum of the whole lattice. The basis of Mössbauer effect is the emission of gamma-ray by radioactive nuclei, and the subsequent reabsorption of these gamma-ray by other nuclei of the same kind of atoms, with negligible recoil energy transferred to internal excitations of the lattice (Fig. 2.1). The emission and absorption spectra are composed of strong lines with natural width superimposed on a broader distribution caused by the thermal motion of the atoms in solids (6-7). The nuclear emission and absorption energies are slightly changed by the solid where the nuclei are incorporated. These tiny changes of energy can be measured and used to learn about the surroundings of the nuclei. The nuclear energy levels changes seen by Mössbauer spectrometry are due to the first few nearest-neighbor shells of a ^{57}Fe nucleus (8-10).

Though more than thirty elements are known to exhibit the Mössbauer effect today, most experiments have been carried out on materials which contain ^{57}Fe and ^{119}Sn, as the measurement can be made easily at room temperature and these elements are interesting to chemists and metallurgists. Especially for ^{57}Fe, the effect persists up to temperatures of over 1000 °C and its natural line width is very narrow (3), which makes Mössbauer spectroscopy a very useful technique. The following description is given for the iron and iron alloy experiment, since ^{57}Fe was being employed in this work. Spontaneous decay of the ^{57}Co nucleus involves the emission of 14.39 KeV gamma-ray in the final decay from the first excited state (nuclear spin I=3/2 with the set of I_Z : -3/2, -1/2, 1/2, 3/2) of ^{57}Fe to the ground state (I=1/2 with the set of I_Z : -1/2, 1/2). In the nuclear transition I_Z may only change by -1, 0, or +1 from the magnetic dipole selection rule. Therefore, there are no more than six different transition energies. The emitted gamma–ray has a Lorentzian energy spread with line width of 4.7×10^{-9} eV. In the Mössbauer effect, this gamma–ray is resonantly absorbed without recoil

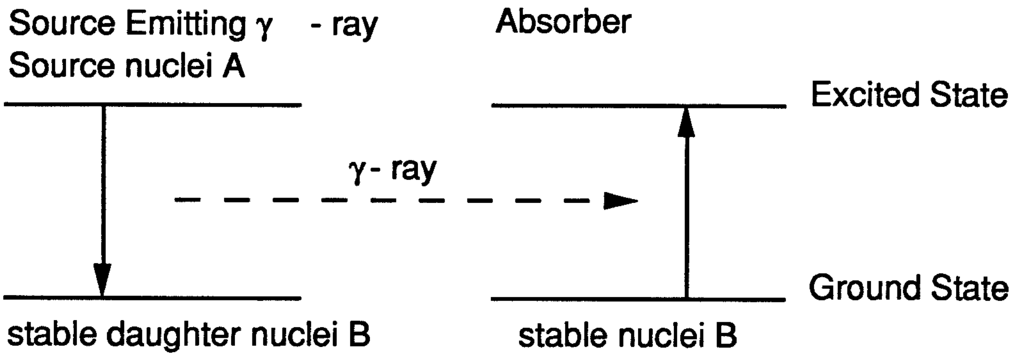

Figure 2.1. Schematic plot of the events in Mössbauer spectroscopy. The horizontal lines represent the nuclear states. The left part shows the source nucleus going to the ground state by emitting a gamma ray. The gamma ray is then absorbed (right), lifting the absorber nucleus up to its excited state. The resonance absorption can be detected either by the decreased transmission of the absorber, or by the subsequent decay of the nuclei of absorber from the excited state.

by another ^{57}Fe. There are two different arrangements of Mössbauer spectroscopy (Fig. 2.2, 2.3). The experiment in our work was done in transmission geometry. The ^{57}Co, the source of gamma-rays, is placed in a Rh matrix, which does not have crystal fields to lift the degeneracy of the 3/2 and 1/2 states (11). Then a thin specimen containing ^{57}Fe is placed between the source and a detector. To realize the observation of a spectrum, the gamma-ray energy is varied by use of the Doppler effect, i.e., by moving the radioactive source back and forth. If velocity is taken as positive when the motion of the source is toward the sample, the gamma-ray energy can be expressed by:

$$E(v) = E_0 (1 + v/c) ,$$

where

$E_0 = 14.39$ KeV

v = velocity of source in mm/sec

c = velocity of light (3×10^{11} mm/sec).

The Mössbauer spectrum is usually reported as transmission intensity versus velocity as shown in Fig. 2.2. As the Doppler energy shifts cause the energies of gamma-rays match the excitation energies of nuclei in the absorber, the nuclear resonance causes higher absorption, and a dip in the measured transmission. The Mössbauer spectrum consists of these dips. Usually the transmission spectrum is more efficient than backscatter experiment. However, there are two major advantages of scattering experiments. (A) For transmission geometry the thickness of sample must be thin enough to let

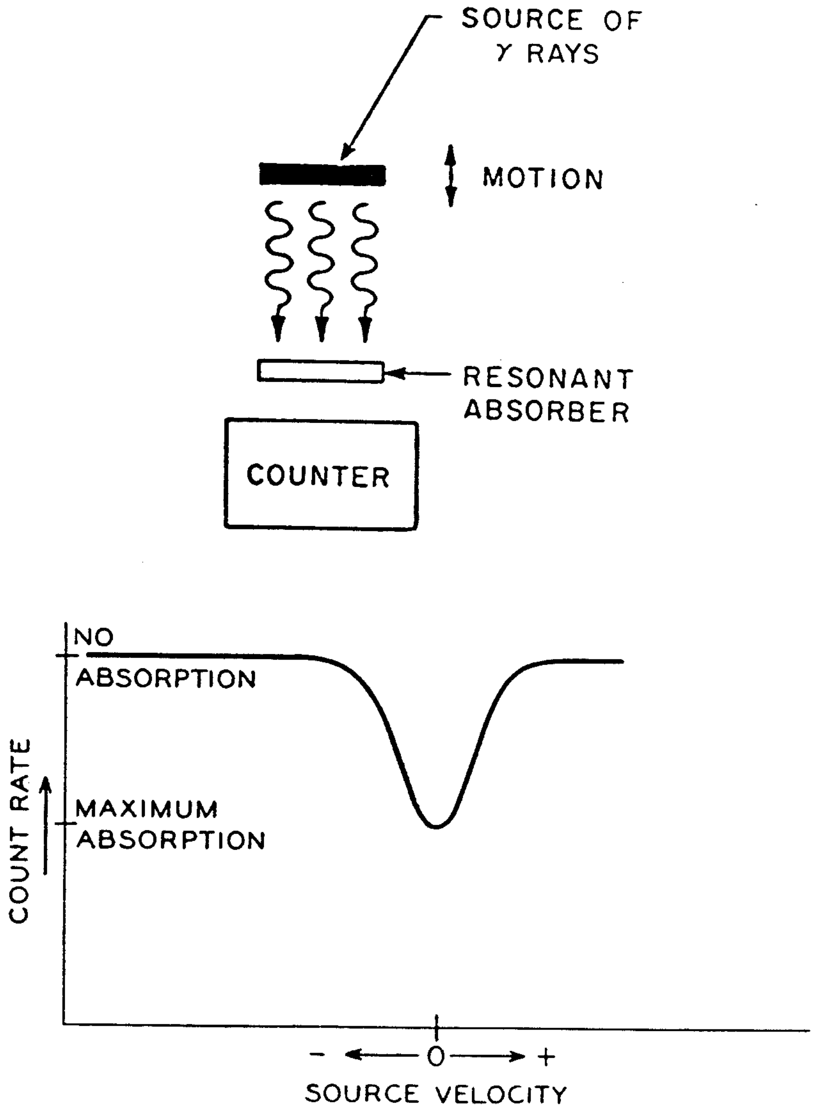

Figure 2.2. Basic arrangement for obtaining a Mössbauer spectrum in transmission geometry. The source is moved to vary the gamma ray energy by use of the Doppler effect. The higher absorption happens when the gamma ray energy is absorbed resonantly by the nuclei of sample, which results in decreased counting rate (2).

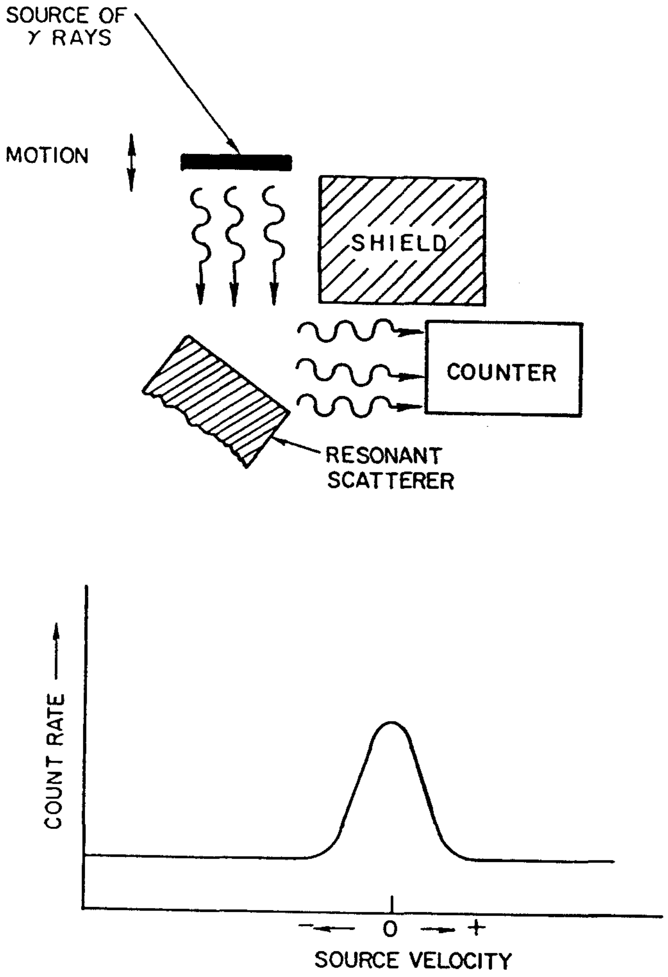

Figure 2.3. Basic arrangement for obtaining a Mössbauer spectrum in scattering geometry. The source is moved to vary the gamma ray energy by use of the Doppler effect. The higher absorption happens when the gamma ray energy is absorbed resonantly by the nuclei of sample, which raises the nuclei of absorber to excited states. Those excited nuclei decay by emitting radiation, which results in higher counting rate (2).

gamma-rays go through. Thin specimens are not necessary for backscatter experiments. (B) It is possible to study only the surface layer of a sample in a scattering experiment.

2.2 Hyperfine Magnetic Field Effects

If a atom is situated in a static uniform magnetic field **H**, this field interacts with all the magnetic moments **M** present in the atom. The eigenvalue of the Zeeman Hamiltonian , H_Z, is the interaction energy of the atom with the field H. The Hamiltonian can be expressed as

$$H_Z = -\mathbf{H} \cdot \mathbf{M} .$$

The Zeeman Hamiltonian can cause the splitting of the energy levels of a ^{57}Fe nucleus.

The magnetic hyperfine interaction (nuclear Zeeman effect) is due to the interaction of the nuclear magnetic moment with the effective magnetic fields at the nucleus. In the ^{57}Fe nuclei, for example, this interaction splits the degeneracy of the nuclear states into more levels according to different components of the nuclear spin. For the excited state with the nuclear spin $I=3/2$, I_Z can be : $-3/2, -1/2, 1/2, 3/2$, and I_Z can be : $-1/2, 1/2$ for the ground state. The interval between levels is proportional to the effective magnetic field. With a selection rule for magnetic dipole radiation that forbids the $I=-3/2$ to $I=+1/2$ and $I=+3/2$ to $I=-1/2$ transitions, there are six allowed transitions between the excited state and ground state of the ^{57}Fe nucleus. The ^{57}Fe

Mössbauer spectrum of a ferromagnetic Fe alloy therefore comprises a sexet of peaks, whose separation is proportional to the hyperfine magnetic field.

2.3 Recoil-Free Fraction

The "recoil-free fraction" f is similar to the Debye Waller factor commonly measured in x-ray diffraction, and represents the fraction of recoil-free emissions (source) or absorptions (absorber) in the resonance phenomena. The recoil-free fraction is related to the binding of nuclei in the lattice and can be employed to study lattice vibrations. The general expression of the recoil-free fraction f of gamma rays for the Mössbauer effect from quantum mechanics is (3-4):

$$f = |\langle i | e^{i\mathbf{k}\cdot\mathbf{X}} | i \rangle|^2,$$

where

$\langle i |$ = initial state of lattice

$\mathbf{k}$ = wavevector of gamma ray

$\mathbf{X}$ = coordinate of center mass of whole lattice.

This formula represents the probability of the gamma-ray emitted without energy loss to the lattice. When the nucleus of an atom incorporated in a solid decays by the gamma emission, the momentum is picked up by the whole solid. This momentum cannot be taken by the translation motion of the nucleus since the energy for a nucleus to leave a lattice site is much larger than the energy available. The lattice vibrations or phonons cannot pick up the momentum since the phonons are standing waves. A phonon does not carry the physical momentum and the expectation value of the momentum for the lattice vibrations vanishes (12). Therefore, the momentum must contribute to the translational motion of the whole lattice, which causes negligible effect on the state of lattice. In the explicit form of the Einstein model it is given by (2):

$$f = \exp\left(-\frac{4\pi^2\langle x^2 \rangle}{\lambda^2}\right),$$

where

$\langle x^2 \rangle$ = mean of the square amplitude of the displacement of the emitting atom from its equilibrium position under thermal vibration in the propagation direction of the gamma-ray averaged over an interval equal to the lifetime of the nuclear level involved in the gamma-ray emission (or absorption) process

λ = the wavelength of the gamma-ray.

The condition for strong absorption is that the vibrational amplitude of the emitting atom is small compared to the wavelength of gamma-ray. Therefore, small vibrations of atoms are essential for a strong Mössbauer effect in the Einstein model.

When a Debye model is used instead of an Einstein model it is necessary to consider the large number of oscillator levels and their frequency distribution. Each of the available levels has a certain probability to be excited by the recoil. Quantitatively the Debye model gives the following expression for the recoil-free fraction (13):

$$f = \exp\left\{ -\frac{6E_r}{k_B\theta_D} \left[\frac{1}{4} + \left(\frac{T}{\theta_D}\right)^2 \int_0^{\frac{\theta_D}{T}} \exp\left(-\frac{x}{e^x - 1}\right) dx \right] \right\},$$

where

E_r = recoil energy of the free atom

k_B = Boltzmann's constant

T = temperature

θ_D = Debye temperature.

This equation is useful to estimate the intensity change of the Mössbauer effect versus temperature, and also can be used to calculate the Debye temperature. Qualitatively the recoil-free fraction decreases as temperature rises.

2.4 Transmission Intensity

Since both the incoming gamma-ray and the absorption level of the sample have Lorentzian energy distributions (14), the observed absorption is a convolution of these two distributions (15). Neglecting the self-absorption of gamma-rays by the source, the transmitted intensity of the Mössbauer spectrum for a sample with uniform thickness t is given as a function of Doppler velocity v by (16):

$$P(v) = (1\text{-}f_S) + f_S \int_{-\infty}^{\infty} S(E\text{-}V_S\text{-}v)\exp\left(-\frac{T\tau^2/4}{(E\text{-}V_A)^2+\tau^2/4}\right) dE$$

$$= (1\text{-}f_S) + f_S \int_{-\infty}^{\infty} S(E\text{-}v)\exp\left(-\frac{T\tau^2/4}{(E\text{-}V_O)^2+\tau^2/4}\right) dE, \qquad (\text{Eq. } 2\text{-}1)$$

where

$V_O = V_A\text{-}V_S$

V_S = centroid of the emitted gamma-ray energy spread when v equal to zero

V_A = centroid of the absorption level spread

f_S = source recoil-free fraction

$S(E) = \frac{2}{\pi\tau}\frac{T\tau^2/4}{E^2+\tau^2/4}$ = energy distribution function of the γ-ray

τ = half width of the energy distribution = 4.67 × 10-9 eV = 0.097mm/sec

$T = f_A\, n_A\, a_A\, \sigma_O\, t$

f_A = absorber recoil-free fraction

n_A = number of iron nuclei per cm^3 in the absorber

a_A = fractional abundance of ^{57}Fe isotope in the absorber

σ_O = total absorption cross section.

If there are several absorption levels, as is often the case, (Eq. 2-1) becomes:

$$P(v) = (1-f_S) + f_S \int_{-\infty}^{\infty} S(E-v) \exp\left(- \sum_i \frac{Tq_i \tau^2/4}{(E-V_i)^2+\tau^2/4} \right) dE, \qquad \text{(Eq. 2-2)}$$

where

q_i = normalized probability of the ith transition. ($\sum_i q_i = 1$)

V_i = difference between the centroid of the ith absorption level and that of the emitted g-ray when v equal to zero.

For a very thin absorber, (T « 1), the exponential term can be expanded and the equation simplified. Retaining only the leading terms, (Eq. 2-2) can be simplified as (16):

$$P(v) \approx 1 - f_S \sum_i \frac{Tq_i}{2} \frac{\tau^2}{(v-V_i)^2+\tau^2}$$

$$= 1 - f_S \sum_i \frac{Tq_i}{2} L(v; V_i, 2\tau, h_i) \qquad \text{(Eq. 2-3)}$$

$$(h_i = \frac{Tq_i}{2}),$$

where the Lorentzian function is defined by:

$$L(v; V_i, 2\tau, h_i) = \frac{h_i \tau^2}{(v-V_i)^2+\tau^2}.$$

Therefore, the absorption area is proportional to recoil free fraction and the peak shape behaves as the sum of Lorentzian functions.

2.5 Isomer Shift

The origin of the isomer shift is from the interaction energy of the electronic cloud inside the range of the nucleus with the nuclear charge over a finite nuclear radius in the excited and ground states; i.e., the effect of the finite nuclear size on the Coulomb energy. The electrostatic interaction energy of the isomer shift is about 10^{-4} eV (2-3) with respect to a point nucleus. A change in nuclear radius can occur even without a change in nucleon number, for example, the radius of excited state nucleus r_{ex}, is generally slightly different from that of ground state nucleus r_g. For ^{57}Fe, the nuclear radius of the excited state is less than that of the ground state. However, it is the opposite for ^{119}Sn (1). In actual experiments it is the difference in transition energies between a source and an absorber which is measured.

In order to understand the isomer shift, a simplified problem of a spherical nucleus of finite radius surrounded by its orbital electrons is considered. It is assumed that the relevant electron wave function $\psi(r)$ (usually from s-electrons) is essentially constant over the range of nuclear charge and is equal to $\psi(0)$ (wave function at nuclear center) , otherwise the kinetic energy of electron would be extremely large over such a small distance (first derivative of wave function with respect to distance can be related to momentum). The electrostatic interaction between the electron and the nucleus which is in excited state is:

$$E_{ex} = -e \int_0^\infty V(r_e) \mid \psi(0) \mid^2 \, d r_e \ ,$$

where

e = electronic charge

r_e = position vector of electron (choose the nuclear center as origin)

$V(r_e)$ = electrostatic potential created by the nucleus at distance r_e and can be expressed as:

$$V(r_e) = -e \int_0^\infty \frac{\rho_{ex}(r_{ex})}{\mid r_e - r_{ex} \mid} \, d r_{ex} ,$$

where

ρ_{ex} = electronic density of excited state

r_{ex} = position vector of excited nucleus.

From a surface charge model, the potential will behave like $-\frac{Ze}{r_e}$ if r_e is larger than the nuclear radius ($r_e >> r_o$) but it will remain constant $-\frac{Ze}{r_{min}}$ as r_e is less than some value r_{min} (3, 17). (There is a different assumption which makes the first derivative of potential become continuous at $r_e = r_{min}$ (18), but the result is similar.) By introducing the second moment of nuclear charge distribution to avoid the explicit integration over nuclear coordinates, the difference of electrostatic interaction energy of the excited state for the finite nucleus with a given nuclear radius will be (3, 17):

$$E_{ex} = \frac{2}{3} \pi Z e^2 < r_{ex}^2 > \mid \psi(0) \mid^2 ,$$

where

$$< r_{ex}^2 > = \frac{1}{Z} \int_0^\infty \rho_{ex}(r_{ex})\, r_{ex}^2\, d\, r_{ex} .$$

Therefore, the change of electrostatic interaction energy for the nuclear transition is:

$$E_{ex} - E_g = \frac{2}{3} \pi Z e^2 \; | \psi(0) |^2 (< r_{ex}^2 > - < r_g^2 >) .$$

$| \psi(0) |^2$ will be different for different materials. The isomer shift can be observed only if the two nuclear states involved have different radii. If the chemical environments of source, s, and absorber, a, are different such that the wave functions at the nuclei in the source and absorber are different, the isomer shift δ_{IS} can be written (2-3, 19-20):

$$\delta_{IS} = \frac{2}{3} \pi Z e^2 \; (< r_{ex}^2 > - < r_g^2 >) \{ | \psi(0)_a |^2 - \; | \psi(0)_s |^2 \} .$$

The main result from above is that the isomer shift depends on the differences of $< r^2 >$ and $| \psi(0) |^2$. The differences in $< r^2 >$ are too small to handle by nuclear theorists (17). The other quantity $| \psi(0) |^2$ is dominated by the s-electrons. The 1s-electrons contribute more than 80 % of the total density (4, 17). However, this does not mean that other small contributions can be ignored. The change of p, d, and f-electrons also can cause the indirect s-electron change by shielding outer s-electrons from nucleus (21-22). Although much effort has been spent in this subject, the understanding of $| \psi(0) |^2$ differences is still not enough when the nucleus is under various environments in solids. Therefore, one can conclude that the nature of isomer shift is well understood qualitatively. However, the quantitative calculation is not easy since the accurate wave functions for electrons in solids, especially for metallic systems, are very complicated.

2.6 Second-Order Doppler Shift

For metallic iron, the chemical isomer shift is basically temperature independent until the temperature is higher than Curie temperature (4). Nevertheless, there will be a temperature dependent shift of the centroid of the Mössbauer spectrum. The second-order Doppler shift (SODS) is a small decrease in the energy of the γ-ray emission or absorption resulting from the relativistic effects of the thermal vibrational velocity, v, of the nuclei. This phenomena can be observed in the Mössbauer experiment if the temperatures of source and absorber are different. It can be explained by a straightforward application of relativity. If the source is at very low temperature, v is about zero. The source then can become a role like stationary clock. The absorber at very high temperature has a root-mean-square velocity $<v^2>^{1/2}$, which can play a role of a clock in a rocket. The clock in a rocket is slower than the stationary clock. The energy shift of SODS has the value:

$$\delta E_{sods} = -\frac{\overline{v^2}}{2c^2} E\gamma ,$$

where

$\overline{v^2}$ = the average squared velocity of the oscillating atoms in the lattice

c = the velocity of light

$E\gamma$ = the γ transition energy.

$\overline{v^2}$ is dependent on temperature, pressure, and Debye temperature of the surrounding matrix. The second-order Doppler shift (SODS) is dependent on the vibrations of the atoms in the lattice and can be expressed in terms of energies associated with vibrational modes in a harmonic lattice (23). SODS is superimposed on the isomer shift (3, 17, 24), and it is very difficult to distinguish the isomer shift and the SODS. The Debye temperature can be determined from the second-order Doppler shift, S_{sods} as follows (17, 24):

$$S_{sods} = -\frac{1}{2c}\left(\frac{9k_B\theta_D}{8M} + \frac{9k_BT}{M}\left(\frac{T}{\theta_D}\right)^3 \int_0^{\frac{\theta_D}{T}} \frac{x}{e^x - 1}dx \right),$$

where

c = speed of light

k_B = Boltzmann's constant

θ_D = Debye temperature

M = mass of ^{57}Fe atom.

Since $\overline{v^2}$ is strongly temperature dependent and may change dramatically at phase transitions, the SODS becomes important when the temperature dependence of the isomer shift and its behavior near phase transitions are studied. For ^{57}Fe and ^{119}Sn, most of the temperature dependence of the center shift is usually from SODS.

2.7 Superparamagnetism

Superparamagnetism is the process of collective reorientation of the magnetic moment direction in fine particles. It is encountered in cases like thin iron films (25), and small Fe-oxide particles (26). This phenomena arises in the following way: If a magnetic material is cooled below the magnetic ordering temperature (Morin transition temperature), the spins of magnetic domains will tend to align along one direction, therefore producing magnetic ordering.

The hyperfine fields determining the splitting of the nuclear energy levels are dynamic. Hyperfine parameters may fluctuate so rapidly that the hyperfine structure is determined by a time average of the fluctuating value; this occurs in magnetically ordered materials as the sublattice magnetization is significantly less than the saturation value. Bulk materials of magnetically ordered systems containing high concentrations of 3d-elements normally satisfy this criterion. Therefore, in the measurement of magnetic properties for single domain particles what is observed depends on the ratio of the time required for the measurement, τ_{obs}, to the relaxation time, τ_o. τ_{obs} is the reciprocal of the hyperfine frequency υ_{obs}, which is often called the Larmour frequency. The hyperfine frequency can be related to the hyperfine splitting (or Zeeman splitting) of nuclear energy levels E_{obs} as:

$$\upsilon_{obs} = \frac{E_{obs}}{h} ,$$

where

h = Plank's constant (4.135×10^{-15} eV sec).

τ_o is the time between changes of direction of the hyperfine field, or relaxation time, which can be written as (26):

$$\tau_o = \frac{1}{a\,f}\,\exp\left(\frac{2Kv}{kT}\right),$$

where

a = geometrical factor, the number of different directions the magnetization vector can flip.

f = frequency factor, the Larmour frequency of the magnetization vector in an effective field.

K = anisotropy energy of the material, the energy required to go from one easy direction to another

v = particle volume

k = Boltzmann constant

T = temperature.

Physically it is the thermal fluctuations which cause the magnetization vector to undergo Brownian rotational motion around the easy axis. For $\tau_{obs} \ll \tau_o$, the particles will show ferromagnetic behavior. If the reverse is true, the particles will be superparamagnetic. The ratio, $\frac{2Kv}{kT}$, is the determining factor of the relaxation time, τ_o, since it is the argument of an exponential. For nanophase materials v is a small quantity. In order to increase the ratio, $\frac{2Kv}{kT}$, we have to lower the temperature. Therefore, it is expected to observe the superparamagnetic behavior of nanophase materials at low temperature (or by applying an external magnetic field (27)). Several examples will be discussed in chapter 4.

References for Chapter 2

1. Editor U. Gonser, Mössbauer Spectroscopy (Springer-Verlag, New York, Heidelberg Berlin, 1975), chapter 1 by U. Gonsor and chapter 2 by P. Gütlich.

2. Editor Richard L. Cohen, Applications of Mössbauer Spectroscopy Vol. I (Academic Press, New York, 1976), chapter 1 by Richard L. Cohen and chapter 2 by L. H. Schwartz.

3. Hans Frauenfelder, The Mössbauer Effect (W. A. Benjamin, Inc., New York, 1962).

4. Editor Leopold May, An Introduction to Mössbauer Spectroscopy (Plenum Press, New York-London, 1971), chapter 1 by Peter G. Debrunner and Hans Frauenfelder; chapter 5 by Robert L. Ingalls.

5. R. L. Mössbauer, Z. Physik, **151**, 124 (1958).

6. R. L. Mössbauer, Naturwissenschaften, **45**, 538 (1958).

7. W. E. Lamb, Jr., Phys. Rev., **55**, 190 (1939).

8. G. K. Wertheim, V. Jaccarino, J. H. Wernick, and D. N. E. Buchanan, Phys. Rev. Lett., **12**, 24 (1964).

9. I. Vincze and I. A. Cambell, J. Phys. F: Metal Phys., **3**, 647 (1973).

10. I. Vincze and A. T. Aldred, Phys. Rev. B, **9**, 3845 (1974).

11. S. L. Ruby, L. M. Epstein, and K. H. Sun, Rev. Sci. Instr., **31**, 580 (1960).

12. Charles Kittel, Introduction to Solid State Physics (John Wiley & Sons, Inc., New York, 1986), chapter 4.

13. W. M. Visscher, Ann. Phys., **9**, 194 (1960).

14. J. D. Jackson, Can. J. Phys., **33**, 575 (1955).

15. John M. Cowley, Diffraction Physics (North-Holland Publishing Company, Amsterdam·New York·Oxford, 1981), p. 27.

16. Atsushi Asano, Ph.D. Thesis (1974), Northwestern University at Evanston, Illinois.

17.Editor Shenoy, G. K. and Wagner, F. E., Mössbauer Isomer Shifts (North Holland, 1977), chapter 3 by Shenoy, G. K., Wagner, F. E. and Kalvius, G. M..

18. Shirley, D. A., Rev. Mod. Phys., **36**, 339 (1964).

19. L. R. Walker, G. K. Wertheim, and V. Jaccarino, Phys. Rev. Lett., **6**, 98 (1961).

20. S. Debenedetti, G. Lang, and R. Ingalls, Phys. Rev. Lett., **6**, 60 (1961).

21. Editors D. Goldring and R. Kalish, Hyperfine Interactions in Excited Nuclei (Gordon and Breach, New York, 1971), p. 709-717.

22. Fricke, B. and J. T. Waber, Phys. Rev., B, **5**, 3445 (1972).

23. Housley, R. M. and F. Hess, Phys. Rev., 146, 517 (1966).

24. P. K. Tseng, S. L. Ruby, Phys. Rev., **172**, 249 (1968).

25. M. N. Varma, R. W. Hoffman, J. Appl. Phys., **42**, 1727 (1971).

26. Walter Kündig, Hans Bömmel, Phys. Rev., **142**, 327 (1966).

27. S. Mørup and H. Topsøe, Proc. Internat. Conf. Mössbauer Spectroscopy, Bucharest, Romania (Edited by D. Barb and D. Tarina), p. 229 (1977).

Chapter 3 Experimental

This chapter describes the experimental procedures and instrumentation used in this study. The sample preparation methods are described in § 3.1. Characterization methods and data processing methods are described in § 3.2. X-ray diffraction analyses and transmission electron microscopy image processing are the subjects of § 3.3.

3.1 Sample Preparation

Ball milled nanophase powder samples of elemental metals and alloys with different grain sizes are necessary for this study. Some alloys like Fe-Cr, Fe-Ti, Ni-Fe and Fe-Mn, were prepared from elemental metals of at least 99.9% purity either by induction melting on a water cooled silver hearth in an argon atmosphere or by arc melting on a water cooled copper hearth in an argon atmosphere (1-3). The choice of technique depended on the melting temperature, and the relative reactivity with silver. The ingots, weighing around 8 grams, were turned over and remelted several times to improve homogeneity. During the process, a lump of Ti was used as an oxygen getter and also an indicator of vacuum condition. The mass losses after melting were negligible, so the chemical compositions of the alloys were assumed to be those of the original stoichiometric compounds.

The ball milling was performed in a standard Spex 8000 laboratory mill using hardened steel balls and a vial. An effort was made to exclude oxygen from the vial. After repeated purging of the glove bag with argon, elemental powders and filings from the ingots prepared by melting were sealed in a vial under the argon atmosphere. A 4:1 or 5:1 ball-to-powder weight ratio was used and the vial temperature was kept constant during the milling experiments by forced air cooling. A small effort was spent on low temperature ball milling with the ball milling machine Super-MISUNI Model NEV-MA8 (Nisshin Giken Co., Ltd.). This machine can be operated at different temperatures usually from the range of liquid nitrogen temperature to 300 °C, and with different vibration frequencies. It is unfortunately extremely inefficient to use the machine at liquid nitrogen temperature. Since the liquid nitrogen evaporated very fast during the milling process, the liquid nitrogen reservoir needed to be refilled every 15 minutes.

After different milling times at room temperature, the mechanical attrition was interrupted and a small quantity of powder was removed for analyses by x-ray diffractometry and Mössbauer spectrometry. All the handling was done in the glove bag pre-purged five times under an argon atmosphere in order to suppress oxidation.

The ball-milling vial must be cleaned with care after use, otherwise contamination from the previous materials and water can be very serious. The contamination can usually be discovered from x-ray diffraction measurement and chemical analysis. After each ball-milling run, the vial was emptied of powder,and a cleaning run was started with only steel hardened balls and alcohol. After different milling times the cleaning run was interrupted and all the alcohol was replaced by fresh alcohol. The residual materials adhering to the inside of the vial had the tendency to disperse into the alcohol, which can be explained if the alcohol is a surfactant. The vial was then sand-blasted several times in order to remove all the impurities remaining on the surface of the vial. After repeating the milling process with alcohol, the vial was baked for one hour at 100 °C in order to get rid of the water and alcohol.

In order to induce grain growth, annealings at elevated temperatures (usually 300 °C) were performed. With repeated evacuations and purgings under helium gas atmosphere, the sample powder was sealed in borosilicate glass ampules (or in the quartz ampules if the annealing temperature was higher than 550 °C, at which the borosilicate glass started to soften).

3.2 Characterization of Nanophase Alloys

A. X-ray Diffractometry

The structures and grain sizes of the nanophase alloys were characterized by x-ray diffractometry. A conventional General Electric XRD-5 θ-2θ diffractometer (Cr Kα radiation) and a Philips θ-2θ diffractometer (Cu and Mo Kα radiation) were used to analyze the Fe-Mn, Fe-Cr, Fe-V and Fe-Ti alloys. An INEL CPS 120 x-ray diffractometer (Co Kα radiation) with graphite incident beam monochromator was used to analyze the Ni-Fe, Fe-Mo, Fe-B, Fe-Zr, Fe-Sn, Fe-Nb, Fe-Al and Fe-Al-Cr alloys. This INEL x-ray diffractometer, shown schematically in Figure 3.1, is arranged in such a way that the sample, detector, and x-ray beam are all fixed with respect to each other. The emitted x-ray beam hits the sample surface at an incident angle, ϕ.

Then the diffracted x-ray beams are collected simultaneously over a range of 127° with the large-angle curved detector (4). The major advantage of this instrument is that it takes much less time to perform the x-ray diffraction measurement. For example, diffraction measurements with good statistical quality can typically be achieved within a few minutes. A typical example of x-ray diffraction from nanocrystalline material Fe-Zr is shown in Figure 3.2, which was obtained in 10 minutes.

The broadening of the x-ray diffraction lines increased continuously with ball milling time. X-ray linewidths were determined either by fitting the diffraction peaks to functions that are analytic approximations to the convolution of Gaussian and Lorentzian functions (5), or by obtaining the integral breaths of the peaks. For most of our work, methods of integral breadths (5) were employed to analyze x-ray diffraction data. The method of Warren Averbach (6-8) was also used to analyze several cases. However this method is very tedious and time consuming. Furthermore, it is confined to studies of alloys with simple structures like bcc, since the diffraction peak tails tend to overlap with each other for nanophase alloys. The details will be discussed in § 3.3.

B. Transmission Electron Microscopy

Transmission electron microscopy (TEM) was performed with a Philips EM430 microscope operated at 300 kV and Philips EM301 microscope operated at 100 kV. For chemical microanalysis we used an EDAX 9900 energy dispersive x-ray system with a Si[Li] detector at a take-off angle of about 20°. The computer hardware for the EDAX unit consisted of a PDP-11 computer with a multichannel analyzer. The analysis software was provided by EDAX. Specimens for TEM were prepared by grinding the sample powder in a mortar

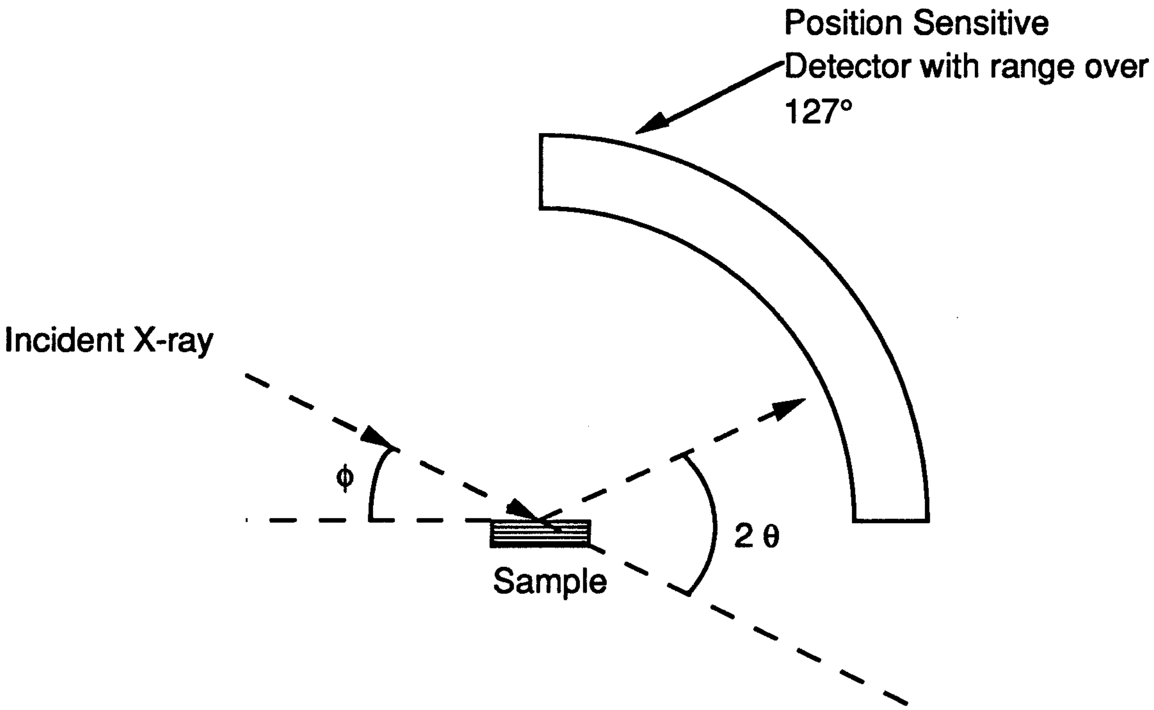

Figure 3.1. Schematic drawing of INEL CPS 120 x-ray diffractometer.

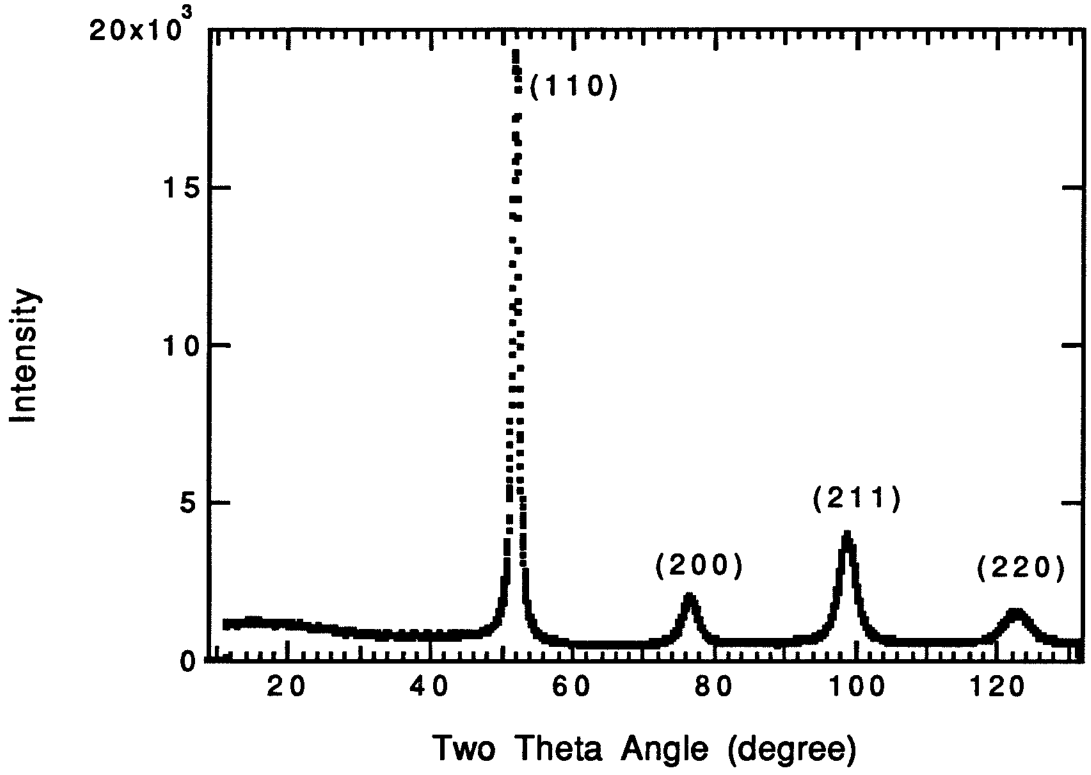

Figure 3.2. X-ray diffractometer recording of the powder pattern of Fe-Zr ball-milled for 30 hrs. The pattern is indexed as bcc structure.

and pestle with propanol, and sprinkling some of the powder on a holey carbon microscope grid. Dark field imagings of some specific diffractions and imaging processings were employed to obtain an estimate of the mean crystallite sizes and the size distribution. This image processing was performed with the software package Image 1.40 running on a Macintosh II computer. The methods and results will be discussed in § 3.3.

C. Electron Microprobe Analysis

Chemical analyses of the powders were performed with a JEOL Superprobe 733 electron microprobe. The resolutions of this instrument are about 1 atomic % in composition, and one micron in spatial position. Specimens for chemical analysis were prepared by first compacting the sample powder into a circular rod in a steel vial, then the sample was polished after being fixed in epoxy at room temperature.

D. Mössbauer Spectrometry

Mössbauer spectrometry has proved to be useful in studies of mechanical alloying, for example see references (9-13). Mössbauer spectra were obtained with a conventional constant acceleration spectrometer having a room temperature source of 50 mCi ^{57}Co in Rh. The schematic graph of the transmission Mössbauer spectroscopy is shown in Figure 3.3. Most spectra were measured with a Mössbauer spectrometer MS-900 (Ranger Scientific, Inc.). The MS-900 Mössbauer spectrometer is a computer based system, designed to be used with the Apple II computer. It includes a proportional counter with preamp, the velocity transducer and multichannel analyzer. The gamma-ray energy spectrum from the detector can be displayed on the monitor in multi-channel analyzer mode. By adjusting the lower and higher level discriminator potentiometers, only the 14.4 KeV Mössbauer gamma-ray

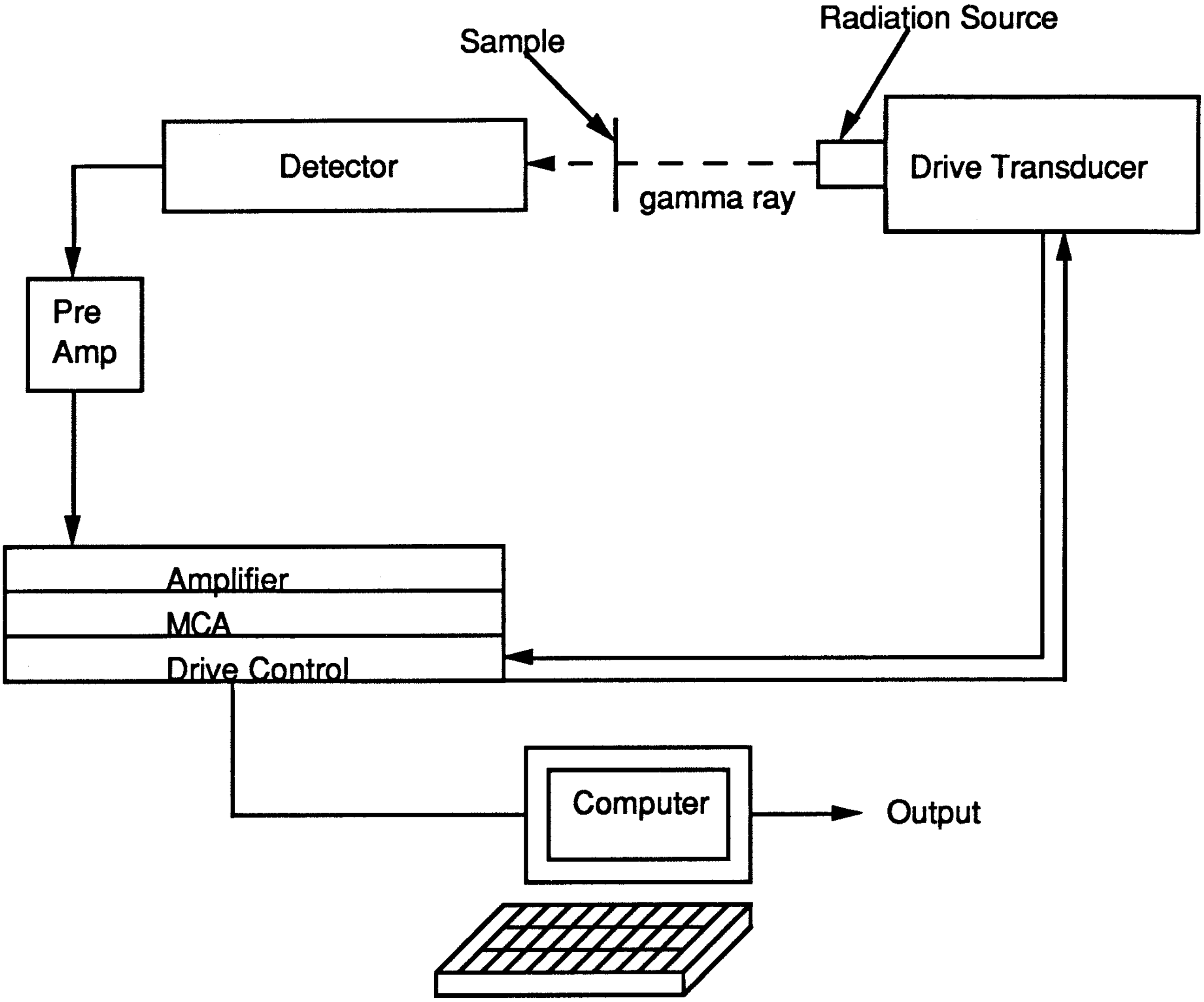

Figure 3.3. The schematic diagram of the transmission Mössbauer spectroscopy.

can be selected.

Usually the data was transferred to a Decstation 3100 minicomputer for analysis. A typical example of a transmission Mössbauer spectrum from a thin iron foil is shown in Figure 3.4. Hyperfine magnetic field distributions were obtained from the experimental spectra by the method of Le Caër and Dubois (14). However, different input, like source peak width and sextet ratio (14), can change hyperfine magnetic field distributions (Figure 3.5). Therefore, it is important to compare the fitting results with the raw spectra.

Mössbauer area measurement is the experiment (15-17) which measures the resonant absorption of the complete sample by means of evaluation of the area under the absorption lines over a range of temperature, usually from liquid helium temperature to room temperature. Dewars for a temperature range from 1.2 to 300 K are discussed in detail in reference (18). Liquid nitrogen was employed as a coolant in the range of 80 - 300 K. Liquid helium was used as a coolant when temperature was below 80 K. The geometrical arrangement of low temperature Mössbauer spectroscopy is about the same as that at room temperature except that the sample was placed in the cryostat, Model 8CC LHe Mössbauer Cryostat (Cryo Industries of America, Inc.). The liquid helium was consumed very fast (30 liters for 8 hours) due to its small heat capacity. Epoxy-coated Mylar was used as the windows. The temperature was varied by using the helium exchange gas and a heating coil in the sample chamber. The schematic plot of cryostat is presented in Figure 3.6.

Microstructural information obtained by Mössbauer spectrometry is frequently magnetic in origin; phases and local atomic environments are distinguished most clearly when they cause different magnetic polarizations

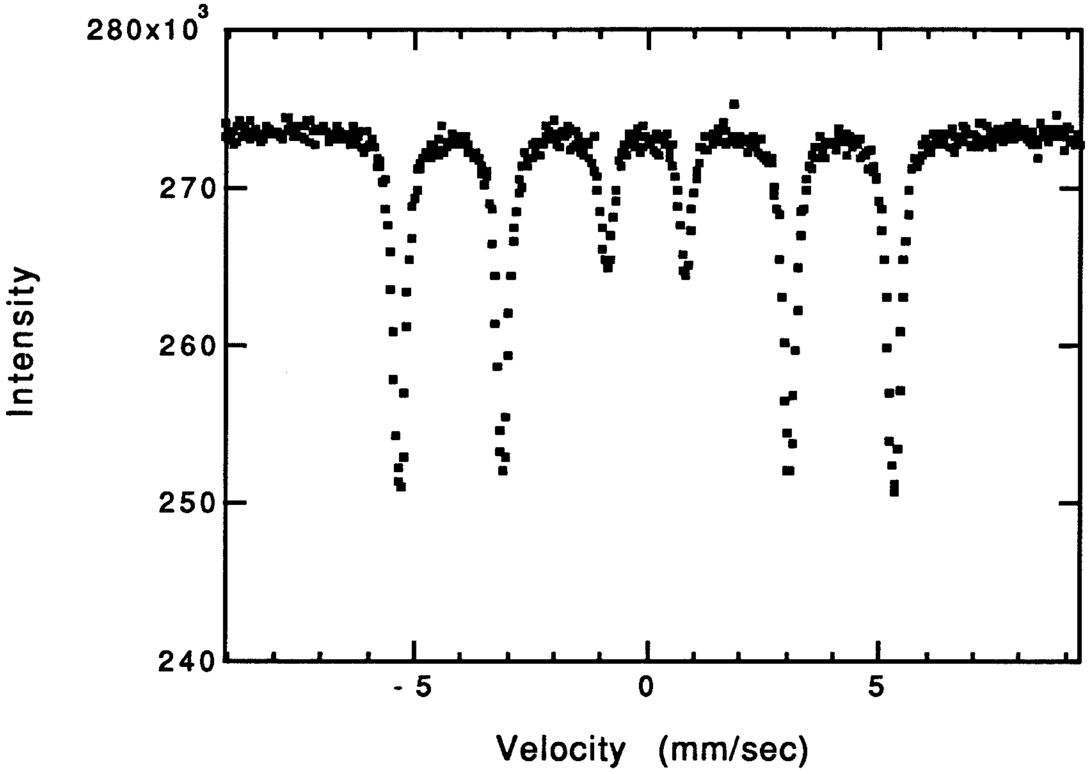

Figure 3.4. Transmission Mössbauer spectrum of thin iron foil. The six lines arise from the nuclear Zeeman splitting effect or hyperfine magnetic interaction.

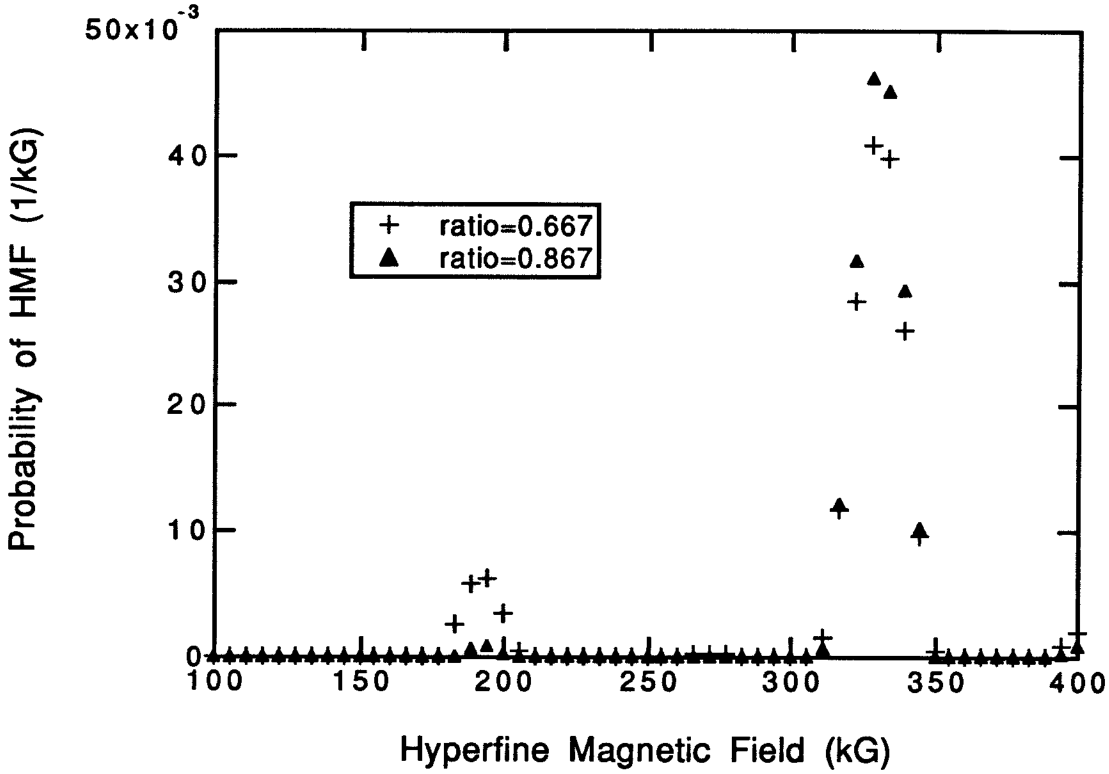

Figure 3.5. The hyperfine magnetic field distributions of Figure 3.4 obtained by the method of Le Caër and Dubois. The superfluous peak around 200 kG can appear by varying the input of peak ratio (14).

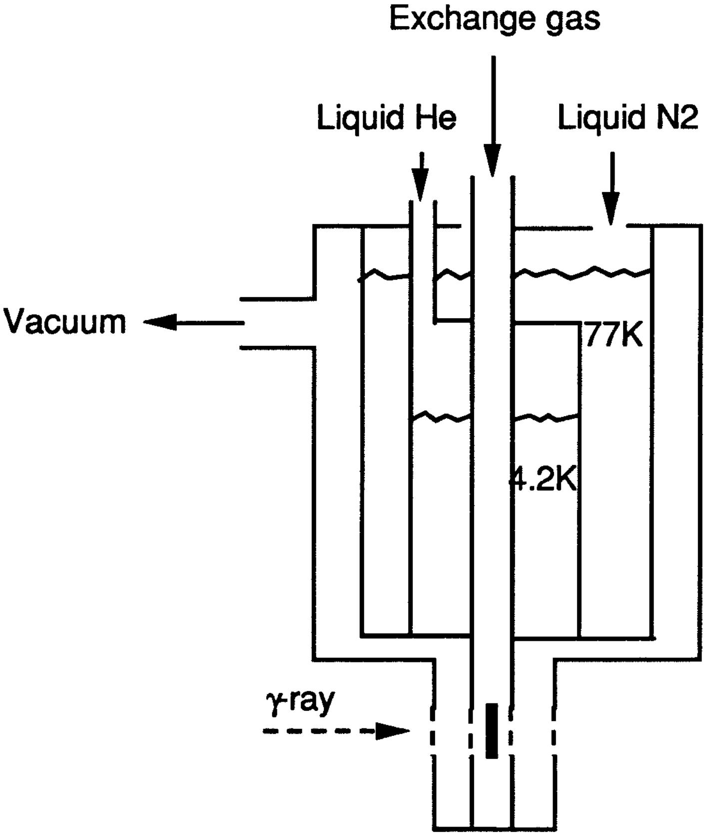

Figure 3.6. Schematic plot of the cryostat used for low temperature Mössbauer spectroscopy.

of electrons at ^{57}Fe atoms because these polarized electrons cause strong perturbations of ^{57}Fe nuclear energy levels (19). The effective magnetic field at the ^{57}Fe nucleus that originates from these polarized electrons is termed the hyperfine magnetic field (HMF). We expected the HMF to vary with the structural environments in nanophase materials, especially for ^{57}Fe atoms near grain boundaries (20-21). A "magnetic signature" of ^{57}Fe atoms at grain boundaries was found for nanophase Fe prepared by gas condensation (16). In this work we report the magnetic signature of ^{57}Fe atoms at grain boundaries in Cr-Fe, Fe-Ti, Ni-Fe, and Fe-Mn. We will report how the number of such grain boundary atoms varied with crystallite size as measured by x-ray diffractometry in chapter 4.

E. Vibrating Sample Magnetometer

This is a technique (22) which measures the magnetic moment of a sample when the sample is vibrated perpendicular to a uniform magnetizing field. The oscillating magnetic field of the vibrating sample induces a voltage in the stationary coils. From this voltage, the magnetic moment of the sample can be obtained by comparing another voltage of a reference sample.

3.3 Grain Size Measurement by X-ray Diffractometry and TEM

X-ray diffractometry and TEM were both used to measure the grain size. The x-ray diffraction peak width increased continuously with ball-milling time. When the lineshapes were fit to convolutions of Lorentzian and Gaussian functions (23), it was found that the Gaussian parts depended more strongly on wavevector k (the order of the diffraction), consistent with effects of a strain distribution (5, 24). The tails of the Gaussian peak go to zero very quickly. It is reasonable to assume that the strain distribution is described by a Gaussian function since we do not expect to see any strain larger than the yield strain. In general, with increasing milling time the diffraction lines became more Lorentzian than Gaussian, and the linewidths became less dependent on wavevector, k. This behavior was interpreted as an early line broadening caused by the growth of the root-mean-squared strain, $\langle \varepsilon^2 \rangle^{1/2}$ (typically 0.005 - 0.01), but further line broadening was caused by a reduction in size of diffracting domains, which we interpret as a decreased crystallite size. The mean crystallite size was obtained as the inverse of the y-intercept of the plot of Δk (from the half-width-at-half-maximum of the linewidth of the Lorentzian part of the fit) versus k (from the order of diffraction) extrapolated to k equal to zero (5). For example, the strain in Cr-Fe milled for 10 hrs was 0.01 by analysis of the slope of the plot of Δk versus k. The grain size was 23 nm from the inverse intercept of the plot. The reduced crystallite size dominated the x-ray line broadening after a few hours of ball milling. After long milling times, the x-ray diffraction lineshapes were reasonably close to Lorentzian functions. From this it is deduced that the distribution of crystallite lengths was approximately exponential (25) since the Fourier transform of a exponential function is the Lorentzian function, which agrees with the results from analyses of TEM images such as presented in Figure 3.7. The results basically are consistent with other works (26). However, it must be emphasized that different methods of sample preparation can cause different grain size distributions. For example, the grain size distributions produced by gas condensation are usually log-normal (27). The mean particle sizes determined by XRD and TEM were in reasonable

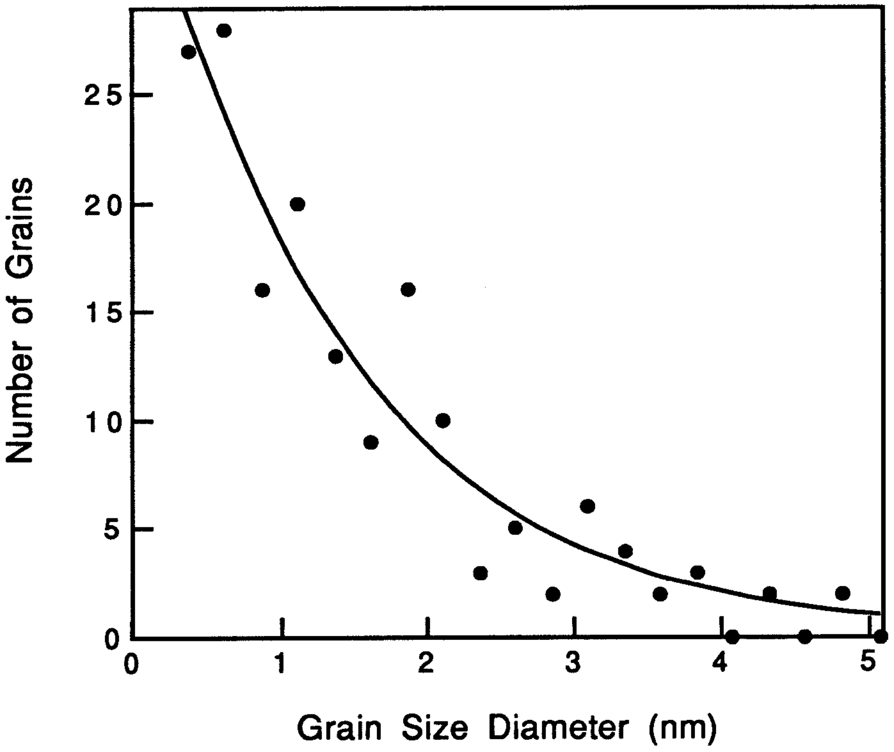

Figure 3.7. Grain size distribution obtained from processing of TEM (110) dark field image from Cr-18.5 % Fe powder after ball milling for 96 hours.

agreement, considering that the dark field images show the maximum projection of the particle profile. Besides the method above for analyzing x-ray diffraction data, the method of Warren Averbach (6-8) was also used to analyze several alloy systems. The major advantage of this method is that it is not necessary to perform curve-fittings of the diffraction peaks by assuming some special functions associated with strain and grain size distributions. The column length information and the strain information are provided as the functions of the different coefficients of the Fourier transform of the diffraction peaks of the first two orders of parallel crystallographic planes. However, the results of this method are very sensitive to the range of the diffraction peak, which is taken for Fourier transform. Complicated systems of diffraction patterns are not convenient for study by the method of Warren Averbach since it is not easy to resolve each diffraction peak individually. The tails from other peaks could be easily superimposed on the peak which is Fourier transformed. The results of grain sizes obtained by this method are reasonably consistent with those by the method mentioned above. For example, the grain size of Fe-V milled for 48 hrs was 8.8 nm compared to 7.9 nm obtained from the method of integral breadths. The details of the method of Warren Averbach are described in Appendix A.

Figure 3.8 presents data on crystallites of Cr-18.5 % Fe filings that were ball-milled for times up to 96 hrs. The effective crystallite size is reduced to approximately 3 nm. A typical TEM micrograph is presented in Figure 3.9. This dark field image shows many small diffracting regions whose sizes are consistent with the 3 nm crystallite size determined by x-ray diffractometry. The crystallite size distribution also includes a few large grains.

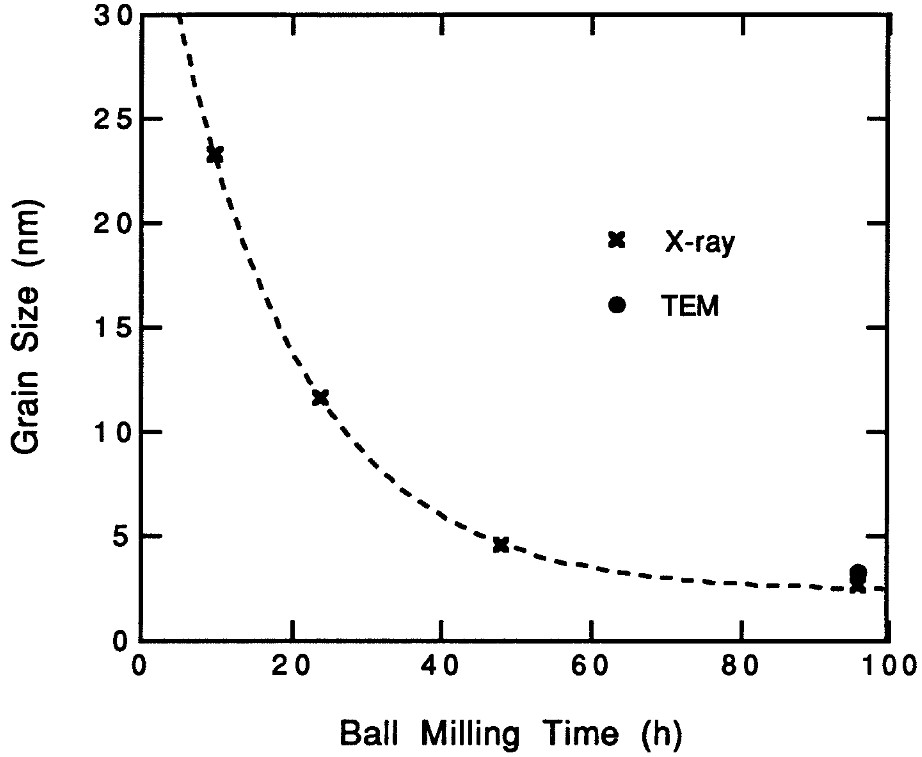

Figure 3.8. Crystallite size of Cr-18.5 % Fe filings versus ball milling time, as determined by x-ray line broadening (crosses) and TEM (circle).

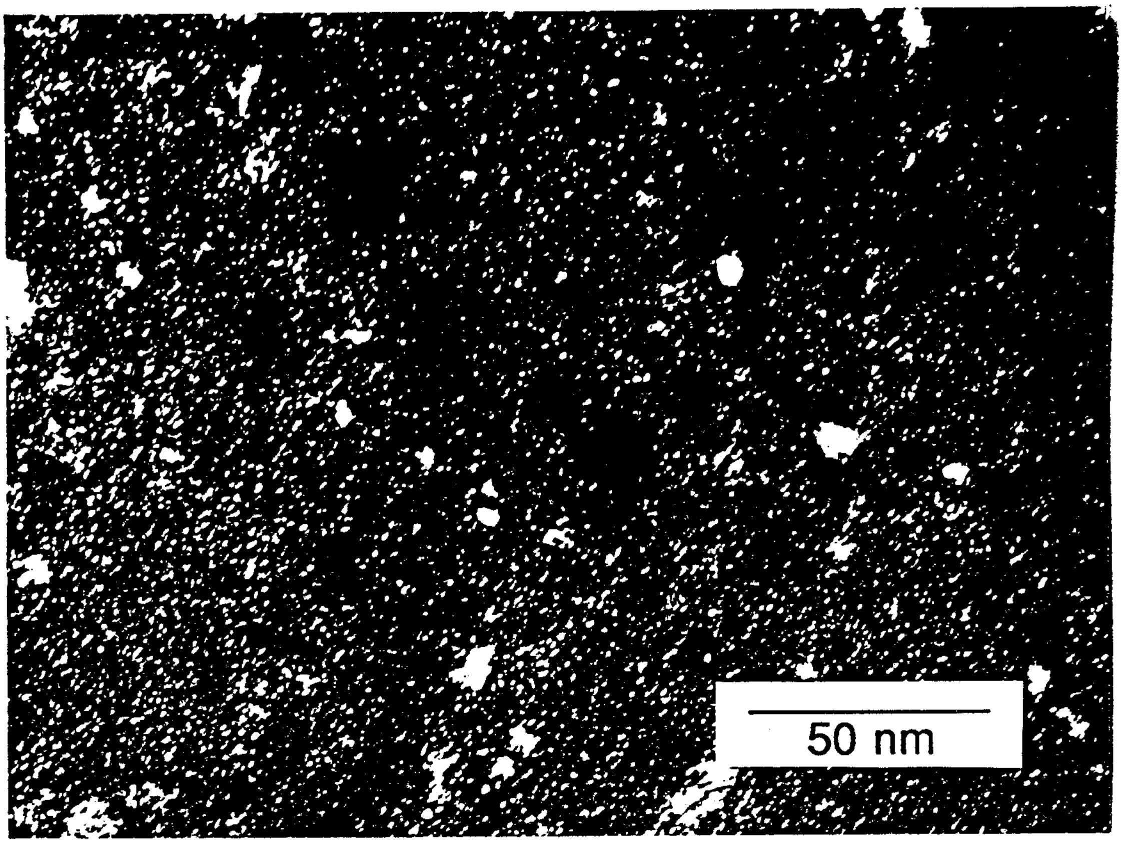

Figure 3.9. TEM micrograph of initially Cr-18.5 % Fe powders after ball milling for 96 hours. This dark field image was made from a (110) bcc diffraction.

References for Chapter 3

1. H. Kuwano, H. Ouyang and B. Fultz, Nanostructured Materials, **1**, 143 (1992).

2. H. Kuwano, H. Ouyang and B. Fultz, Materials Science Forum, **88-90**, 561 (1992).

3. H. Ouyang, B. Fultz and H. Kuwano, "Grain Boundary Widths of Four FCC and BCC Nanophase Alloys Prepared by Mechanical Attrition," Submitted to TMS 1992 Spring Conference.

4. J. Ballon, V. Comparat and J. Pouxe, Nucl. Instrum. Methods, **217**, 213 (1983).

5. H. P. Klug and L. E. Alexander, X-Ray Diffraction Procedures (John Wiley, New York, 1974), p. 661-665.

6. B. E. Warren, X-Ray Diffraction (Dover, New York, 1990), p. 257-274.

7. B. E. Warren and B. L. Averbach, J. Appl. Phys., **21**, 595 (1950).

8. R. Delhez, Th. H. de Keijser, E. J. Mittemeijer and J. I. Langford, Aust. J. Phys., **41**, 213 (1988).

9. B. Fultz, G. Le Caër, and P. Matteazzi, J. Mater. Res., **4**, 1450 (1989).

10. C. Michaelsen and E. Hellstern, J. Appl. Phys., 62, 117 (1987).

11. P. Matteazzi and G. Le Caër, J. Am. Ceram. Soc., **74**, 1382 (1991).

12. H. Kuwano, H. Ouyang and B. Fultz, Nanostructured Materials, **1**, 143 (1992).

13. G. Le Caër, P. Matteazzi, and B. Fultz, "A Microstructural Study of the Mechanical Alloying of Fe and Sn Powders," J. Mater. Res., in press.

14. G. Le Caër and J. M. Dubois, J. Phys. E, **12**, 279 (1979).

15. U. Herr, J. Jing, R. Birringer, U. Gonser, and H. Gleiter, Appl. Phys. Lett. **50**, 472 (1987).

16. Editor Leopold May, An Introduction to Mössbauer Spectroscopy (Plenum Press, New York-London, 1971), chapter 2 by Jon J. Spijkerman.

17. Editor U. Gonser, Mössbauer Spectroscopy (Springer-Verlag, New York, Heidelberg Berlin, 1975), chapter 1 by U. Gonser.

18. Guy K. White, Experimental Techniques in Low-Temperature Physics (Clarendon Press, Oxford, 1979).

19. L. H. Schwartz in Applications of Mössbauer Spectroscopy Vol. I, R. L. Cohen, ed., Academic Press, New York (1980), p. 37.

20. U. Herr, J. Jing, R. Birringer, U. Gonser, and H. Gleiter, Appl. Phys. Lett., **50**, 472 (1987).

21. J. Jing, A. Krämer, R. Birringer, H. Gleiter and U. Gonser, J. Non-Cryst. Solids, **113**, 167 (1989).

22. Simon Foner, Rev. Sci. Instrum., **30**, 548 (1959).

23. D.G. Rancourt and P. Hargraves, Nucl. Instrum. Methods B, **44** (2), 199 (1989).

24. B. Fultz, Diffraction Theory with Applications to Transmission Electron Microscopy and X-Ray Diffractometry Vol. II, course notes for Aph /Ms 122 at caltech (1991).

25. A. G. Khachaturyan, Sov. Phys. Cryst., **5**, 335 (1960).

26. M. L. Trudeau and R. Schultz, Materials Science and Engineering, **A134**, 1361 (1991).

27. R. W. Siegel, Annu. Rev. Mater. Sci. , **21**, 559 (1991).

Chapter 4 Hyperfine Magnetic Fields and Magnetic Properties of Nanophase Fe-Alloys

In this chapter some experimental results on magnetic properties are discussed. The hyperfine magnetic field (HMF) distributions of four Fe-alloys, Cr-Fe, Fe-Mn, Ni-Fe and Fe-Ti, are described in § 4.1. Debye temperatures obtained from Mössbauer recoil-free fraction and second order Doppler shift measurements for Cr-Fe nanophase are described in § 4.2. In § 4.3 the results from magnetization curve measurement of Cr-Fe are described. The superparamagnetic behavior of nanophase Cr-Fe is described in § 4.4.

4.1 Bimodal Hyperfine Magnetic Field Distribution

Several methods have been proposed to evaluate hyperfine parameter distributions from unresolved Mössbauer spectra of many overlapping lines (1-4). In this work, the method of Le Caër and Dubois was employed (5), by which the hyperfine magnetic field distributions are obtained from the raw experimental spectra by the curve-fitting with many known spectra.

Room temperature Mössbauer spectra of filings from the Cr-18.5 % Fe ingot before and after ball milling are presented in Figure 4.1. Significant broadening of the initially paramagnetic peak occurs, and the original symmetric peak develops a positive skewness. These changes in lineshape are larger than those typically caused by isomer shift or electric quadrupole effects in paramagnetic alloys, and at the same time the material became

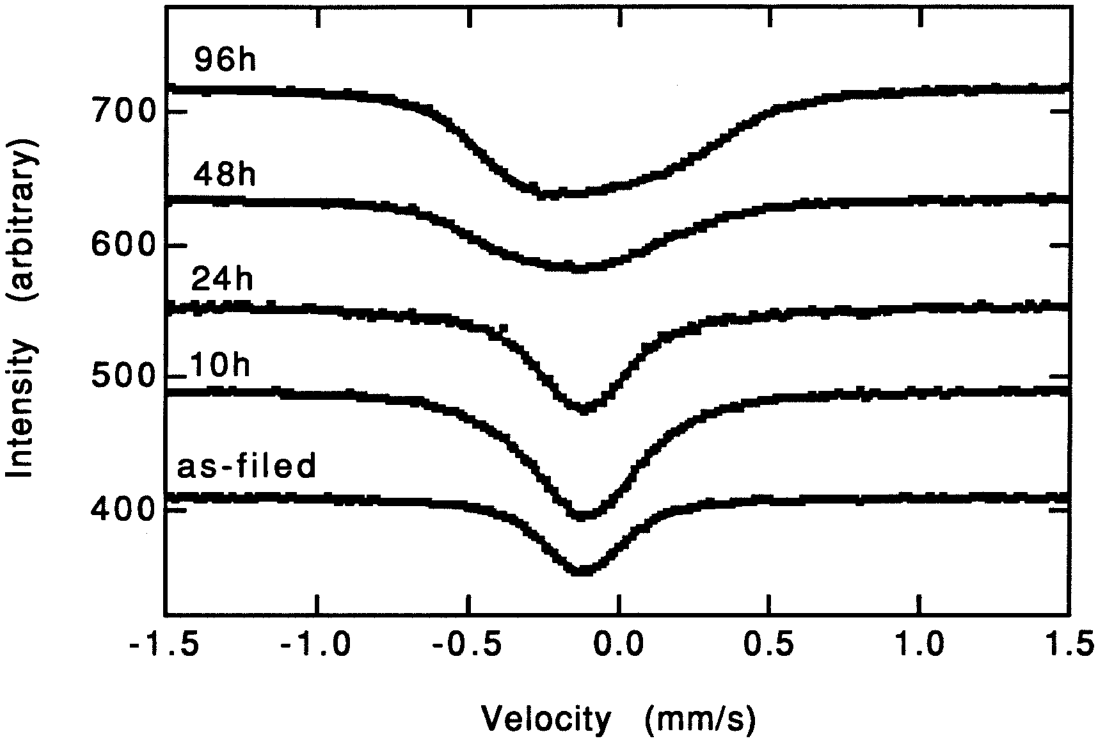

Figure 4.1. Mössbauer spectra of the Cr-18.5 % Fe filings after ball milling for various times.

increasingly ferromagnetic, as evidenced by its attraction to a permanent magnet. Therefore the line broadening can be attributed to changes in the hyperfine magnetic field in the material, and more evidence is presented in § 4.3. The HMF distributions of ball milled powder , presented in Figure 4.2, show two components — one centered at 7- 8 KG and the other centered at 20 KG. These two components are well-separated in HMF, and this separation was obtained consistently even when we used different values for the radiation source lineshape, or different relationships between the isomer shift and HMF. The ^{57}Fe nuclei contributing to the high field component of the HMF distribution are those nuclei responsible for the growth in skewness of Mössbauer spectra. It is this high field component of the HMF distribution which grows as the crystallite size decreases.

The reason for the broadening of the Mössbauer spectrum was studied by applying an external magnetic field to the specimen. Mössbauer spectra from Cr-Fe powder ball-milled for 96 hrs were obtained with and without applying a magnetic field of 0.2 T. The absorption peak obtained with the magnetic field was slightly sharper than that without the applied magnetic field. Since the direction of the hyperfine field at the ^{57}Fe nucleus is opposite to that of the lattice magnetization (6), the observed Mössbauer spectrum is expected to become narrowed if a HMF larger than 0.2 T exists in the sample. If the sample is paramagnetic, the spectrum is expected to become broadened with the applied external magnetic field.

Energy dispersive x-ray analysis and electron microprobe analysis showed that during ball milling, the powder became enriched in Fe. The Fe contamination came from the hardened steel balls and inside of vial. The Fe concentration of Cr-Fe is presented in Figure 4.3 as a function of ball milling time. Similar trends were observed in other alloy systems. Because the

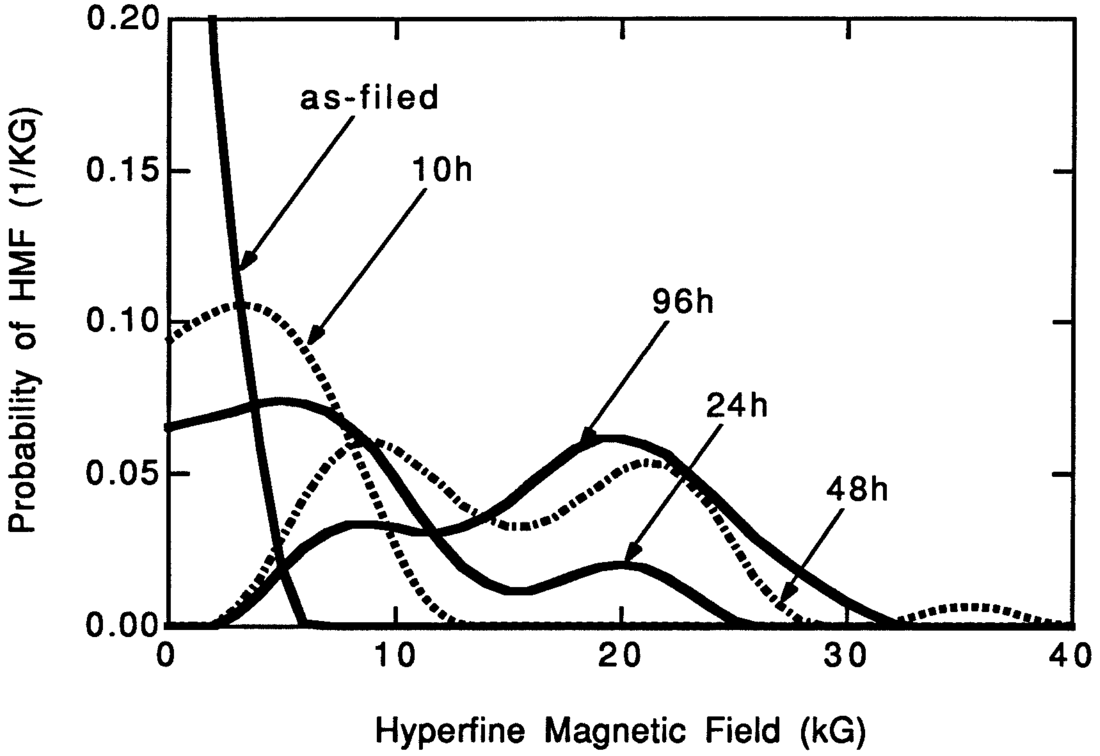

Figure 4.2. Hyperfine magnetic field distributions obtained from the spectra presented in Figure 4.1.

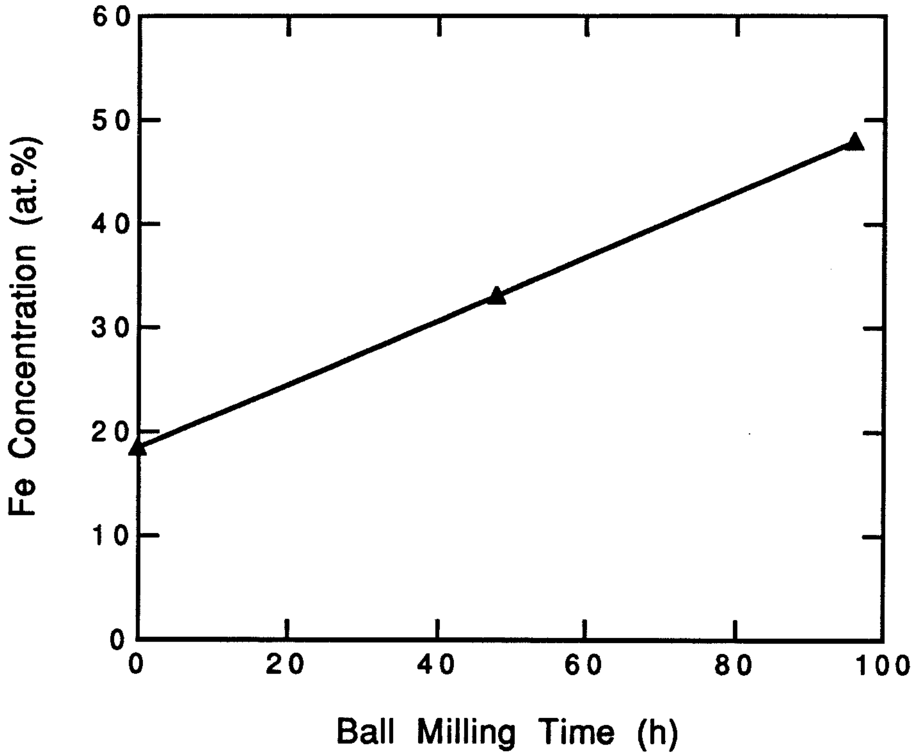

Figure 4.3. Fe concentration of initially Cr-18.5 % Fe filings versus ball milling time, which was determined by the electron microprobe.

chemical composition of the powders was changing as the crystallite size decreased with the ball milling time, we also studied powders that underwent grain growth during annealing. Such studies are also useful for estimating possible effects of grain boundary segregations, which will probably become larger during annealing. In one series of experiments we used the Cr-18.5 % Fe filings that were ball milled for 48 hrs, during which their chemical composition changed to Cr-35 % Fe. As the crystallite size grew from 4.5 nm to 8 nm after 6 hours of annealing at 300 °C, the fraction of the high field peak fell from about 45 % to 35 %, in good agreement with the changes that occurred during the initial milling. With further annealing this trend continued, but an additional high field peak appeared in the HMF distribution, which may originate from Fe-rich regions that form during spinodal decomposition of the alloy. To suppress the formation of this high field peak during annealing, we used powder with a lower Fe concentration of about 22 %, prepared by ball milling filings of pure Cr for 96 hours. This material had an initial crystallite size of 5 nm, which grew to 10 nm during annealing at 300 °C. The HMF distributions presented in Figure 4.4 show a reduction in intensity of the high field component as the crystallite size of this powder increased during annealing. This trend is shown quantitatively in Figure 4.5 (triangles), together with similar data obtained from the Cr-18.5 % Fe filings during ball milling (circles).

We used the same method to analyze Mössbauer spectra from alloys of Fe-Mn, Fe-Ti, and Ni-Fe. Room temperature Mössbauer spectra from filings of the Fe-45 % Mn ingot before, during, and after ball milling are presented in Figure 4.6. At room temperature, Fe-Mn is weakly antiferromagnetic (6), so the apparent doublet in the as-filed spectrum is actually a sextet of overlapping peaks. Figure 4.7 shows a single peak in the HMF distribution at

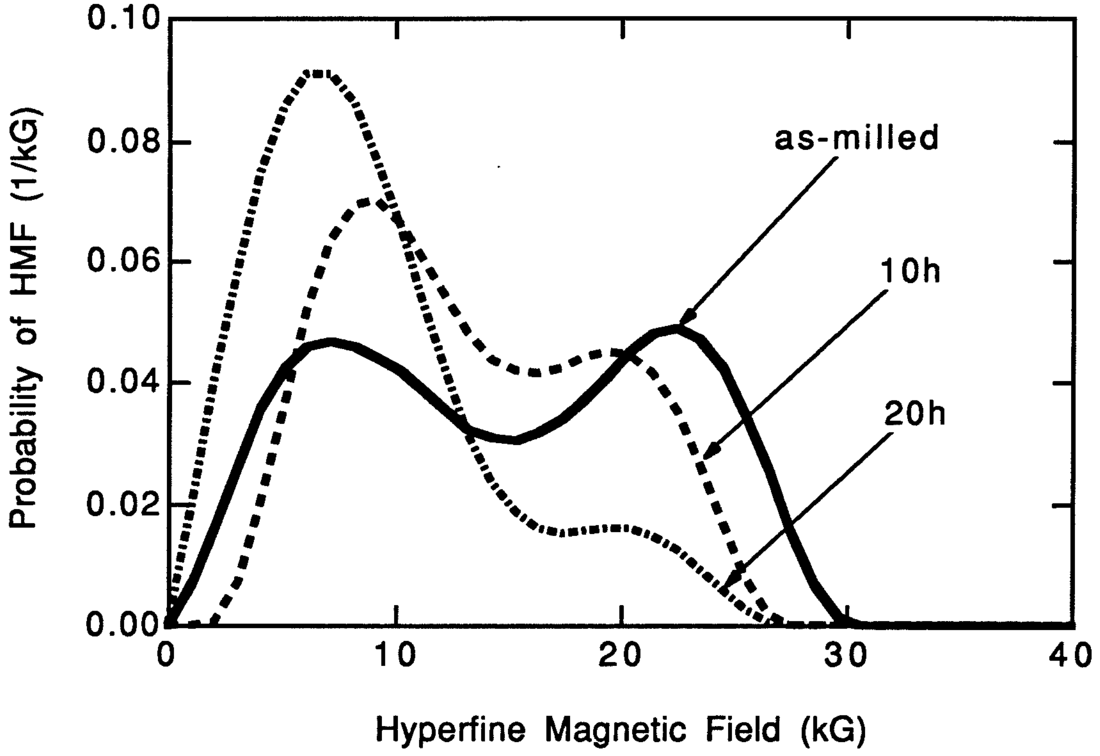

Figure 4.4. Hyperfine magnetic field distributions obtained from Cr filings ball-milled 96 h to produce a nanophase Cr-22 % Fe alloy, and annealed at 300 °C for various times.

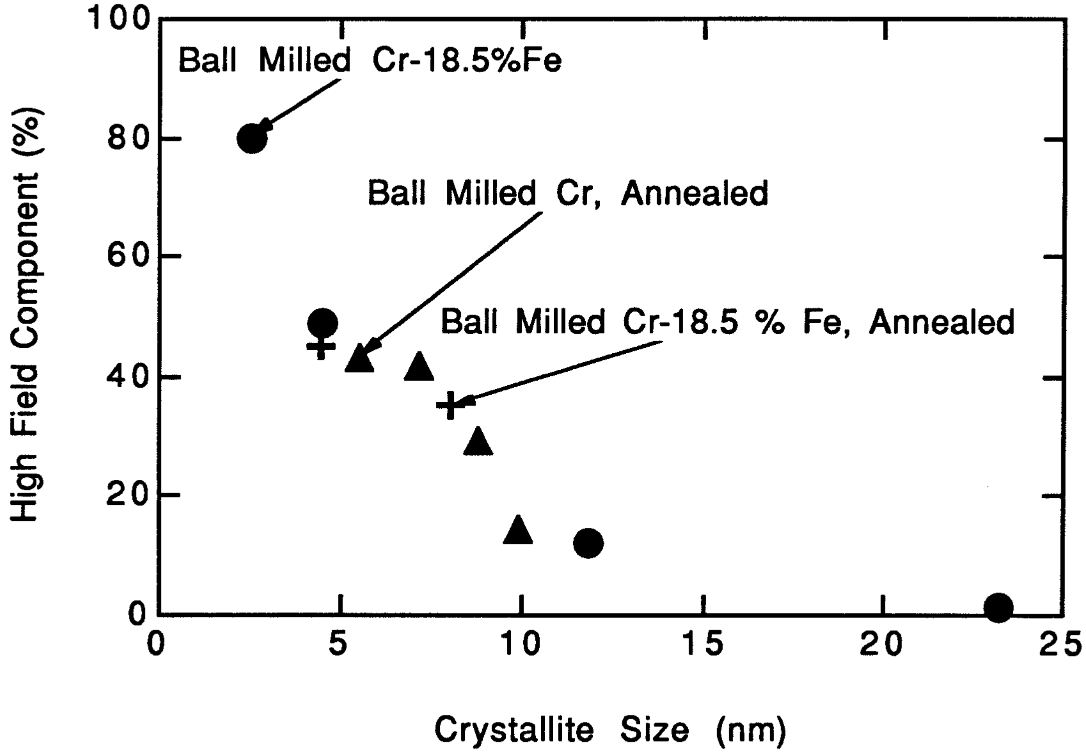

Figure 4.5. Percentage of high field HMF component versus crystallite size. Circles: Cr-18.5 % Fe filings after ball milling for various times. Crosses: Same material annealed at 300 °C. Triangles: Cr powders ball milled to produce Cr-22 % Fe powders, then annealed at 300 °C.

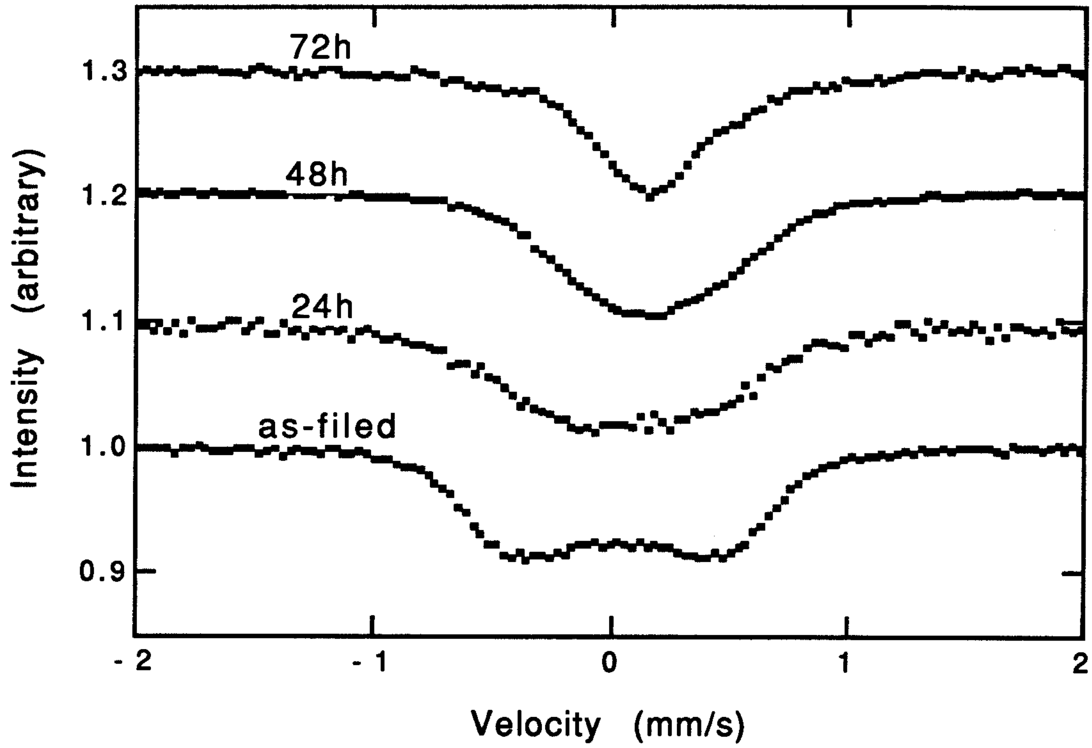

Figure 4.6. Mössbauer spectra of Fe-45 % Mn after ball milling for the times as labelled.

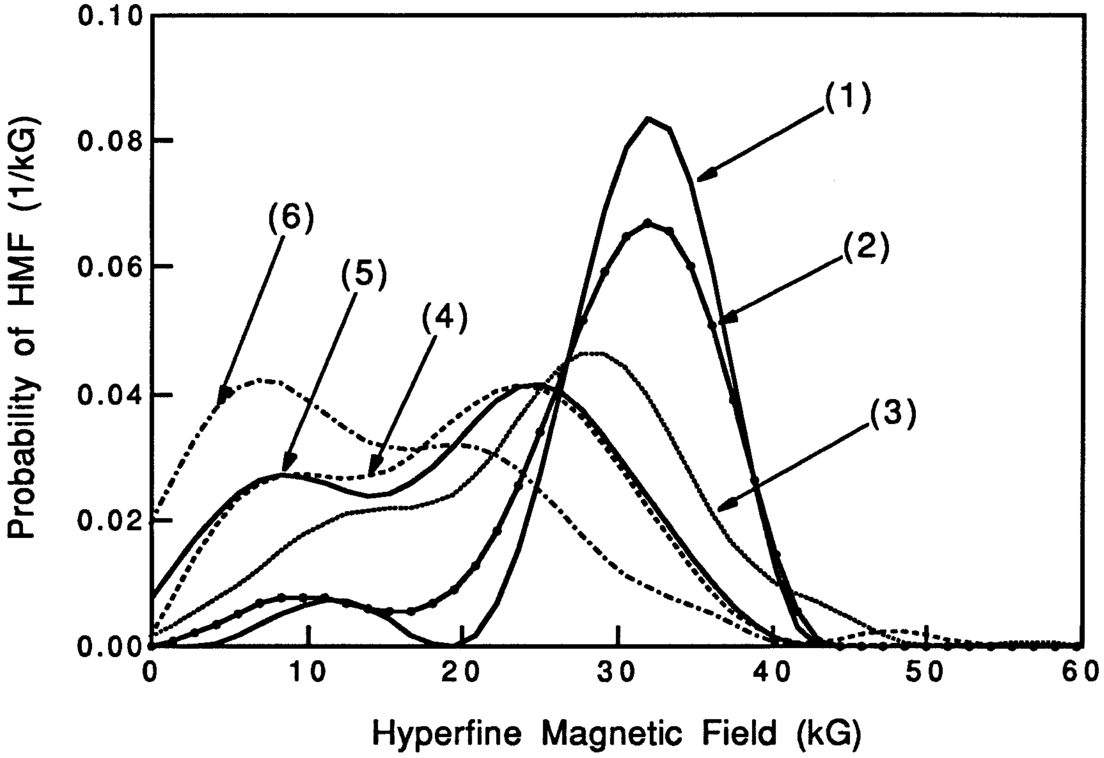

Figure 4.7. Hyperfine magnetic field distributions of Fe-Mn powders with different grain sizes. Increasing numbers denote decreasing grain sizes, obtained with these processings: 1) as-filed. 2) milled 24 h under H_2 gas. 3) milled 24 h under Ar gas. 4) milled 48 h under Ar gas. 5) milled 72 h under Ar gas. 6) milled 96 h under Ar gas.

about 32 kG for the as-filed material. Other HMF distributions of ball-milled Fe-Mn powder, obtained with the same equipment lineshape and smoothing parameter, are also presented in Figure 4.7. Although there is some downwards shift of the crystalline antiferromagnetic component with ball milling time, two components are still resolved – one centered around 10 kG and the other centered around 30 kG. These two components are well-separated in HMF, and this separation was obtained even when we used different values for the radiation source linewidth, or different relationships between the isomer shift and HMF. The ^{57}Fe nuclei contributing to the low field component of the HMF distribution are those nuclei responsible for the narrowing of the Mössbauer spectra in Figure 4.6. It is this low field component of the HMF distribution which grows as the crystallite size decreases, so it is this component that we attribute to ^{57}Fe atoms situated at or near grain boundaries.

Following similar procedures, room temperature Mössbauer spectra from filings of the Fe-50 % Ti and Ni-25 % Fe ingot before, during, and after ball milling are presented in Figure 4.8 and 4.9. The changes of raw spectra of Fe-Ti are like those of Cr-Fe. Therefore, it is not surprising that both of the HMF distributions are similar, and the HMF distributions of Fe-Ti show two components – one peak centered around 10 kG and another peak centered at 20 kG. For Fe-Ti it is the high field component that we attribute to the ^{57}Fe atoms at and near grain boundaries. Alloys of Ni-Fe are strongly ferromagnetic at room temperature, with the HMF distribution extending to 350 kG (Figure 4.10). A broad, intermediate field component in the ^{57}Fe HMF distribution from Ni-Fe was attributed to the ^{57}Fe atoms at and near grain boundaries. I have prepared many alloys by mechanical attrition (Table 4.1). Only the four alloys: bcc Cr-Fe, bcc Fe-Ti, fcc Fe-Mn, and fcc Ni-Fe achieved the

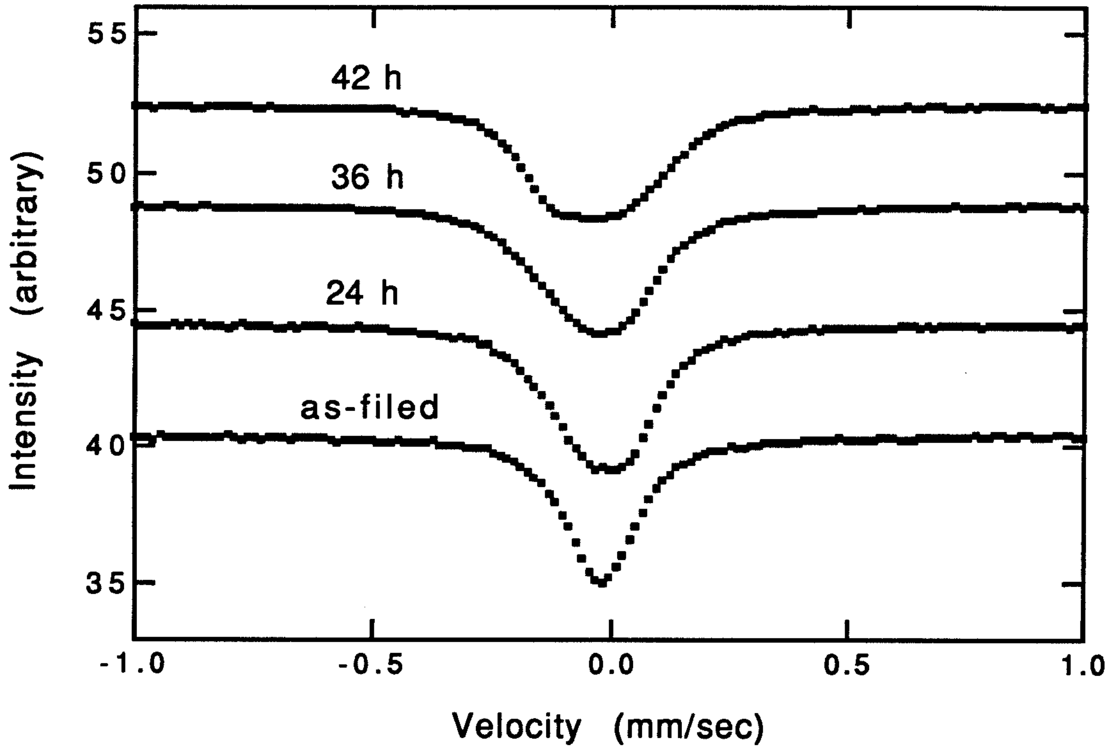

Figure 4.8. Mössbauer spectra of Fe-50 % Ti after ball milling for the times as labelled.

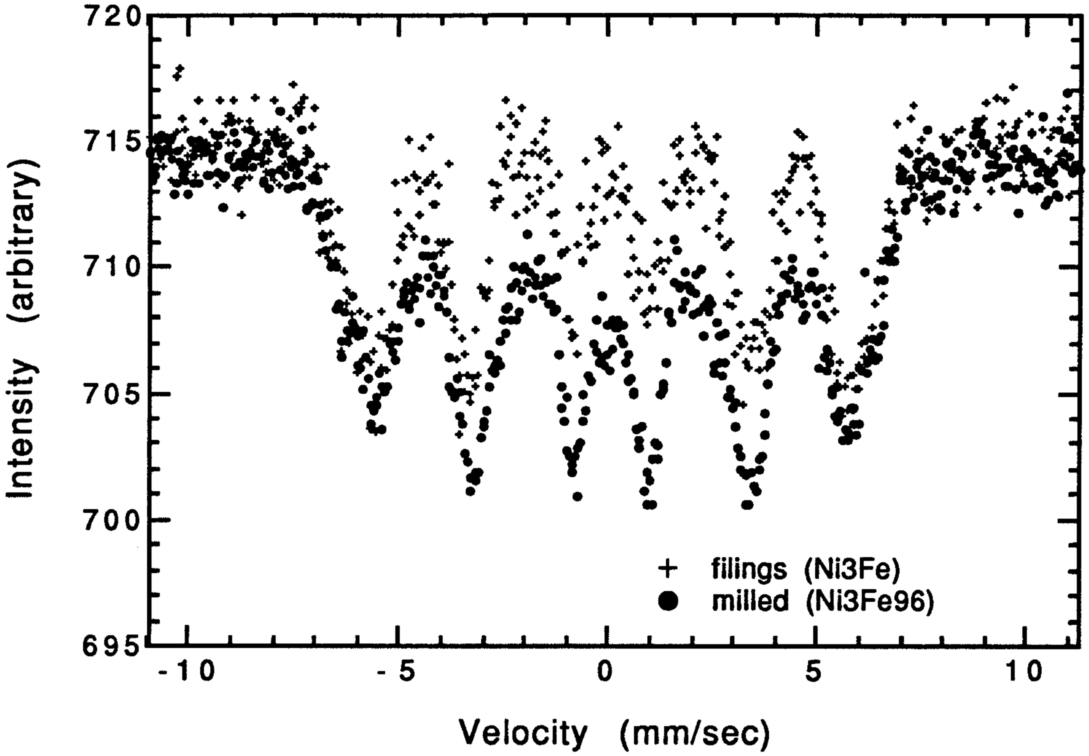

Figure 4.9. Mössbauer spectra of Ni-25 % Fe before ball milling and ball milled for 96 hours.

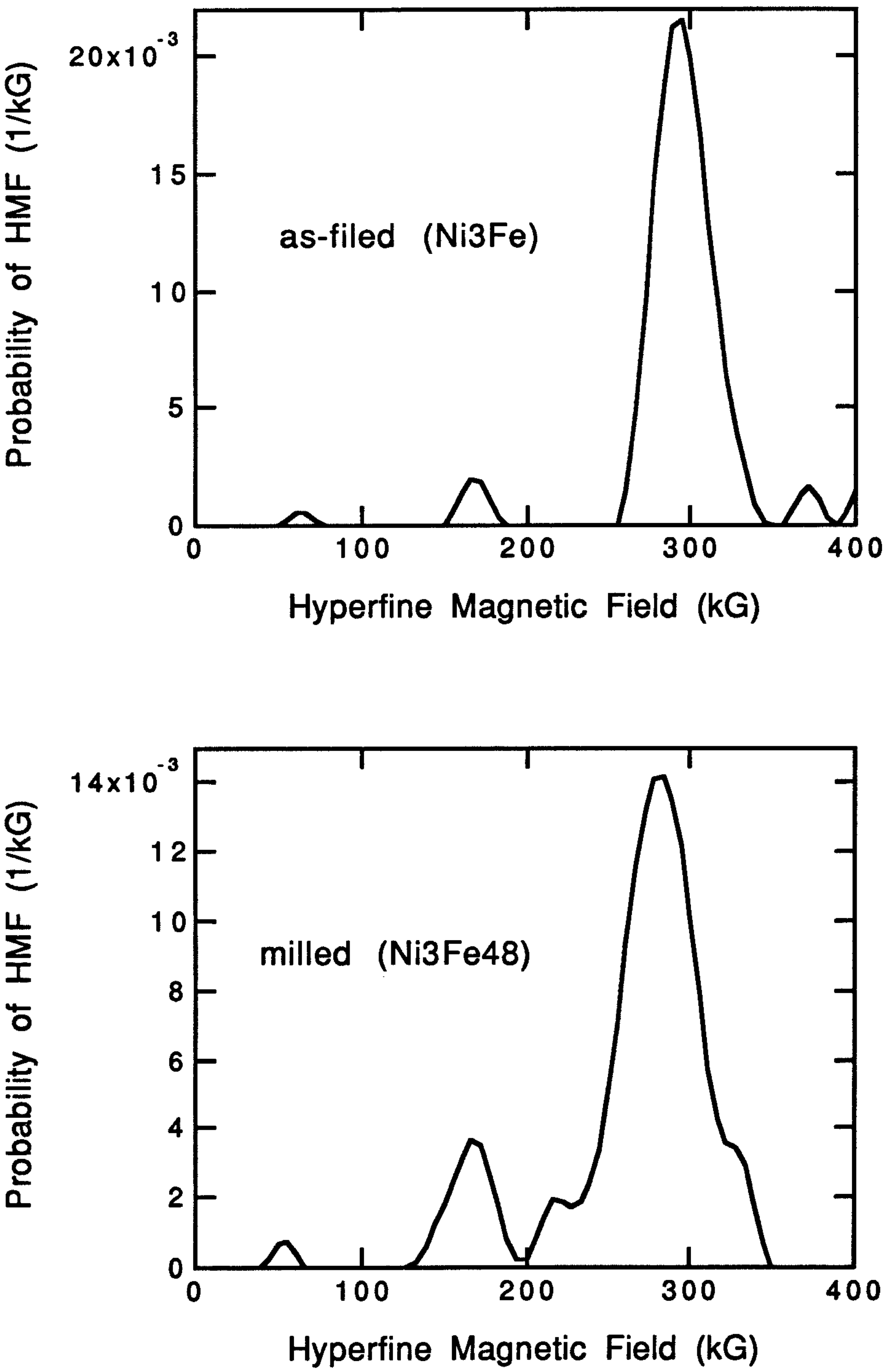

Figure 4.10. Hyperfine magnetic field distributions obtained from the Mössbauer spectra of Ni-Fe before ball milling (upper) and ball milled (lower) for 48 hours. After ball milling, a broad, intermediate field component in the ^{57}Fe HMF distribution developed.

Metal or Alloy	Ball Milling Time (hour)	Average Grain Size (nm)
Cr-18.5 % Fe	96	3
Ni-50 % Al	156	10
Ni-25 % Fe	96	5
Fe	96	12
Fe-50 % Ti	96	3
Fe-50 % Co	120	19
Fe-50 % Mo	120	13
Fe-25 % Al	10	10
Fe-45 % Mn	96	5
Fe-20 % V	96	7
Fe-40 % V	48	amorphous
Fe-5 % Zr	30	9
Fe-10 % Zr	30	amorphous
Fe-10 % Zn	48	16
Fe-25 % Sn	48	11
Fe-10 % Nb	48	14
Fe-10 % B	24	10
Fe-28 % Al-5 % Cr	8	9

Table 4.1. Ball milling results for metals and alloys

smallest grain size. These were also the alloys which showed well-resolved grain boundary components in the HMF distributions. Although we ball-milled alloys of many other compositions, if we did not achieve grain size of 7 nm or less, we did not find a clear magnetic signature of the ^{57}Fe atoms at or near grain boundaries. However, a magnetic signature from bcc alloys could be seen at grain sizes larger than 7 nm.

Because the Fe concentration of the powders of Fe-Mn, Ni-Fe and Fe-Ti increased with milling time, we also studied powders that underwent grain growth during annealing. Unfortunately, our attempts at grain growth experiments with Fe-Mn were not successful because of the formation of an intermetallic compound during annealing. We had better success with grain growth experiments with Ni-Fe, and Fe-Ti, which were annealed at 300 °C. As the crystallite size of these two alloys grew after several hours of annealing, the fraction of the high field component in the HMF distributions of Fe-Ti decreased, and the low field component of Ni-Fe decreased. These changes of grain size during annealing were in good agreement with the changes during the ball milling. This trend continued with further annealing, and data from these grain growth experiments are included in Figure 4.11 and 4.12. In both figures, the data from the powders milled for different times are presented as solid circles, and the data from milled powders that were subsequently annealed in grain growth experiments are presented as solid triangles. The data from these two types of experiments lie on a common curve, indicating that the controlling variable in all of these materials is the grain size and not, for example, chemical heterogeneities.

Figure 4.13 includes results from Figure 4.5, 4.11, 4.12 and the change of low field component of Fe-Mn of the HMF distributions versus grain size. The results of Figure 4.13 strongly imply that the high field component of

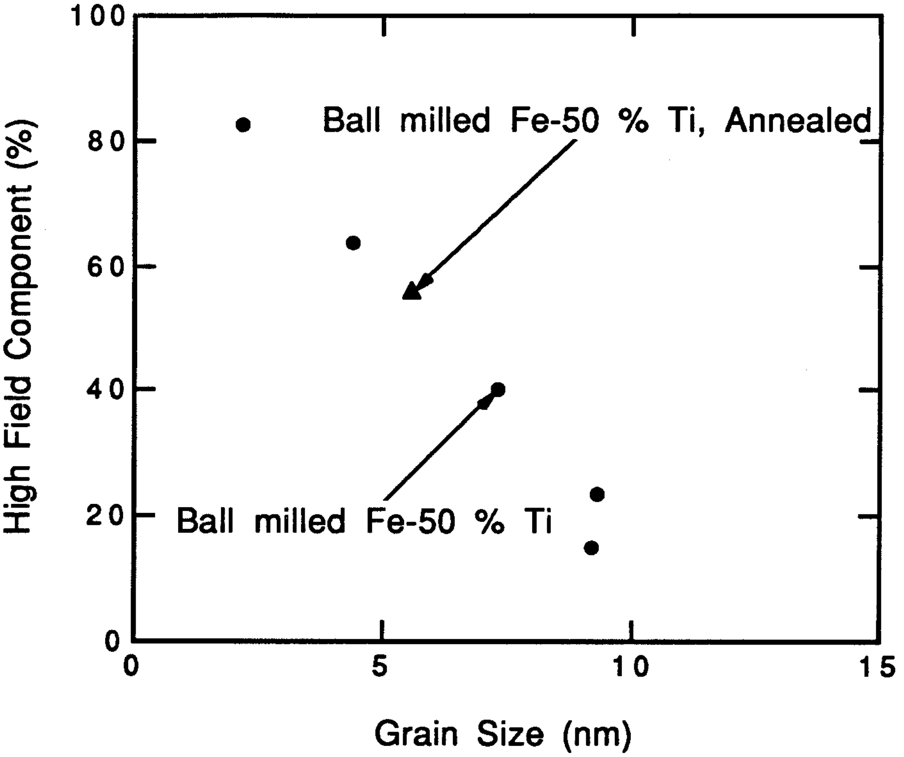

Figure 4.11. Percentage of high field HMF component versus crystallite size. Circles: Fe-50 % Ti filings after ball milling for various times. Triangles: Material milled for 96 hours, then annealed at 300 °C for various times.

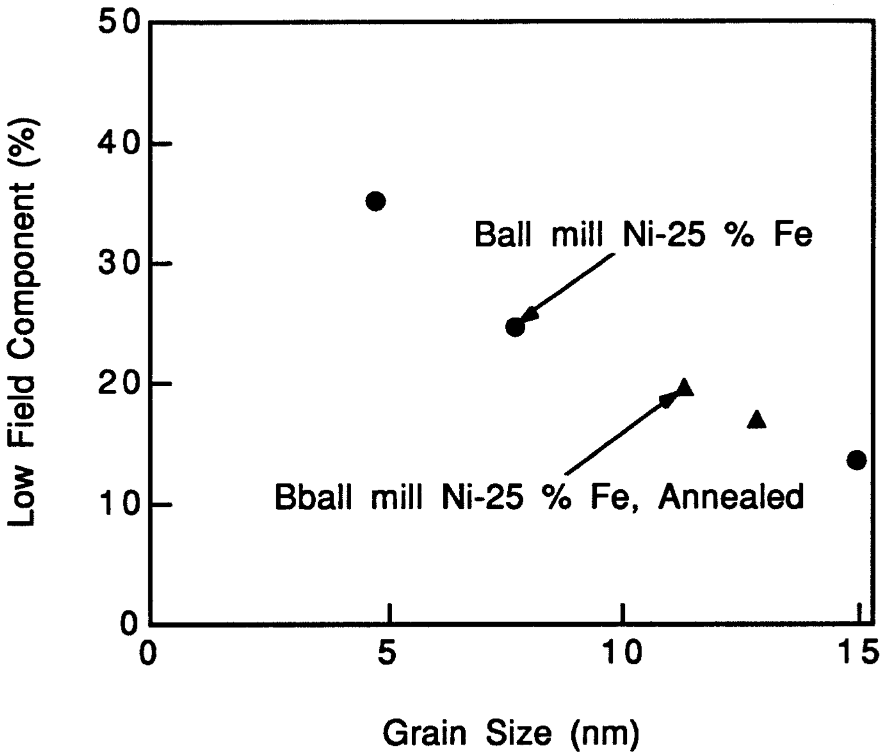

Figure 4.12. Percentage of low field HMF component versus crystallite size. Circles: Ni-25 % Fe filings after ball milling for various times. Triangles: Material milled for 96 hours, then annealed at 300 °C for various times.

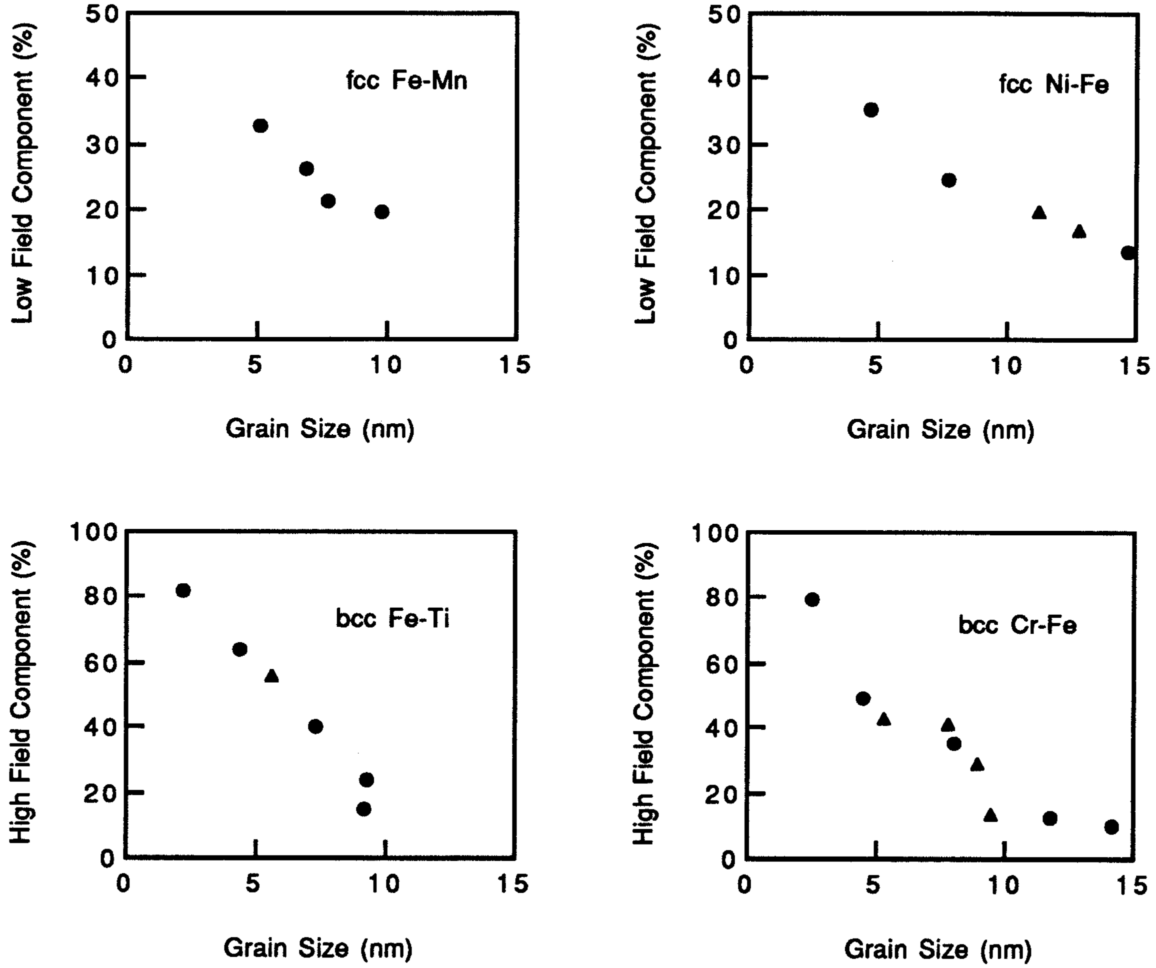

Figure 4.13. (upper) Percentage of low field component versus crystallite size. (lower) Percentage of high field component versus crystallite size. Circles: Materials after ball milling for various times. Triangles: Materials milled for 96 hours, then annealed at 300 °C for various times.

Cr-Fe and Fe-Ti, and the low field component of Fe-Mn and Ni-Fe of the HMF distribution originates with ^{57}Fe atoms at and near grain boundaries.

It seems unlikely that the two components in the HMF distribution are distinguished by differences in their chemical environment since the two sets of data in Figure 4.13 show similar trends, even though the alloy compositions are different; the change of the lattice constant versus the composition could determine the occurrence of the chemical segregation. However, the broadening of the diffraction peak and the change of strain with different milling times limit the accuracy of this method. In our work, the abrupt change of the lattice constant versus the composition was not observed; diffusion is necessary for chemical segregation to occur. The heat of mixing is a important factor in the diffusion process, which can determine how fast the atom moves between different phases. The strongly different heats of mixing of Cr-Fe, Fe-Ti, Fe-Mn and Ni-Fe (8) also suggest that the similar trends of the data in Figure 4.13 were not due to chemical segregation.

A "magnetic signature" of the ^{57}Fe atoms at grain boundaries is not surprising; magnetic moments and hyperfine magnetic fields are known to be sensitive to differences in atomic displacements and coordinations, and the differences in displacements and coordinations for ^{57}Fe atoms at grain boundaries and for ^{57}Fe atoms in regions of good crystal are expected to be large. We do not hope to predict the magnetic signature a-priori (even if we assume the local atomic arrangements at the grain boundaries). We settle instead for a phenomenological understanding that the high (or low) field component of the ^{57}Fe HMF corresponds to ^{57}Fe atoms at grain boundaries, or close enough to the grain boundaries to have a perturbed HMF. The range of influence of a grain boundary is probably rather short for Fe-transition metal alloys, since the 3d-electron rearrangements responsible for extending the magnetic disturbance into the crystal have characteristic lengths of at most few atomic distances (9-11). Nevertheless, it is important to consider how the "magnetic width" of the grain boundary may extend into the crystallites. A previous Mössbauer spectrometry study of pure Fe nanocrystals (12) found an unexpectedly large fraction of 57Fe atoms with perturbed HMF's, indicating a large magnetic width of perhaps 2 nm. In this previous work, however, the HMF of the grain boundary atoms was not well-resolved from that of atoms in the crystallites, so the edge of the magnetic disturbance near grain boundary was more gradual. In our materials of Cr-Fe, Fe-Ti, Fe-Mn, and Ni-Fe, the components of the HMF are well-resolved, indicating that the magnetic environments at the grain boundaries and in the crystallites are distinctly different. This supports our contention that the fraction of ^{57}Fe atoms with the grain boundary signature corresponds well to the fraction of atoms with at least some of their first-nearest-neighbor atoms in non-crystalline configurations. The "magnetic width" of the grain boundary should correspond reasonably well to the physical width of the grain boundary, although the magnetic width may be larger. The magnetic width of the grain boundary can be determined from the data on the fraction of ^{57}Fe atoms at grain boundaries (Fig. 4.13) if the grain boundary fraction for a material with a given crystallite size can be estimated. It is possible to obtain this information easily with a simple geometrical model of spherical grains in which the grain boundary width is twice the width of a shell on the surface of a spherical particle, but this model ignores the effects of the crystallite size distributions.

4.2 Debye Temperature

The Debye temperature can be taken as a physical parameter of the vibrational spectrum of a solid. It is not surprising that the Debye temperatures of nanophase and polycrystal materials are different since their atomic structures are expected to be different.

Mössbauer recoil-free fraction experiments (12-14) measure the resonant absorption of the complete sample by means of evaluation of the area under the absorption lines over a range of temperature, usually from liquid helium temperature to room temperature.

The quantity of resonant absorption is proportional to recoil-free fraction f (Chapter 2):

$$f = \exp\left\{ -\frac{6E_r}{k_B\theta_D} \left[\frac{1}{4} + \left(\frac{T}{\theta_D}\right)^2 \int_0^{\frac{\theta_D}{T}} \exp\left(-\frac{x}{e^x - 1}\right) dx \right] \right\},$$

where

E_r = recoil energy of the free atom

k_B = Boltzmann's constant

T = temperature

θ_D = Debye temperature.

Differences in f between nanocrystalline and polycrystal materials result from different phonon spectra in the crystalline and grain boundary regions. Since the consumption rate of liquid helium was very high in our experiment, and the vibrations caused by the long tubing in the cryostat were large, the experiment could not last very long around liquid helium temperature, and it was hard to repeat the results. Similar experiments were done in Japan by one of our co-workers (15). Both results for our nanophase Cr-Fe are shown in Figure 4.14. A Debye temperature of 397 K was obtained, which was lower in comparison to the bulk Debye temperature of 470 K. Due to the uncertainty of the interfacial layer thickness at the direction perpendicular to incident γ-ray, no attempt was made to determine a separate Debye temperature for the grain boundary component with the recoil-free fraction data of Mössbauer spectroscopy.

Another analysis was performed to obtain the Debye temperatures of Cr-Fe in the crystalline and grain boundary regions. Isomer shifts can be obtained from HMF distributions (5). The temperature dependences of the isomer shifts (actually second order Doppler shifts) of 96 hr ball milled powders and as-filed powders are shown in Figure 4.15. From § 4.1, the HMF distributions are composed of two components: grain boundary and crystalline components, i.e., a bimodal distribution was observed. The isomer shifts of the grain boundary and the crystalline parts of the HMF distributions can be obtained individually. Recall that the second order Doppler shift (Chapter 2), S_{sods}, is:

$$S_{sods} = -\frac{1}{2c}\left(\frac{9k_B\theta_D}{8M} + \frac{9k_BT}{M}\left(\frac{T}{\theta_D}\right)^3 \int_0^{\frac{\theta_D}{T}} \frac{x}{e^x - 1}\,dx\right), \qquad \text{(Eq. 4.1)}$$

where

c = speed of light

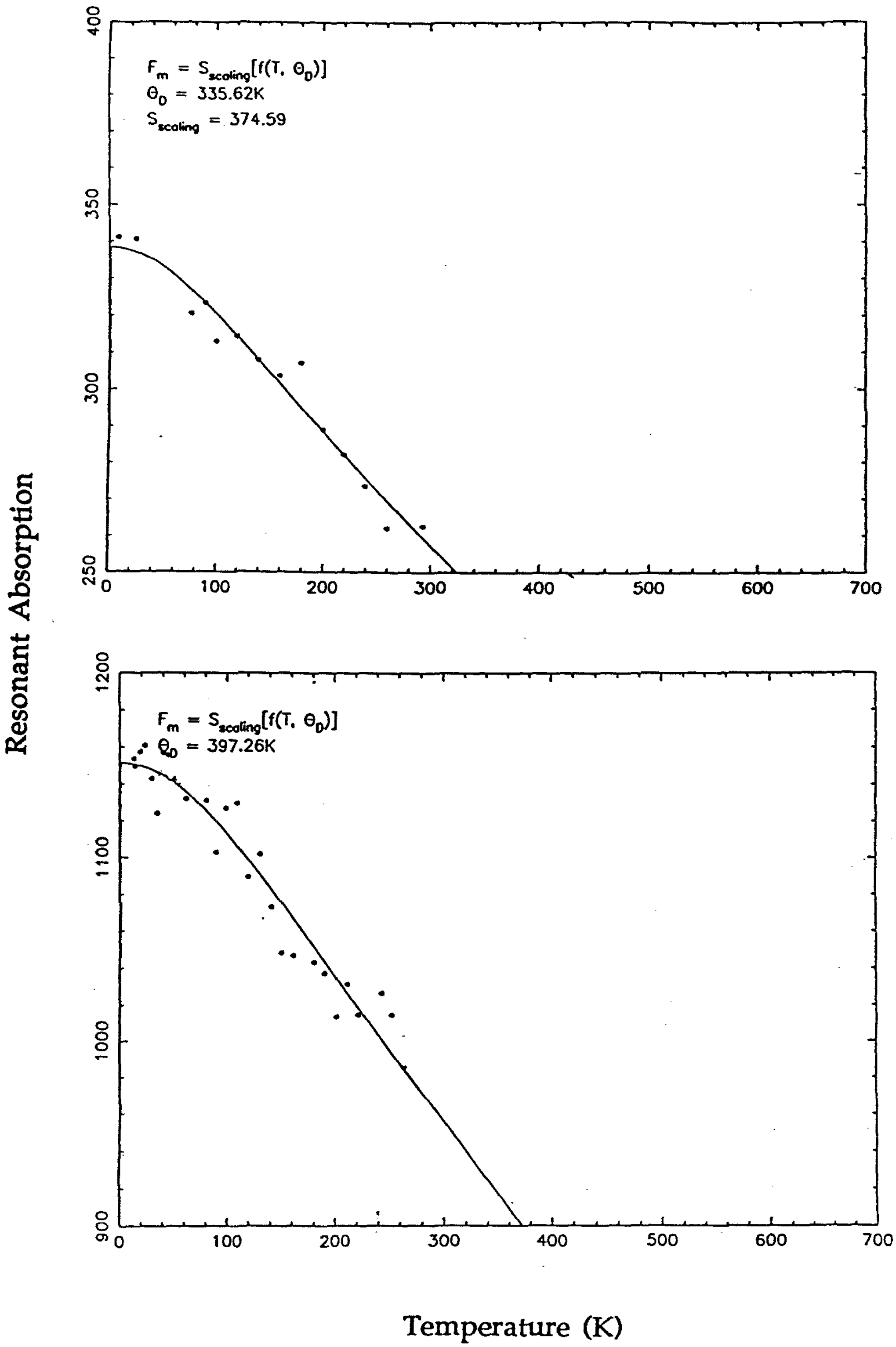

Figure 4.14. Fit of the total resonant absorption. Lower plot was obtained in Japan (13).

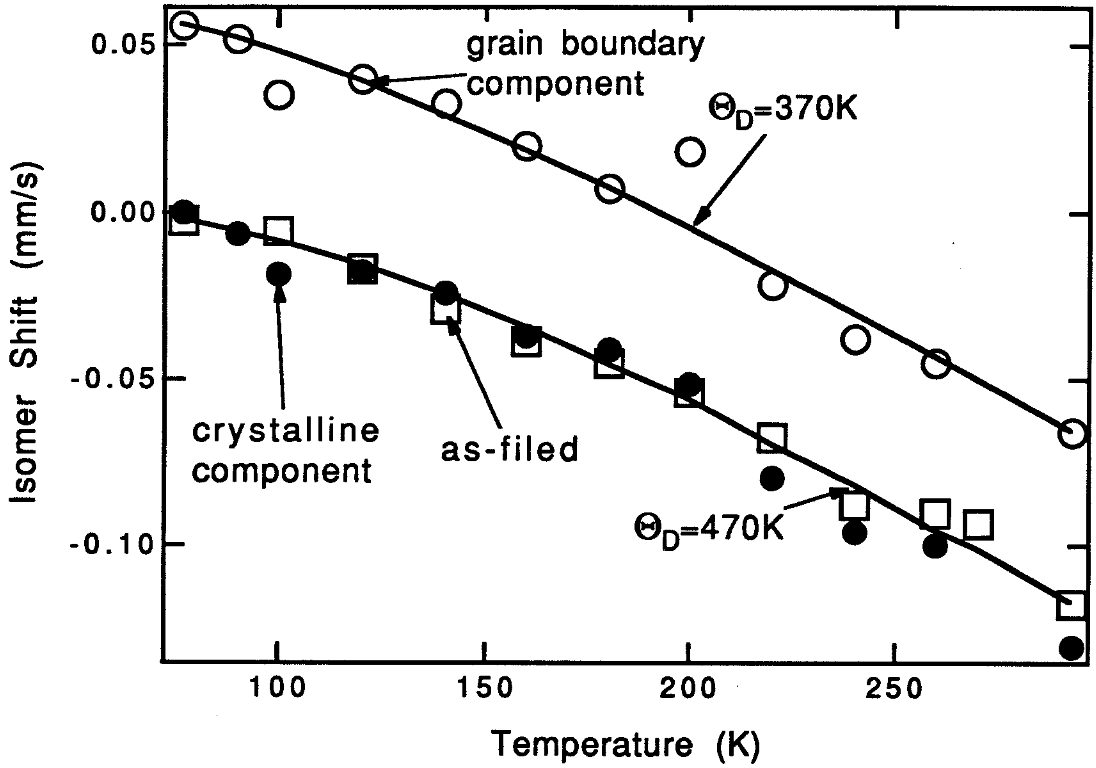

Figure 4.15. Temperature dependences of isomer shifts. Circles: Isomer shifts of Cr-Fe powders ball-milled for 96 h. Squares: Isomer shifts of the as-filed Cr-Fe sample.

k_B = Boltzmann's constant

θ_D = Debye temperature

M = mass of ^{57}Fe atom.

Data in Figure 4.15 were curve-fitted by equation 4.1 plus a constant term from isomer shifts (16) themselves. The Debye temperature of crystalline regions was obtained as 470 K, which is larger than that of grain boundary component, 370 K. The curve for the grain boundary component lies +0.05 mm/sec above the crystalline part. This difference in the isomer shifts was caused by the low density in grain boundaries.

4.3 Magnetization Data

Samples of Cr-Fe powders were sent to National Institute of Standards and Technology (17) and Japan (18) for magnetization curve measurements. Magnetization can be used to explain the origin of the hyperfine fields and to reveal the superparamagnetism (§ 4.4).

To confirm that the broadening of the Mössbauer peaks in Cr-Fe originates from changes in hyperfine magnetic fields in the material, we performed several experiments. No hysteresis appears in the magnetization curve of Cr-Fe as-filed powders (Figure 4.16) (18). However, hysteresis loops were found for powders milled for 48 and 96 hrs. The saturation magnetization, I_S, also increases with ball milling time. It is therefore expected that the line broadening of the Mössbauer spectrum after ball milling originates from ferromagnetism, which is consistent with the experimental results from vibrating sample magnetometry and Mössbauer

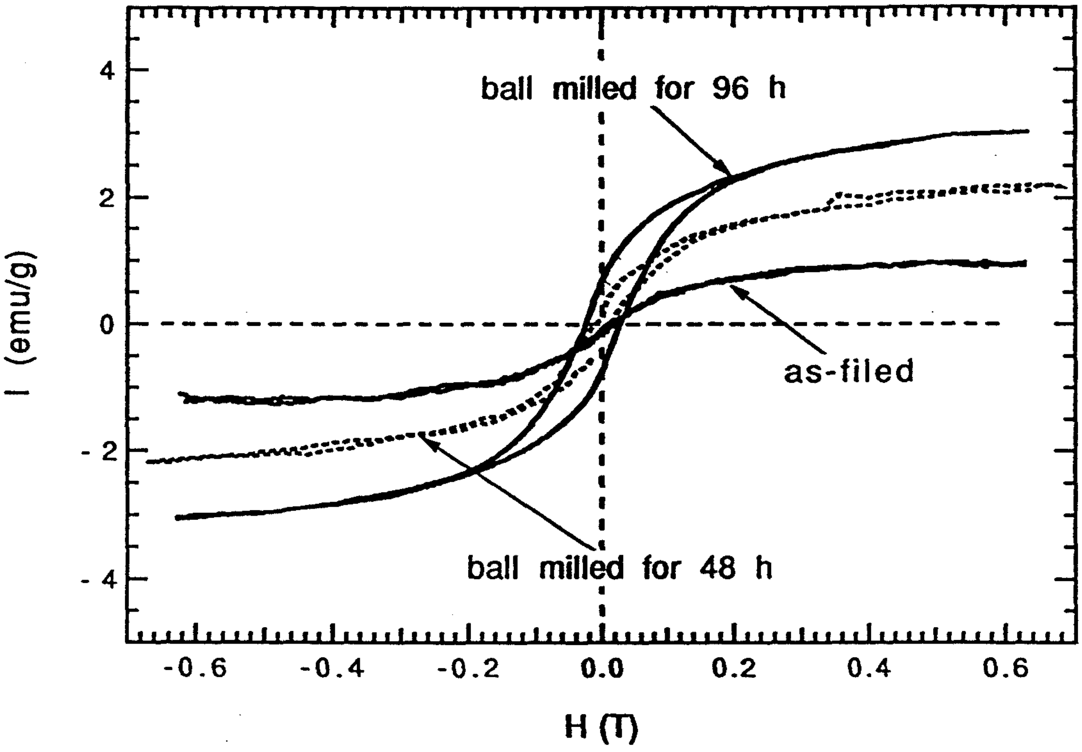

Figure 4.16. Room temperature magnetization curve from Cr-Fe sample before and after ball milling.

spectroscopy under external applied magnetic field. The average magnetic moment per Fe atom, μ_{av}, was measured as 0.046 μ_B and 0.54 μ_B for the 48 and 96 hr ball milling samples respectively (18). The average magnetic moment is equal to the sum of weighted average magnetic moments of Fe atoms in crystalline and grain boundary regions, which is:

$$\mu_{av} = f_{gb}\,\mu_{gb} + (1 - f_{gb})\,\mu_{xtl}, \qquad \text{(Eq. 4.2)}$$

where

μ_{gb} = magnetic moment of Fe atoms in grain boundary regions
μ_{xtl} = magnetic moment of Fe atoms in crystalline regions
f_{gb} = grain boundary volume fraction.

It was assumed that μ_{gb} and μ_{xtl} are independent of ball milling time between 48 and 96 hrs. The grain boundary volume fraction, f_{gb}, can be obtained from the high field component of the HMF distributions. μ_{gb} and μ_{xtl} are determined to be 0.03 and 0.06 μ_B per Fe atom respectively by solving equation 4.2. The estimated values are consistent with the HMF distributions obtained by the method of Le Caër and Dubois from the Mössbauer spectra: the average HMF value of grain boundary component is about as twice that of the crystalline component.

4.4 Superparamagnetism

From chapter 2, the probability that the magnetization vector changes its direction by thermal fluctuations is proportional to exp $\left(-\frac{2Kv}{kT}\right)$ (19),

where

K = anisotropy energy of the material, the energy required to go from one easy direction to another

v = particle volume

k = Boltzmann constant

T = temperature.

Since the grain size, and hence the magnetic domain size of nanophase materials is quite small, usually around 10 nm, it is expected that superparamagnetic behavior will often be observed for nanophase materials.

Mössbauer spectra of Cr-Fe powder ball-milled for 96 hrs were obtained between room temperature and liquid helium temperature. There were two components in the HMF distributions at room temperature (§ 4.1). However, a new high field distribution appeared between 30 and 90 kG as the temperature approached the liquid helium range (Figure 4.17). The transition temperature (Morin temperature) is around 10 K.

The magnetization curves were measured between room temperature down to 10 K (17). Coercive force is defined as the reverse field necessary to bring the material back to zero induction. Upon decreasing the temperature to 50 K, the coercive force decreased from 235 Oe to 204 Oe continuously while it increased dramatically to 227 Oe at 10 K (details are shown in Appendix B). It appears that part of the material is superparamagnetic. The large coercive force at 10 K is a reflection of going below the transition temperature of

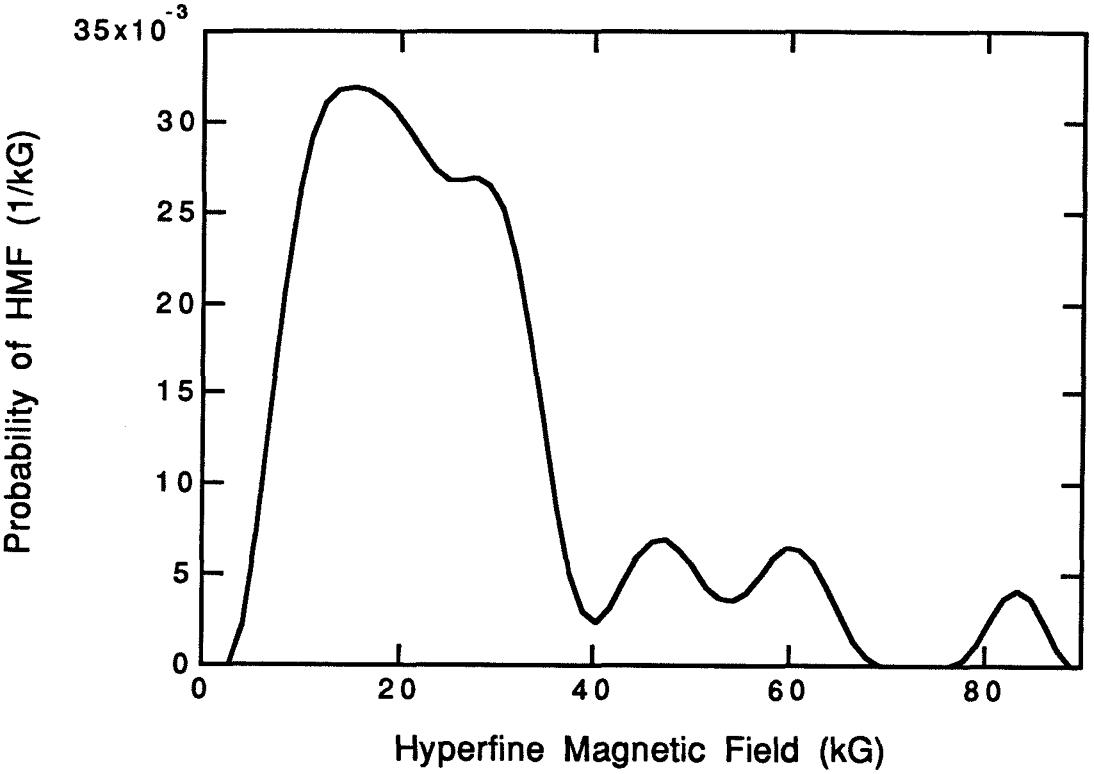

Figure 4.17. HMF distributions of Cr-Fe sample milled for 96 hours at liquid helium temperature.

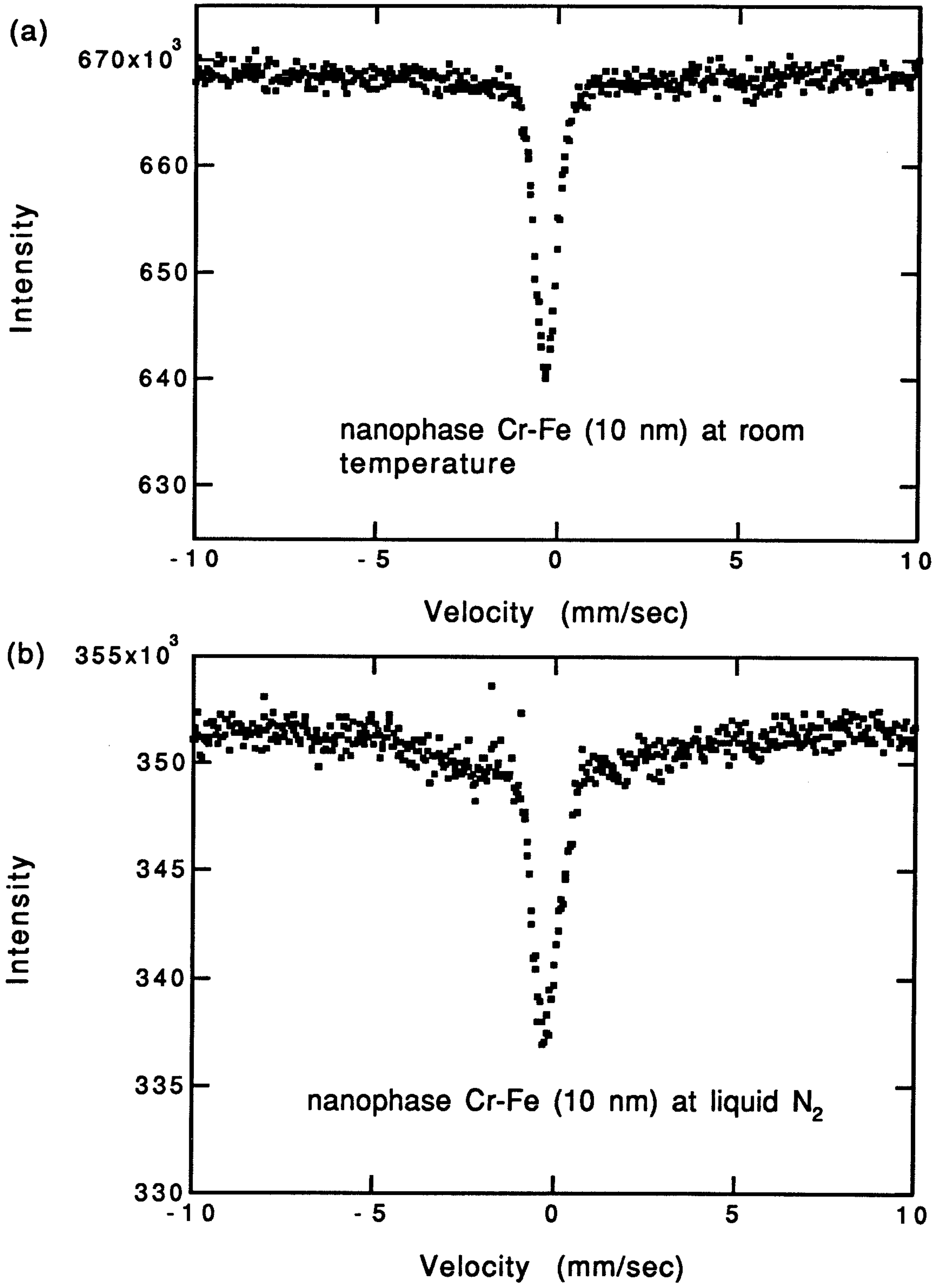

Figure 4.18. The Mössbauer spectra of nanophase Cr-Fe with 10 nm (a) at room temperature. (b) at 77 K.

superparamagnetism. This behavior is consistent with the results from Mössbauer spectrometry.

In order to study this phenomenon in more detail, the sample was annealed to induce grain growth from 3 nm to 10 nm and into the micron range. The Mössbauer spectra of nanophase Cr-Fe with 10 nm grain size are presented in Figure 4.18. The spectrum at room temperature was paramagnetic, however, there was ferromagnetic component at 77 K. After the sample was annealed to become polycrystalline, the spectrum was ferromagnetic even at room temperature as shown in Figure 4.19. Qualitatively, it is easy to observe the magnetic transition at higher temperature. Since the anisotropy energy K is also a function of grain size and other factors (20), the transition temperature may not be a function with one variable, grain size.

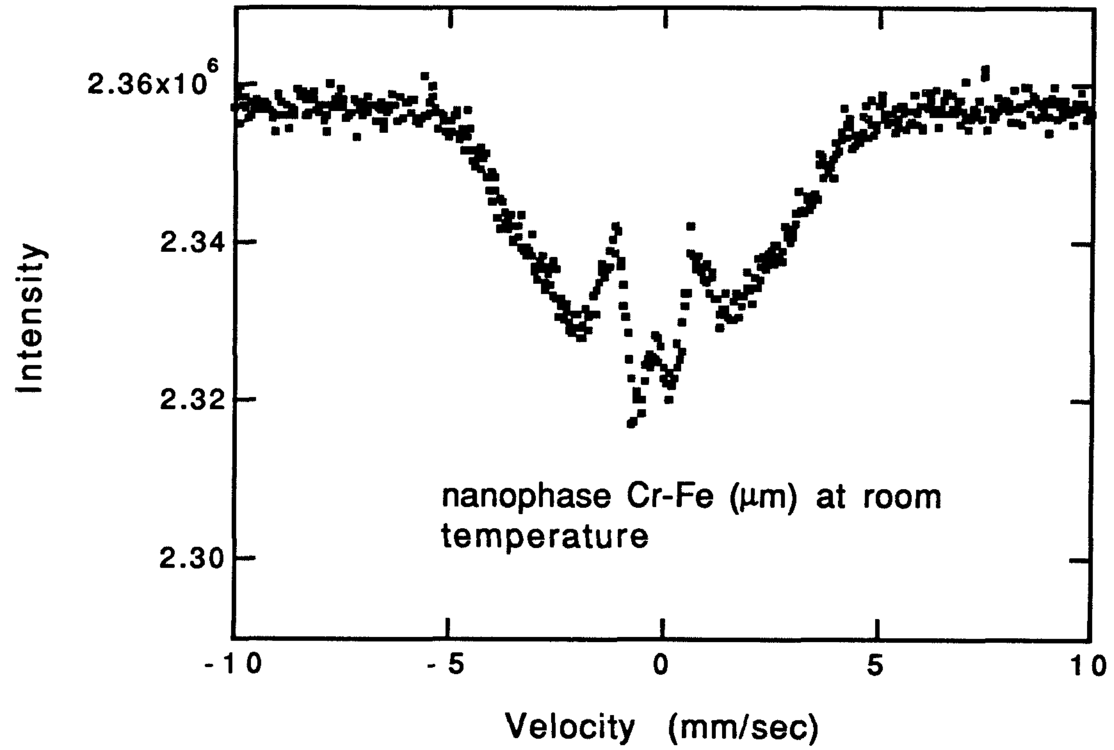

Figure 4.19. The Mössbauer spectrum of polycrystal Cr-Fe at room temperature.

References for Chapter 4

1. Varret F., Gerard A. and Imbert P, Phys. Stat. Solid B, **43**, 723 (1971)

2. Window B., J. Phys. E: Sci. Instrum., **4**, 401 (1971).

3. Hesse J. and Rübartsch A., J. Phys. E: Sci. Instrum., **7**, 526 (1974).

4. Vincze I., Solid St. Commun., **25**, 689 (1978).

5. G Le Caer and J M Dubois, J. Phys. E: Sci. Instrum., **12**, 1083 (1979).

6. S. S. Hanna, J. Heberle, G. J. Perlow, R. S. Preston, and D. H. Vincent, Phys. Rev. Lett., **4**, 513 (1960).

7. Matthias Brendel, Ph.D. Thesis (1990), Fachbereich Physik-Technologie der Universität-GH-Duisburg.

8. A. R. Miedema, F. R. de Boer and R. Boom, CALPHAD, **1**, 341 (1977).
9. M. N. Varma and R. W. Hoffman, J. Appl. Phys. **42**, 1727 (1971).

10. G. K. Wertheim, V. Jaccarino, J. H. Wernick, and D. N. E. Buchanan, Phys. Rev. Lett., **12**, 24 (1964).

11. I. Vincze and I. A. Cambell, J. Phys. F: Metal Phys., **3**, 647 (1973).

12. U. Herr, J. Jing, R. Birringer, U. Gonser, and H. Gleiter, Appl. Phys. Lett. **50**, 472 (1987).

13. Editor Leopold May, An Introduction to Mössbauer Spectroscopy (Plenum Press, New York-London, 1971), chapter 2 by Jon J. Spijkerman.

14. Editor U. Gonser, Mössbauer Spectroscopy (Springer-Verlag, New York, Heidelberg Berlin, 1975), chapter 1 by U. Gonser.

15. Private communication with Dr. H. Kuwano.

16. Editor Shenoy, G. K. and Wagner, F. E., Mössbauer Isomer Shifts (North Holland, 1977), chapter 3 by Shenoy, G. K., Wagner, F. E. and Kalvius, G. M..

17. Private communication with Dr. Robert D. Shull.

18. H. Kuwano, H. Ouyang and B. Fultz, Materials Science Forum, **88-90**, 561 (1992).

19. Walter Kündig, Hans Bömmel, Phys. Rev. **142**, 327 (1966).

20. G. Herzer, IEEE Trans. Magn., **25**, 3327 (1989).

Chapter 5 Grain Boundaries of Nanophase Materials

In this chapter some results from computer simulations are discussed. The method and physical origin of Monte Carlo simulations are described in § 5.1. The procedures to obtain the grain boundary width from X-ray and simulation results are discussed in § 5.2. The summary and future perspective are discussed in § 5.3.

5.1 Monte Carlo Simulations

Monte Carlo simulations were used to create microstructures having crystallite size distributions with qualitative similarities to those of the ball-milled powders. We used these simulated microstructures to simultaneously interpret the results from our Mössbauer spectrometer and x-ray diffractometer experiments. The simulations were inspired by the Johnson-Mehl model of homogeneous nucleation and growth of crystals from a melt. A simple cubic lattice with 1×10^6 elemental cubes was created, and each cube was initially assigned the number 0. Individual elements within this lattice were chosen as nuclei, and assigned numbers other than zero. The distribution of nuclei could be random or non-random, dense or not dense, depending on the desired microstructure, but a random distribution provided a crystalline column length distribution in modest agreement with the exponential distribution determined from the Lorentzian x-ray lineshapes. The algorithm used to grow a microstructure involved a series of steps where the first neighbors of a cube with a non-zero number were assigned the same number as the cube, provided they were neighbors with the number 0. This process continued until there were no remaining cubes with the number 0, and the grains were identified as regions of continuous cubes having the same assigned number (Figure 5.1). This crystal microstructure is not real, but it serves as a "bridge" for data interpretations.

The crystallite column length distributions, used for comparison with x-ray diffraction data, were obtained by measuring the lengths between grain boundary intercepts of straight lines drawn through the lattice. A typical distribution of these column lengths is presented in Figure 5.2. This column length distribution is in reasonable agreement with that from analyses of TEM images such as presented in Figure 3.7, and with the exponential column length distribution deduced from the Lorentzian lineshapes of the x-ray diffraction peaks.

5.2 Grain Boundary Widths

While determining the column length distribution from the Monte Carlo microstructures was straightforward, counting the grain boundary atoms required an unconventional algorithm (1-2). Several versions of this algorithm were used, denoted as "1nn", "3nn", and "9nn" (Appendix C). For the "1nn" version, cubes at and near grain boundaries were identified and counted if they had at least one first nearest neighbor in a different crystallite. Grain boundary volume fractions denoted "2nn" were obtained by counting all cubes that had either first- or second-nearest-neighbors in a different crystallite. In this way we obtained data for the fraction of grain boundary

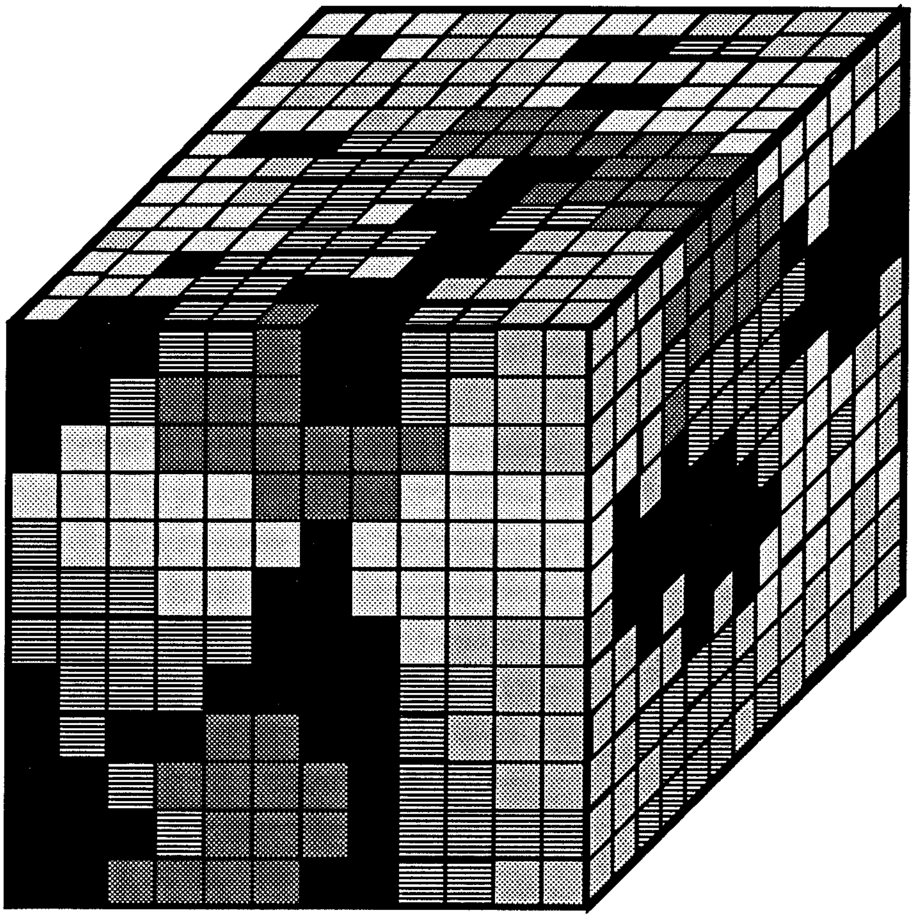

Figure 5.1. Schematic diagram of a cubic lattice generated by Monte Carlo simulation.

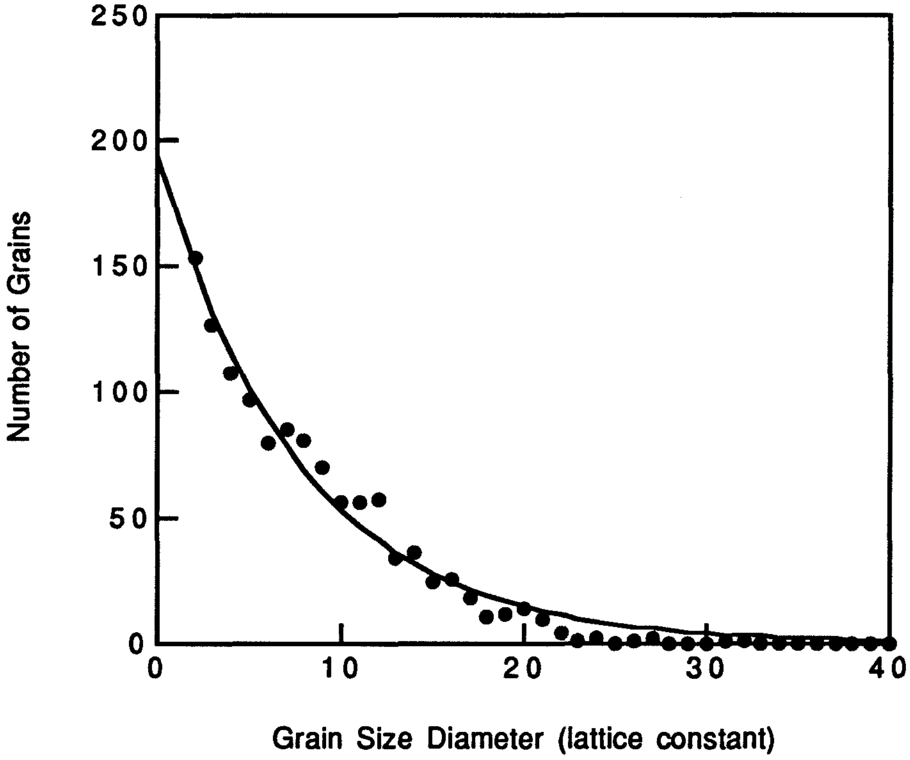

Figure 5.2. Column length distribution from Monte Carlo simulation starting with 500 nuclei.

cubes versus crystallite size for different versions of the algorithm (Figure 5.3), and hence different grain boundary widths. Data from this algorithm are appropriate for comparison with the Mössbauer effect data since both methods (Mössbauer and Monte Carlo) counted atoms at the edges of crystallites.

In Chapter 4, the magnetic width of the grain boundary from Mössbauer data was determined by estimating the grain boundary fraction as a function of ^{57}Fe atoms of crystallite size (Figure 4.13). Here to obtain a conventional grain boundary width, first, an edge length equal to one lattice constant was assigned to the individual cubic elements of the Monte Carlo lattice. This defined an x-axis for comparison with the data of Figure 4.13. Suppose the best fit occurred for the "jnn" version of the algorithm. The length of the jth nearest-neighbor distance is too large for a structural width of the grain boundary, since it also includes atoms at the edges of crystallites as part of the grain boundary fraction. To disallow these edge atoms, the structural width of the grain boundary was taken as the jth nearest-neighbor distance minus a thickness of two unit cell edge lengths.

The data of Figure 4.5, 4.11, 4.12 and 4.13 are included in Figures 5.4 - 5.7, which include results from two versions of the Monte Carlo algorithm. We see that the "9nn" model provides the most accurate grain boundary fraction for the bcc alloys, and the "3nn" works best for the fcc alloys. We convert this into a structural width of the boundary of about 1 nm for the bcc alloys Cr-Fe and Fe-Ti, and about 0.5 nm for the fcc alloys Ni-Fe and Fe-Mn. The grain boundary widths for the fcc alloys are in reasonable agreement with the results of HREM observations of grain boundary widths in fcc metals such as Al, Au, Pd, Pb, and Cu (3-6). Few HREM observations of grain boundaries in bcc metals have been reported (especially ferromagnetic α-Fe).

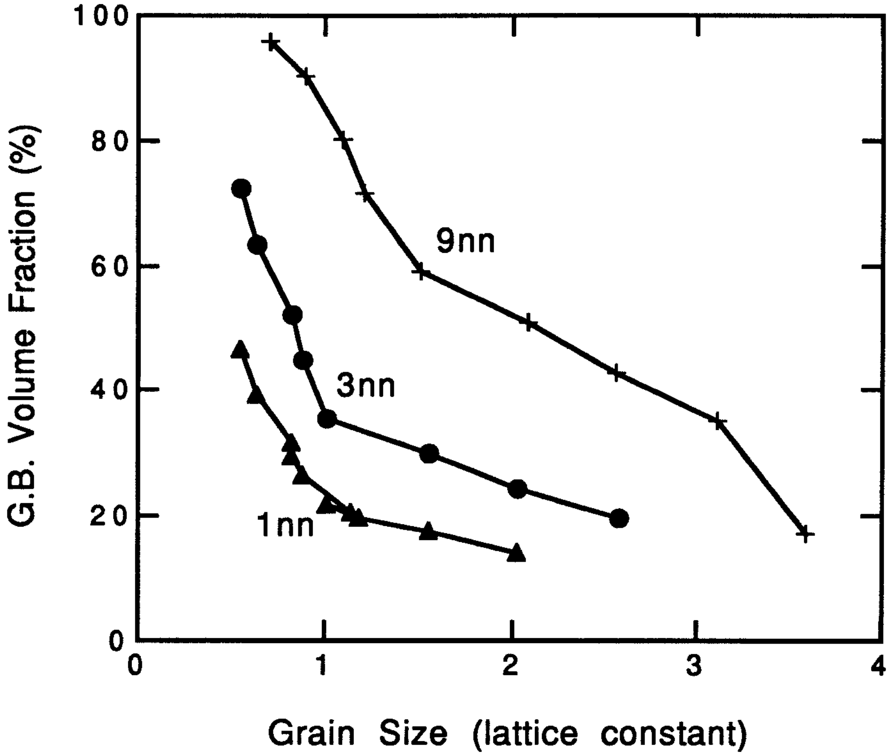

Figure 5.3. Volume fraction of atoms at grain boundaries versus crystallite size. The curves are labelled for the model described in the text.

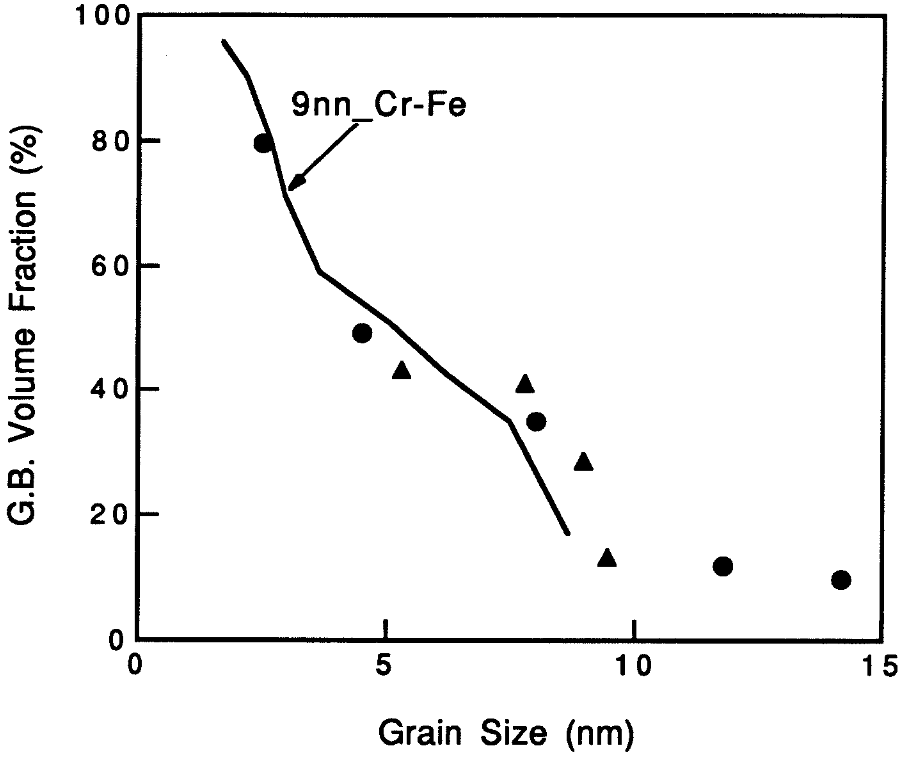

Figure 5.4. Volume fraction of atoms at grain boundaries versus crystallite size for Cr-Fe. The curve is labelled for the model described in the text. Data points from Figure 4.5.

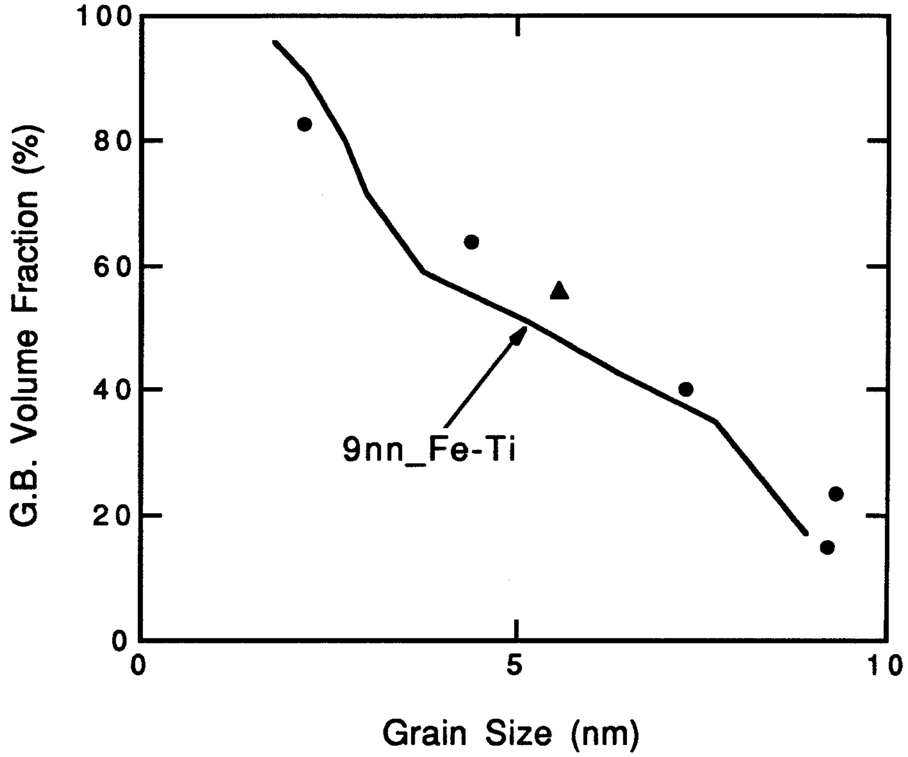

Figure 5.5. Volume fraction of atoms at grain boundaries versus crystallite size for Fe-Ti. The curve is labelled for the model described in the text. Data points from Figure 4.11.

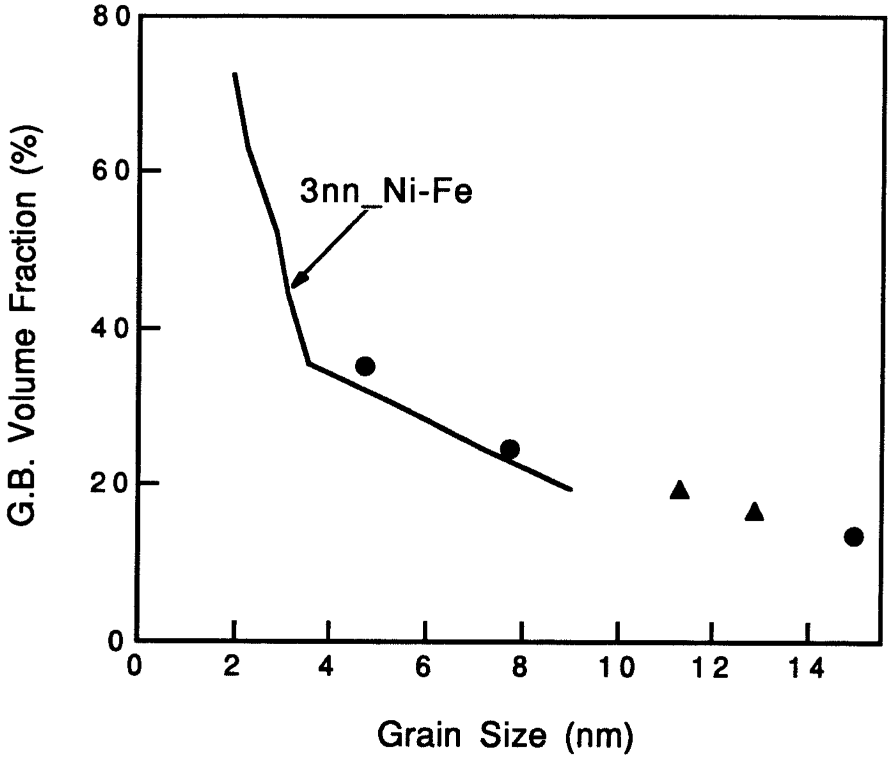

Figure 5.6. Volume fraction of atoms at grain boundaries versus crystallite size for Ni-Fe. The curve is labelled for the model described in the text. Data points from Figure 4.12.

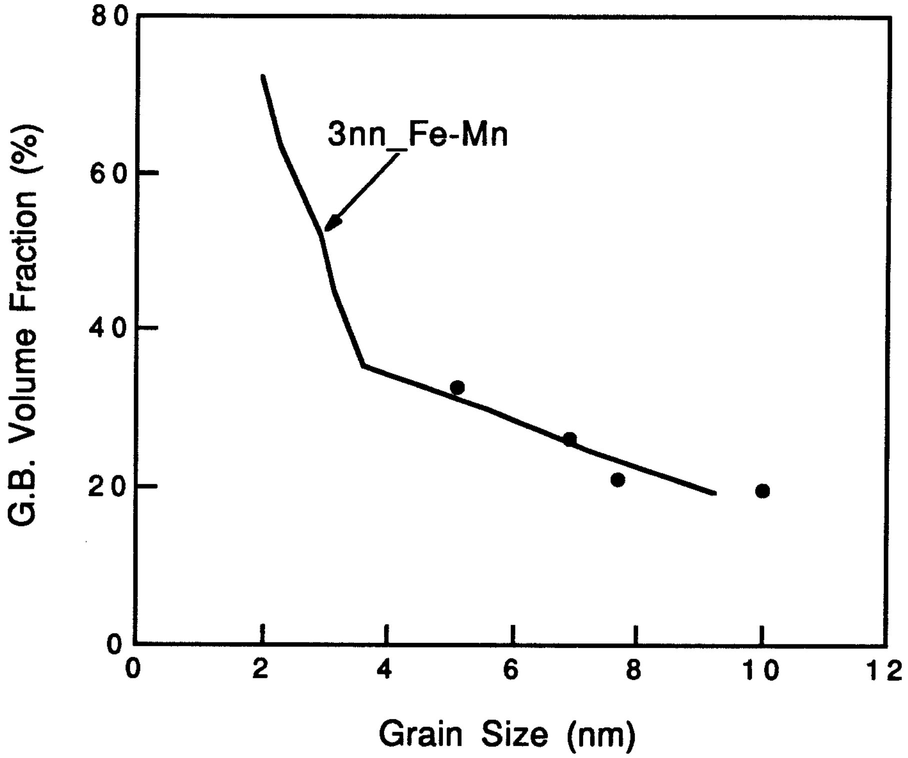

Figure 5.7. Volume fraction of atoms at grain boundaries versus crystallite size for Fe-Mn. The curve is labelled for the model described in the text. Data points from Figure 4.13.

Figures 5.4 - 5.7 strongly suggest that a difference exists between the grain boundaries of bcc and fcc metals. For grain sizes around 5 nm, where both the Mössbauer data and x-ray line broadening data are expected to be most reliable, the bcc alloys have about twice as many ^{57}Fe atoms at grain boundaries than do the fcc alloys. It seems unlikely that data processing errors of our experimental techniques can account for such a large difference. It could be argued that since the grain boundary is of low density, the assumption of uniform density in the Monte Carlo simulations may lead to a (small) underestimate of grain boundary width. On the other hand, an Fe enrichment of the boundary would lead to an overestimate. However, it seems unlikely that such problems with grain boundary density or chemical segregation could cause the factor of two difference in the bcc and fcc data of Figures 5.4 - 5.7, since we compared alloys of different compositions and chemical segregation tendencies, and we compared materials as-milled to materials with grain growth induced by annealing.

5.3 Summary and Perspective

By mechanical attrition in a high energy ball mill, bcc and fcc alloys with crystallite sizes in the range of 3-5 nm were synthesized. From Mössbauer spectra, we found that the ^{57}Fe hyperfine magnetic field (HMF) distribution is bimodal. By correlating the two components in the HMF distribution to measurements of crystallite size, we attribute them to ^{57}Fe atoms in regions of good crystal and to ^{57}Fe at grain boundaries. Since the two components in the HMF distribution were well-resolved, the atoms at and near grain boundaries can be distinguished from those in the crystallites.

By obtaining the grain boundary fraction from Monte Carlo simulations, we obtain grain boundary widths slightly greater than 1 nm for the bcc alloys of Cr-Fe and Fe-Ti, and widths of 0.5 nm for the fcc alloys of Fe-Mn and Ni-Fe.

The narrow grain boundary widths of the fcc alloys, which are consistent with high resolution TEM observation, leaves little volume available for having a highly disordered grain boundary region. In particular, the "gas like" disorder proposed by Gleiter and coworkers (7) seems impossible for grain boundaries of nanophase fcc alloys. On the other hand, the large grain boundary widths of nanophase bcc transition alloys may allow for a more disordered grain boundary structure.

It is not surprising to find a difference between the grain boundaries of fcc and bcc transition metal alloys. The packing density of the fcc structure is known to be larger than the bcc structure (8). Therefore, the bcc structure is more open than the fcc structure. By using interatomic central force potentials, it has been argued that the bcc transition metals have strong directional covalent bonds (9). The existence of directional covalent bonds has been suggested also by theoretical physicists in terms of the d band structure (10). It is reasonable that the microstructural gaps between crystallites in transition bcc alloys are not packed as densely as possible, but some angular accommodation of atoms in the grain boundaries may be necessary. Therefore, atoms in the microstructural gaps can not be simply attached to a bcc crystallite until the crystallites impinge. This difference could lead to a greater width of bcc grain boundaries, or strong relaxations at the edges of bcc crystallites.

The temperature dependence of the bimodal distribution in Cr-Fe also allowed the study of the phonon spectra of crystallites and grain boudaries separately. The Debye temperature is a physical parameter of the vibrational spectrum of the solid. From the temperature dependence of individual thermal shifts (actually the second order Doppler shift) associated with grain boundaries and crystalline regions (Chapter 4), the Debye temperature of crystalline regions in Cr-Fe nanophase can be obtained as 470 K, which is larger than that of grain boundary component, 370 K. The Debye temperature 397 K of nanophase Cr-Fe was obtained from the recoil-free fraction of Mössbauer effect. The recoil of independently moveable nanocrystals cannot account for the differences in Debye temperature (or recoil-free fraction). In our case, all the nanocrystallites are packed closely as we see by examining the sample with TEM. Therefore, the change of Debye temperature must be caused by changes in the phonon spectrum. The change in the Debye temperatures reflects the structural difference between grain boundaries and crystalline regions.

It is known that the bulk physical properties of materials can change substantially when their size becomes reduced to very small dimensions, either in the form of thin films or in the form of small nanocrystallites (5, 11-14). In metallic nanocrystals with grain sizes in the range of several nanometers, a large fraction of the atoms is located in grain boundary regions, and thus, they possess novel properties over those of conventional polycrystalline or glassy materials (Chapter 1). The technological applications of nanophase materials depend on the development of production procedures. The properties of nanophase materials can be varied by different preparation methods. For example, the grain size distribution is log-normal by the gas condensation method, and is approximately exponential by the method of the mechanical attrition. Therefore, the study of properties of nanophase materials by various methods could be important for applications of nanophase materials.

References for Chapter 5

1. H. Kuwano, H. Ouyang and B. Fultz, Nanostructured Materials, **1**, 143 (1992).

2. H. Ouyang, B. Fultz, and H. Kuwano, "Grain Boundary Widths of Four Fcc and Bcc Nanophase Alloys Prepared By Mechanical Attrition," submitted to TMS (1992).

3. G. J. Thomas, R. W. Siegel, and J. A. Eastman, Scripta Metall. Mater., **24**, 201 (1990).

4. W. Wunderlich, Y. Ishida, and R. Maurer, Scripta Metall. Mater., **24**, 403 (1990).

5. R. W. Siegel, MRS Bulletin, **15**, 60 and cover (1990).

6. S. K. Ganapathi and D. A. Rigney, Scripta Metall. Mater., **24**, 1675 (1990).

7. H. Gleiter, Prog. Mater. Sci., **33**, 223 (1990).

8. Charles Kittel, Introduction to Solid State Physics, John Wiley & Sons, INC., New York (1981), p. 16.

9. E. S. Machlin and J. Shao, J. Phys. Chem. Solids, **44**, 435 (1983).

10. Friedel J., Physics of Metals (Edited by J. M. Ziman), Cambridge University Press, London (1969).

11. M. N. Varma and R. W. Hoffman, J. Appl. Phys., **42**, 1727 (1971).

12. R. W. Siegel, S. Ramasamy, H. Hahn, Li Zongquan, and Lu Ting, J. Mater. Res., **3**, 1367 (1988).

13. R. S. Averbach, H. Hahn, H. J. Höfler, and J. C. Logas, Appl. Phys. Lett., **57**, 1745 (1990).

14. C. Suryanarayana and F. H. Froes, Metall. Trans. A, **23A**, 1071 (1992).

Appendix A Method of Warren and Averbach

The method of Warren and Averbach provides column length information and strain information as functions of the different coefficients of the Fourier transform of x-ray diffraction peaks. The method uses the first two orders of parallel crystallographic planes. First of all, it is necessary to get the Fourier coefficients of standard sample, polycrystal silicon in our case, to obtain an instrument function used in data correction. The Rachinger correction (1) is not necessary for a sample with very small grain size. Results from the INEL CPS 120 x-ray diffractometer, however, need to be corrected for the asymmetrical relation of incident and diffracted angles with respect to the sample surface. After the Fourier coefficients were obtained, the Stoke's method (1) was performed to correct the instrument function. The Fourier coefficients then were mathematically manipulated to find out the average grain size and strain (2). The program was written in Mathcad 3.1 Windows™ version.

The present version of the program only allows interactive processing of one diffraction peak at a time. It is necessary to make the two theta range symmetric about the center of the peak. After the one peak file is input as "fin", results of Fourier coefficients will be given in the file "f3". For more details, please refer to the documentation of the program and the manual of Mathcad 3.1. Fourier coefficients of the Si standard sample are presented in Figure A.1.

Spline Interpolation & Frequency Analysis Document

This program will spline interpolate to make the total number of data points to be transformed equal to the first power of two that is greater than the number of input data points. i.e., if you have 379 points in the data file, the program will interpolate extra 133 points to bring the total to 512. This allows Mathcad to use a much faster Cooley-Tookey type butterfly FFT in other documents that deconvolute instrument functions, calculate grain size and strain, etc. The spline interpolation assumes that the slope at both ends of the peak goes to zero. Written by David S. Lee, 4/92. Modified by Hao Ouyang for INEL diffractometer.

$\mathrm{Origin} \equiv 1$

fin f3

$\mathrm{xrstrip} := \mathrm{READPRN}(\mathrm{fin})$

$\mathrm{xrangle} := \mathrm{xrstrip}^{\langle 1 \rangle}$ $\mathrm{xrint} := \mathrm{xrstrip}^{\langle 2 \rangle}$

Incident beam angle of Inel

$\mathrm{incangle} := 15$

Remove the Lorentz-Polarization factor and absorption effect for Inel from the spectrum.

$$\mathrm{xrcount} := \overrightarrow{\frac{\mathrm{xrint}}{\dfrac{\sin\left[(\mathrm{xrangle}-\mathrm{incangle})\cdot\frac{\pi}{180}\right]\cdot\left[1+\cos\left(\mathrm{xrangle}\cdot\frac{\pi}{180}\right)^2\right]}{\sin\left(\mathrm{xrangle}\cdot\frac{\pi}{360}\right)^2\cdot\cos\left(\mathrm{xrangle}\cdot\frac{\pi}{360}\right)\cdot\left[\sin\left(\mathrm{incangle}\cdot\frac{\pi}{180}\right)+\sin\left[(\mathrm{xrangle}-\mathrm{incangle})\cdot\frac{\pi}{180}\right]\right]}}}$$

Figure out the limits for the grapg...

$\mathrm{top} := \max(\mathrm{xrcount})$ $\mathrm{graftop} := 1.05\cdot\mathrm{top}$

$\mathrm{bottom} := \mathrm{if}(\min(\mathrm{xrcount})<0, 1.05\cdot\min(\mathrm{xrcount}), 0)$

Figure out the number of points in the splined data vectors.

$\text{npts} := \text{rows}(\text{xrstrip})$

$$\text{log2npts} := \frac{\ln(\text{npts})}{\ln(2)}$$

$\text{power} := \text{if}\ (\text{mod}(\text{log2npts}, 1)=0, (\text{log2npts}+ 1), \text{ceil}(\text{log2npts}))$

$\text{Qpts} := 2^{\text{power}}$

Below is a declaration/initialization of the data vectors and transformation arrays. The data vectors are then filled with the spline interpolation. Also declared are two temporary arrays used for the spline interpolation, "temp" and "tempang."

$i := 1 .. \text{Qpts}$

$Q_{i,2} := 0$ $\quad$ $\text{xr2count}_i := 0$ $\quad$ $\text{xr2angle}_i := 0$

$\text{temp}_i := 0$ $\quad$ $\text{tempang}_i := 0$

The vector "vs" is a vector containing the second derivative information for the cubic spline interpolation. It is used by the function "cspline" for later interpolation.

$\text{vs} := \text{cspline}(\text{xrangle}, \text{xrcount})$

Calculate the step size for the splined data.

$$\text{step} := \frac{(\text{xrangle}_{\text{npts}} - \text{xrangle}_1)}{\text{Qpts}}$$

Begin the calculations- The total number of points is the first power of two greater than the original number of data points-i.e.,Qpts.

$j := 1..\text{Qpts}$

$\text{xr2angle}_j := \text{xrangle}_1 + \text{step} \cdot (j-1)$

$xr2count := \overrightarrow{\mathrm{interp}(vs,xrangle,xrcount,xr2angle)}$

Create an output array of the appropriate size

$j := 1..Qpts$

$xr2spline_{j,2} := xr2count_j$

$xr2spline_{j,1} := xr2angle_j$

$i := 1..npts$

$xr2count_j$

$xrcount_i$

$xr2angle_j \ , xrangle_i$

Now that we have calculated a splined interpolation for the stripped data, we have "Qpts" data points, where "Qpts" is a power of two. This was done to allow the use of the fft( ) and ifft( ) functions in MCAD, as opposed to the cfft( ) and icfft( ) functions which do not require a power of two but are much slower.

Calculation of the Frequency Spectrum of an Instrument Function and a Diffraction Peak.

This part of the document takes the Fourier Transform of an x-ray diffraction spectrum and calculates its frequency dependence. In particular, this allows the calculation of the coefficients of the Fourier series for the instrument function, which in turn allows it to be deconvolved from the experimentally measured profile, thus leaving only the line profile of the material.

$\lambda := 1.78892$

xrstrip :=xr2spline

xrangle :=xrstrip$^{<1>}$ xrcount :=xrstrip$^{<2>}$

Define the scattering vector, q.

$$q := \left[2 \cdot \frac{\overrightarrow{\left(\sin\left(\frac{xr2angle}{2} \cdot \frac{\pi}{180}\right)\right)}}{\lambda}\right]$$

Take the Fast Fourier Transform of the data.

T :=fft(xcount)

i :=1..rows(T)

The frequency is defined as the inverse of the q-vector step size. Note that this is an approximation that is valid only if sin(deltatheta) ~ deltatheta, which is fine for small deltatheta,i.e., as long as your peaks are not too wide or the step size is very small.

$f_i := \frac{i}{q_i}$

$Tmag_i := \frac{T_i \cdot \exp[\pi \cdot (i-1) \cdot \sqrt{-1} \cdot \frac{Qpts-1}{Qpts}]}{T_1}$

$Qpts =$

$\max(f) =$

$f_1 =$

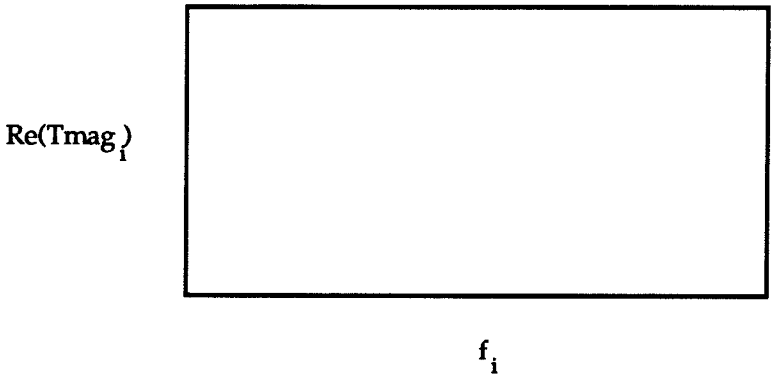

Write/Append the coefficients of the transformed spectrum to a file.

$xrFT_{i,1} := f_i$

$xrFT_{i,2} := (Tmag_i)$

WRITEPRN(f2) :=xrFT

$FTxr_1 := xrFT_{1,1}$

$j := 2..10$

$FTxr_j := xrFT_{j-1,2}$

APPENDPRN(f3) :=$FTxr^T$

$FTxr^T =$

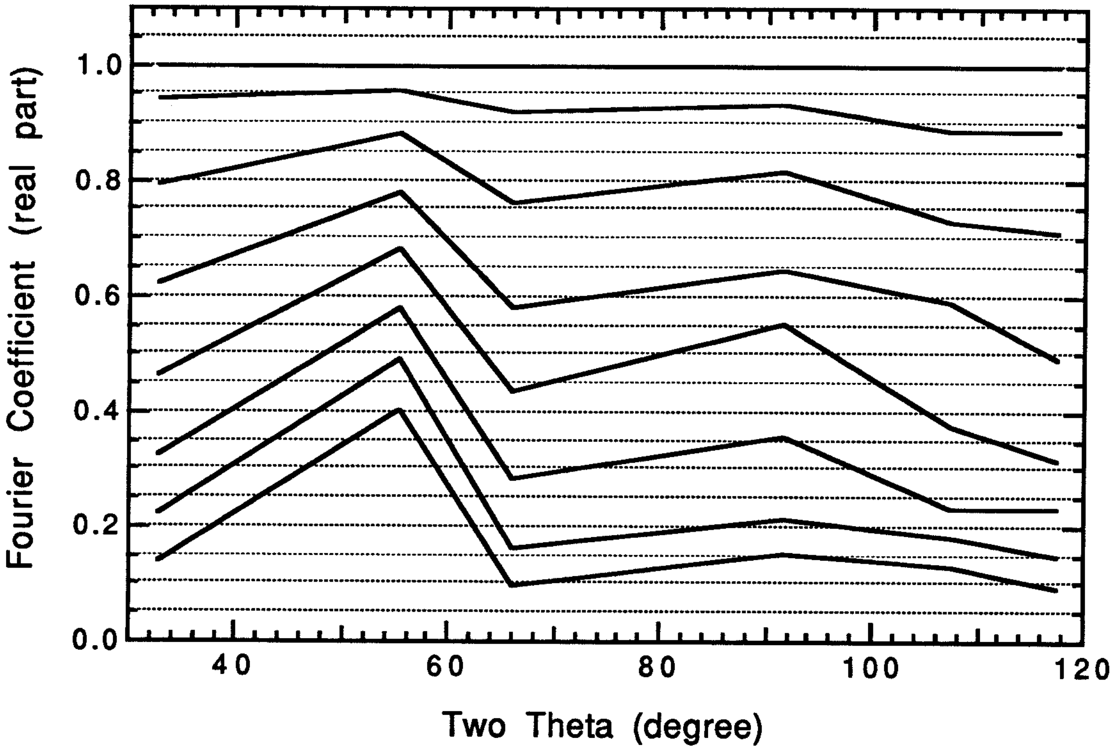

Figure A.1. Fourier coefficients of the Si standard powder sample.

References

1. H. P. Klug and L. E. Alexander, X-Ray Diffraction Procedures (John Wiley, New York, 1974).

2. B. E. Warren, X-Ray Diffraction (Dover, New York, 1990), p. 257-274.

Appendix B Magnetization Data

Enclosed are the magnetization data for the nanophase Cr-18.5 % Fe sample.

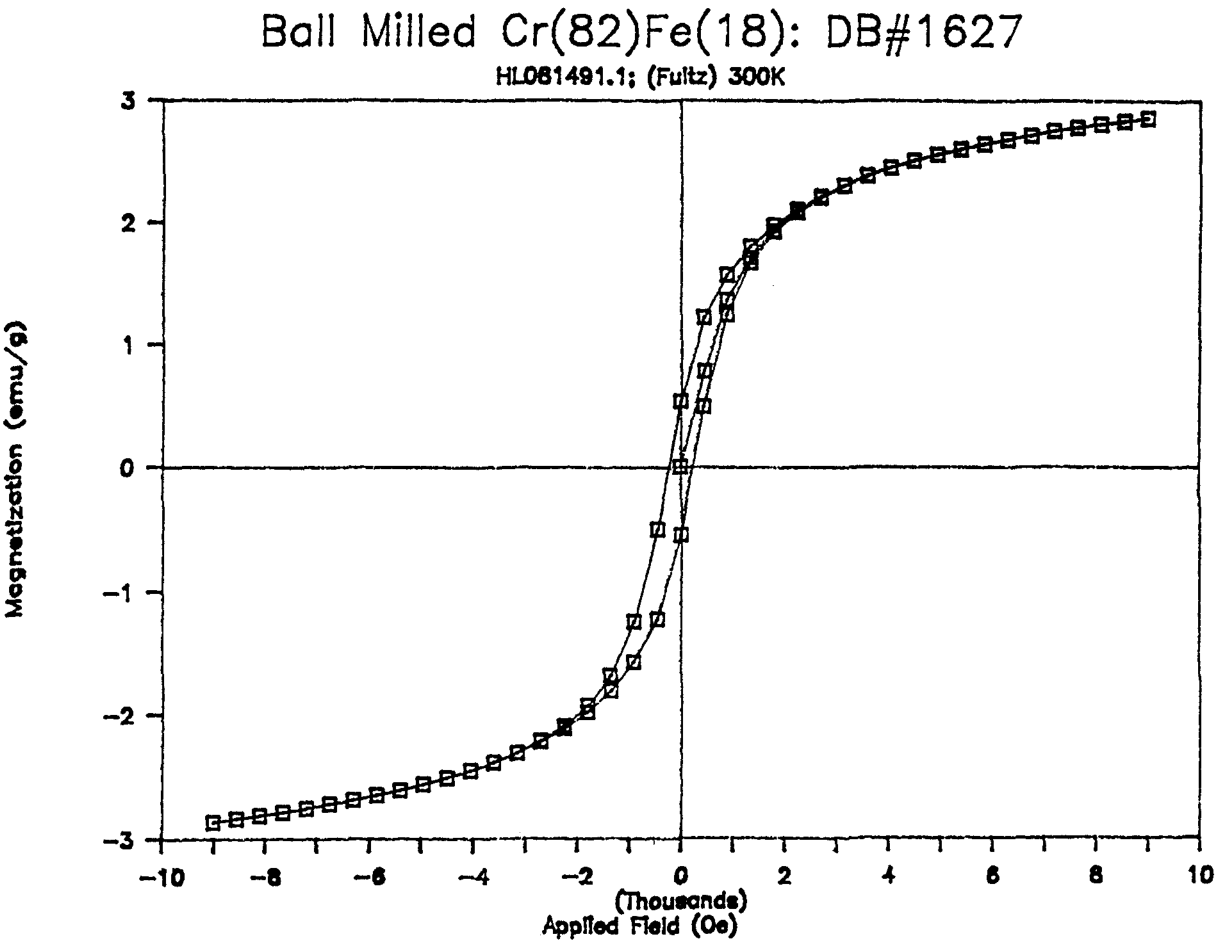

Figure B.1. Magnetization curve of nanophase Cr-Fe at 300 K.

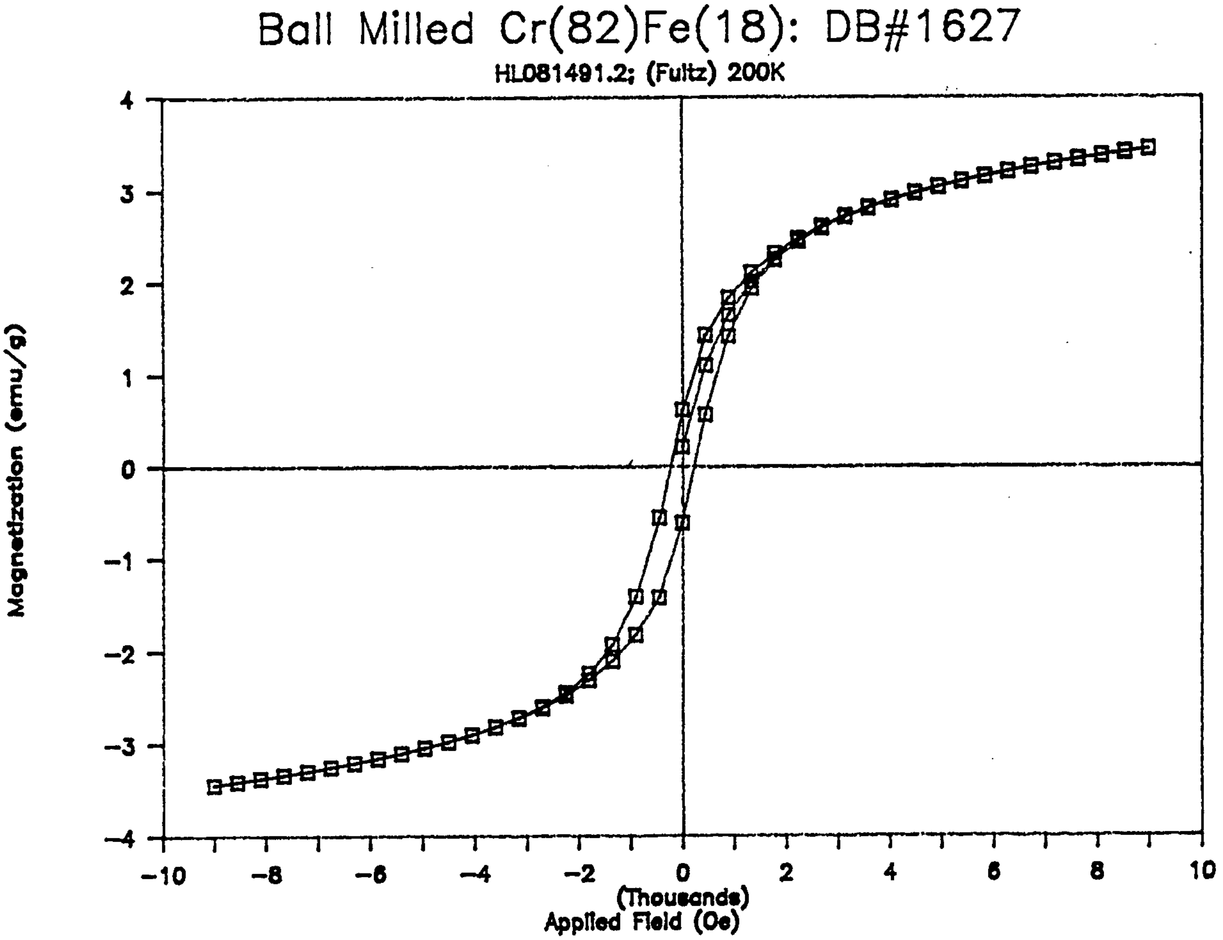

Figure B.2. Magnetization curve of nanophase Cr-Fe at 200 K.

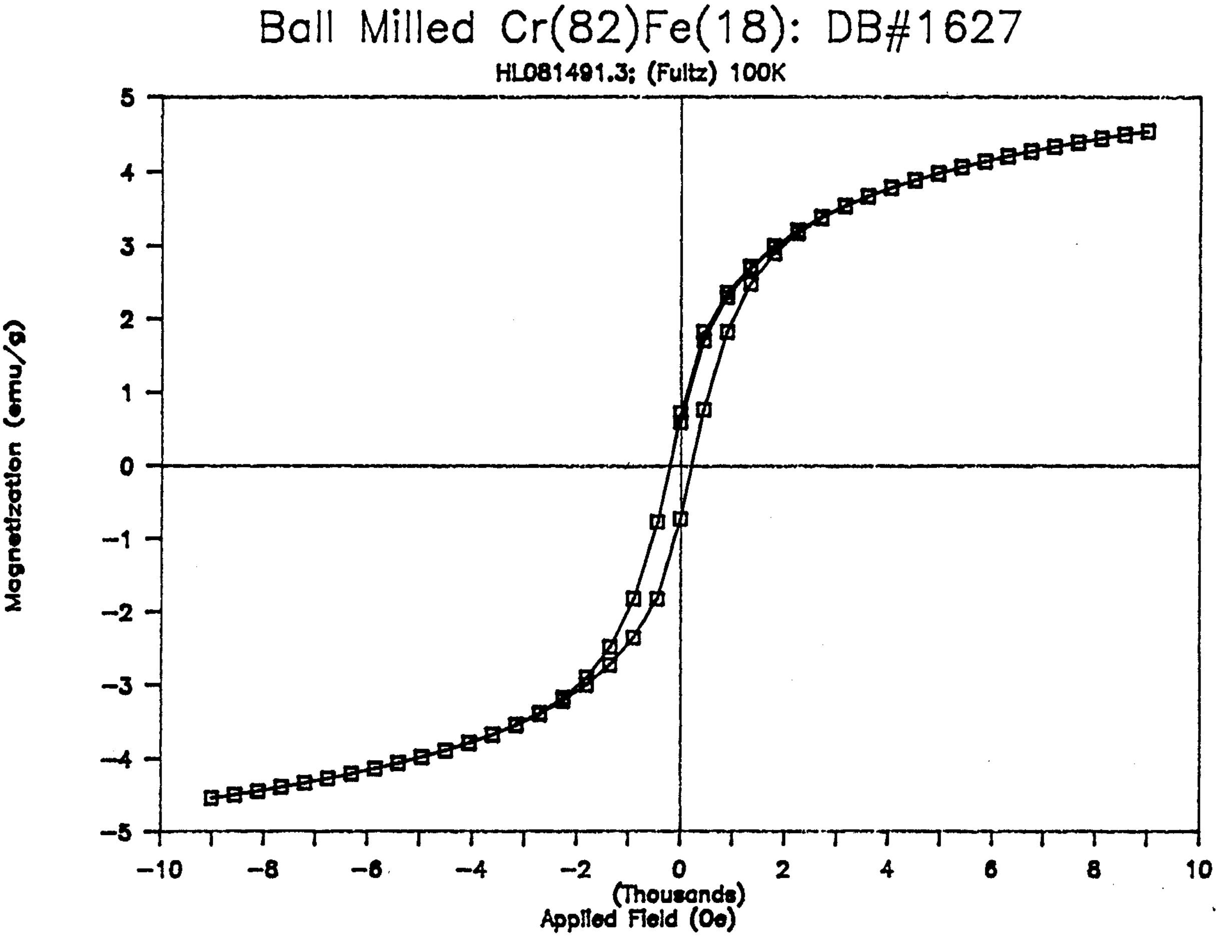

Figure B.3. Magnetization curve of nanophase Cr-Fe at 100 K.

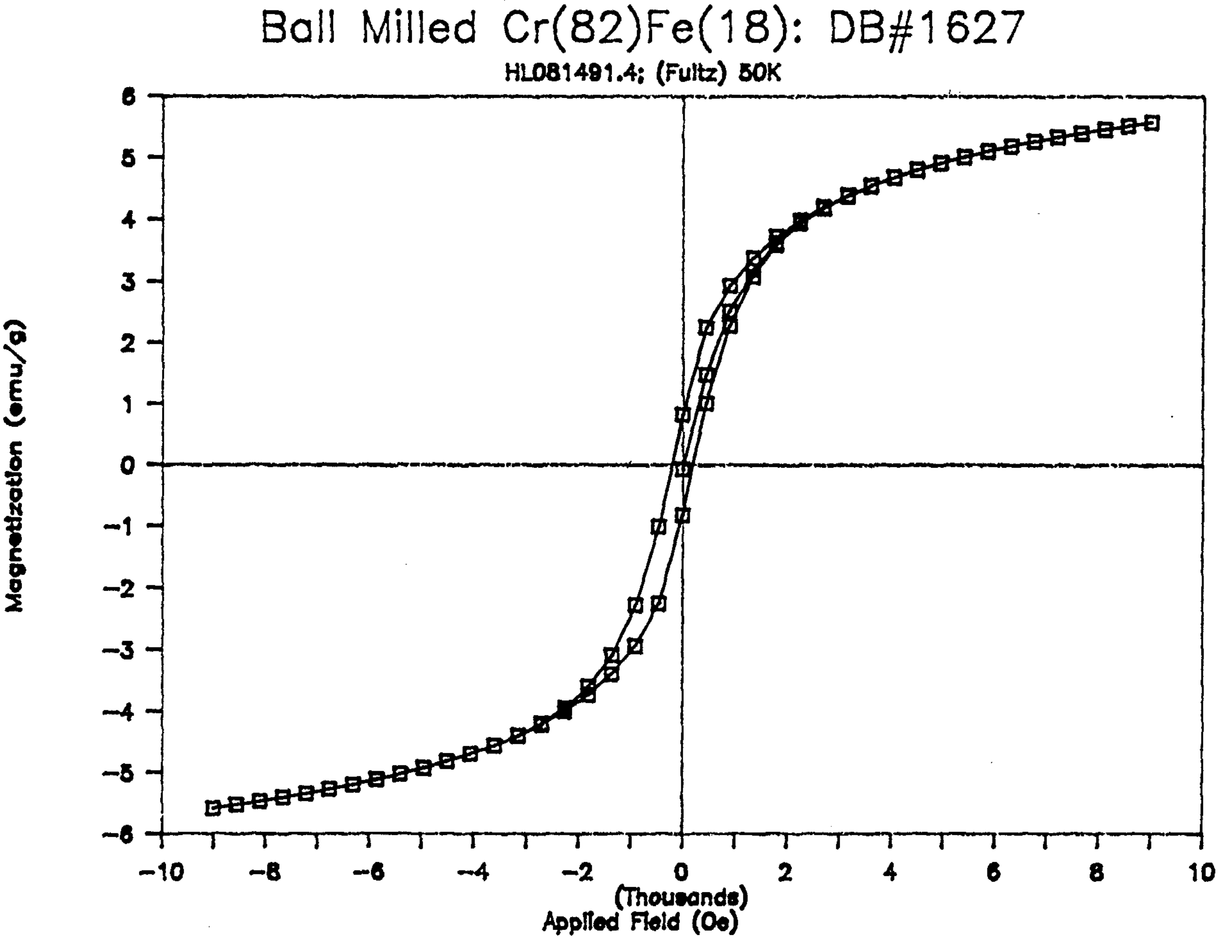

Figure B.4. Magnetization curve of nanophase Cr-Fe at 50 K.

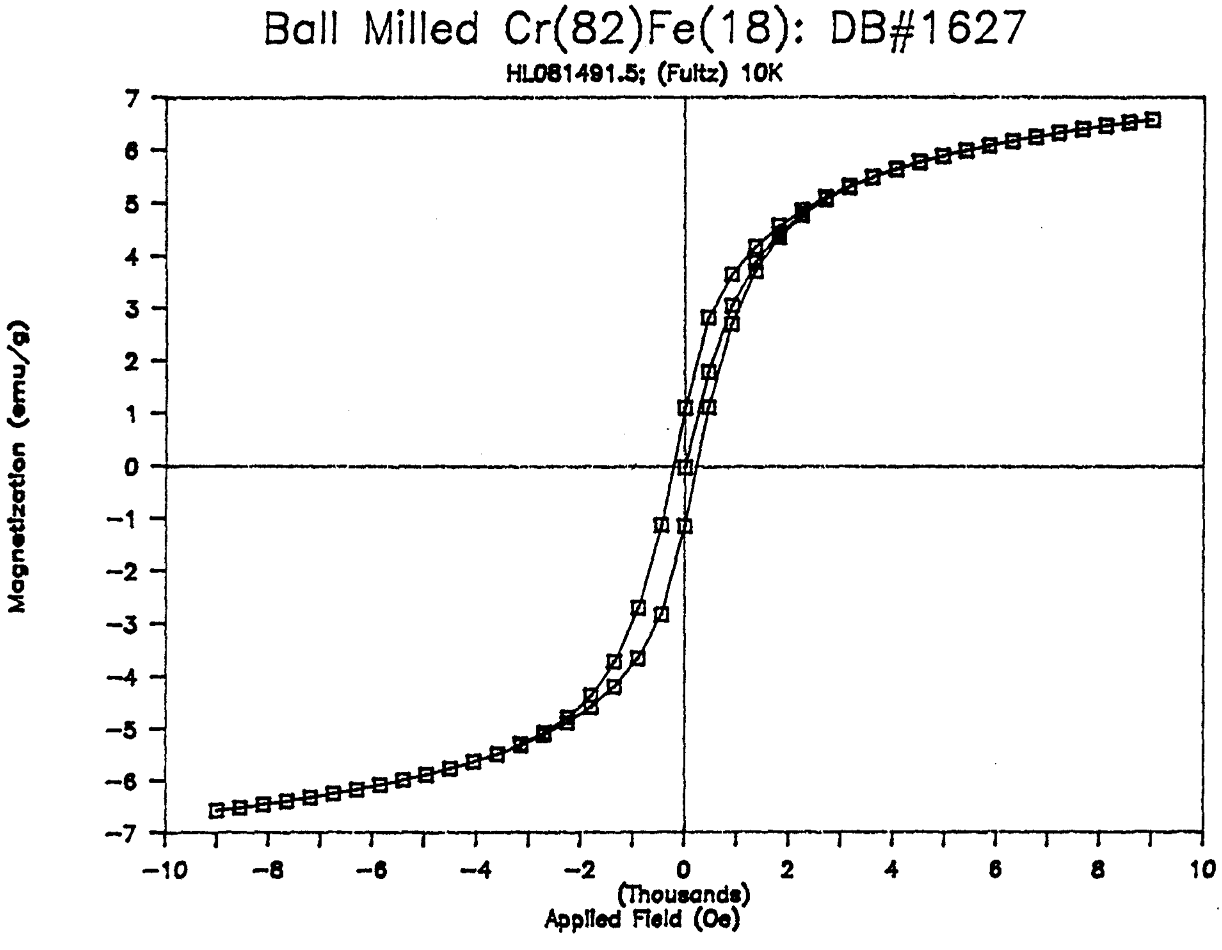

Figure B.5. Magnetization curve of nanophase Cr-Fe at 10 K.

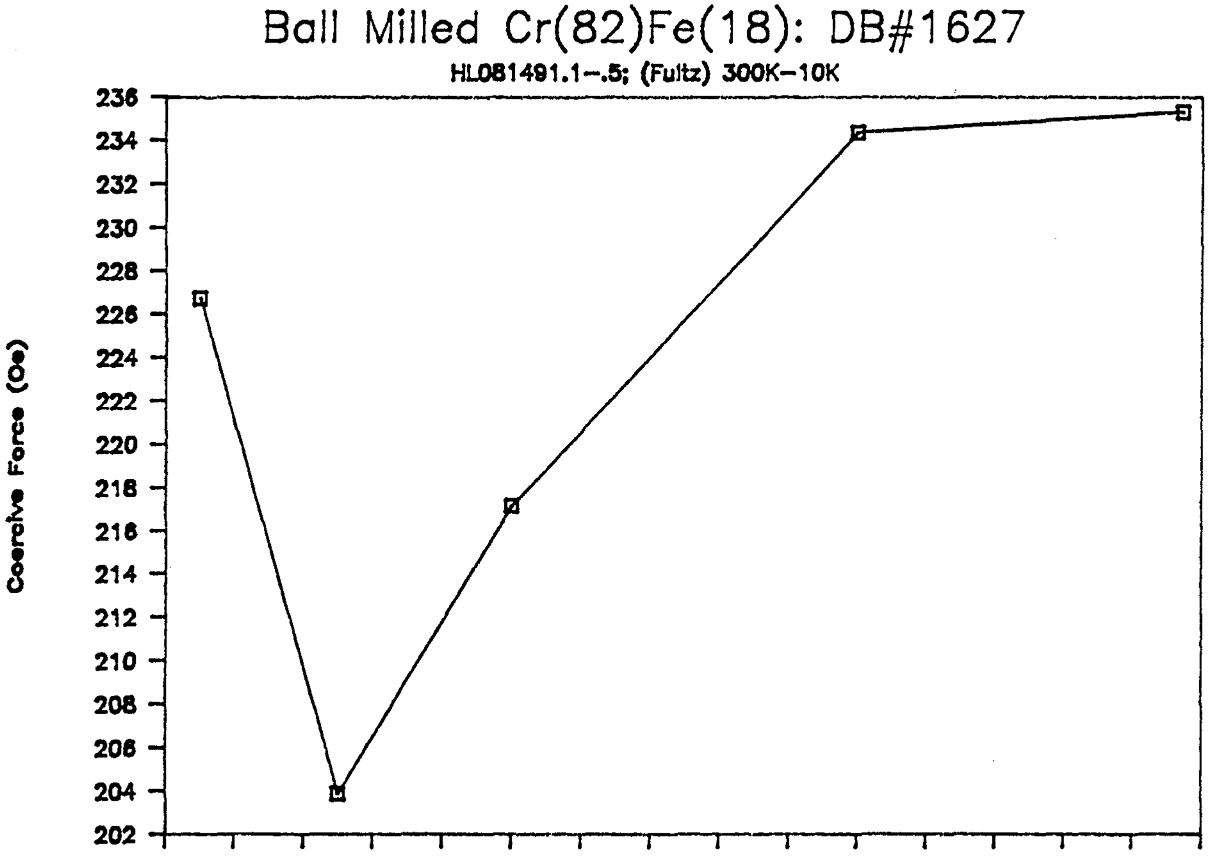

Figure B.6. Temperature dependence of coercive force for nanophase Cr-Fe.

Appendix C Monte Carlo Simulations

Enclosed is the program which was used to generate the lattice described in chapter 5.

```
        program dist

c       This program simulated to calculate the grain boundary fraction up to
c       9th nearest-neighbor and grain size distribution.

        include 'dist9nn.cub'

        integer*4 i, j

        call user_input
      call srand(seed)
c       call pgbegin(0, '?', 1, 1)
c       call pgask(.false.)
c       call pgupdt(0)

       open(12, file='dist9nn.dat')
        call randomize

c       call update(0)

        do i = 1, n_mcs
                do j = 1, (10 * total_atoms)
                        call grow
                enddo

        enddo

       call update(n_mcs)
c       call pgend

      close(12)
        end

        subroutine user_input

        include      'dist9nn.cub'

c     1nn

      nn_x(1) = 1
      nn_y(1) = 0
      nn_z(1) = 0
```

```
      nn_x(2) = 0
      nn_y(2) = 1
      nn_z(2) = 0
      nn_x(3) = 0
      nn_y(3) = 0
      nn_z(3) = 1
      nn_x(4) =-1
      nn_y(4) = 0
      nn_z(4) = 0
      nn_x(5) = 0
      nn_y(5) =-1
      nn_z(5) = 0
      nn_x(6) = 0
      nn_y(6) = 0
      nn_z(6) =-1

c     2nn

      nn_x(7) = 1
      nn_y(7) = 0
      nn_z(7) = 1
      nn_x(8) = 1
      nn_y(8) = 0
      nn_z(8) =-1
      nn_x(9) =-1
      nn_y(9) = 0
      nn_z(9) = 1
      nn_x(10)=-1
      nn_y(10)= 0
      nn_z(10)=-1
      nn_x(11)= 1
      nn_y(11)= 1
      nn_z(11)= 0
      nn_x(12)=-1
      nn_y(12)= 1
      nn_z(12)= 0
      nn_x(13)= 1
      nn_y(13)=-1
      nn_z(13)= 0
      nn_x(14)=-1
      nn_y(14)=-1
      nn_z(14)= 0
      nn_x(15)= 0
      nn_y(15)= 1
      nn_z(15)= 1
      nn_x(16)= 0
```

```
      nn_y(16)=-1
      nn_z(16)= 1
      nn_x(17)= 0
      nn_y(17)= 1
      nn_z(17)=-1
      nn_x(18)= 0
      nn_y(18)=-1
      nn_z(18)=-1

c     3nn

      nn_x(19)= 1
      nn_y(19)= 1
      nn_z(19)= 1
      nn_x(20)= 1
      nn_y(20)= 1
      nn_z(20)=-1
      nn_x(21)=-1
      nn_y(21)= 1
      nn_z(21)= 1
      nn_x(22)=-1
      nn_y(22)= 1
      nn_z(22)=-1
      nn_x(23)= 1
      nn_y(23)=-1
      nn_z(23)= 1
      nn_x(24)= 1
      nn_y(24)=-1
      nn_z(24)=-1
      nn_x(25)=-1
      nn_y(25)=-1
      nn_z(25)= 1
      nn_x(26)=-1
      nn_y(26)=-1
      nn_z(26)=-1

c     4nn

      nn_x(27)= 2
      nn_y(27)= 0
      nn_z(27)= 0
      nn_x(28)=-2
      nn_y(28)= 0
      nn_z(28)= 0
      nn_x(29)= 0
      nn_y(29)= 2
```

```
      nn_z(29)= 0
      nn_x(30)= 0
      nn_y(30)=-2
      nn_z(30)= 0
      nn_x(31)= 0
      nn_y(31)= 0
      nn_z(31)= 2
      nn_x(32)= 0
      nn_y(32)= 0
      nn_z(32)=-2

c     5nn

      nn_x(33)= 2
      nn_y(33)= 1
      nn_z(33)= 0
      nn_x(34)= 2
      nn_y(34)= 0
      nn_z(34)= 1
      nn_x(35)= 1
      nn_y(35)= 2
      nn_z(35)= 0
      nn_x(36)=-2
      nn_y(36)= 1
      nn_z(36)= 0
      nn_x(37)=-2
      nn_y(37)= 0
      nn_z(37)= 1
      nn_x(38)=-1
      nn_y(38)= 2
      nn_z(38)= 0
      nn_x(39)= 2
      nn_y(39)=-1
      nn_z(39)= 0
      nn_x(40)= 2
      nn_y(40)= 0
      nn_z(40)=-1
      nn_x(41)= 1
      nn_y(41)=-2
      nn_z(41)= 0
      nn_x(42)=-2
      nn_y(42)=-1
      nn_z(42)= 0
      nn_x(43)=-2
      nn_y(43)= 0
      nn_z(43)=-1
```

```
      nn_x(44)=-1
      nn_y(44)=-2
      nn_z(44)= 0
      nn_x(45)= 1
      nn_y(45)= 0
      nn_z(45)= 2
      nn_x(46)= 0
      nn_y(46)= 1
      nn_z(46)= 2
      nn_x(47)= 0
      nn_y(47)= 2
      nn_z(47)= 1
      nn_x(48)=-1
      nn_y(48)= 0
      nn_z(48)= 2
      nn_x(49)= 0
      nn_y(49)=-1
      nn_z(49)= 2
      nn_x(50)= 0
      nn_y(50)=-2
      nn_z(50)= 1
      nn_x(51)= 1
      nn_y(51)= 0
      nn_z(51)=-2
      nn_x(52)= 0
      nn_y(52)= 1
      nn_z(52)=-2
      nn_x(53)= 0
      nn_y(53)= 2
      nn_z(53)=-1
      nn_x(54)=-1
      nn_y(54)= 0
      nn_z(54)=-2
      nn_x(55)= 0
      nn_y(55)=-1
      nn_z(55)=-2
      nn_x(56)= 0
      nn_y(56)=-2
      nn_z(56)=-1

c     6nn

      nn_x(57)= 2
      nn_y(57)= 1
      nn_z(57)= 1
      nn_x(58)=-2
```

```
nn_y(58)= 1
nn_z(58)= 1
nn_x(59)= 2
nn_y(59)=-1
nn_z(59)= 1
nn_x(60)= 2
nn_y(60)= 1
nn_z(60)=-1
nn_x(61)=-2
nn_y(61)=-1
nn_z(61)= 1
nn_x(62)=-2
nn_y(62)= 1
nn_z(62)=-1
nn_x(63)= 2
nn_y(63)=-1
nn_z(63)=-1
nn_x(64)=-2
nn_y(64)=-1
nn_z(64)=-1
nn_x(65)= 1
nn_y(65)= 2
nn_z(65)= 1
nn_x(66)=-1
nn_y(66)= 2
nn_z(66)= 1
nn_x(67)= 1
nn_y(67)=-2
nn_z(67)= 1
nn_x(68)= 1
nn_y(68)= 2
nn_z(68)=-1
nn_x(69)=-1
nn_y(69)=-2
nn_z(69)= 1
nn_x(70)=-1
nn_y(70)= 2
nn_z(70)=-1
nn_x(71)= 1
nn_y(71)=-2
nn_z(71)=-1
nn_x(72)=-1
nn_y(72)=-2
nn_z(72)=-1
nn_x(73)= 1
nn_y(73)= 1
```

```
      nn_z(73)= 2
      nn_x(74)=-1
      nn_y(74)= 1
      nn_z(74)= 2
      nn_x(75)= 1
      nn_y(75)=-1
      nn_z(75)= 2
      nn_x(76)= 1
      nn_y(76)= 1
      nn_z(76)=-2
      nn_x(77)=-1
      nn_y(77)=-1
      nn_z(77)= 2
      nn_x(78)=-1
      nn_y(78)= 1
      nn_z(78)=-2
      nn_x(79)= 1
      nn_y(79)=-1
      nn_z(79)=-2
      nn_x(80)=-1
      nn_y(80)=-1
      nn_z(80)=-2

c     7nn

      nn_x(81)= 2
      nn_y(81)= 2
      nn_z(81)= 0
      nn_x(82)= 0
      nn_y(82)= 2
      nn_z(82)= 2
      nn_x(83)= 2
      nn_y(83)= 0
      nn_z(83)= 2
      nn_x(84)=-2
      nn_y(84)= 2
      nn_z(84)= 0
      nn_x(85)= 0
      nn_y(85)=-2
      nn_z(85)= 2
      nn_x(86)=-2
      nn_y(86)= 0
      nn_z(86)= 2
      nn_x(87)= 2
      nn_y(87)=-2
      nn_z(87)= 0
```

```
      nn_x(88)= 0
      nn_y(88)= 2
      nn_z(88)=-2
      nn_x(89)= 2
      nn_y(89)= 0
      nn_z(89)=-2
      nn_x(90)=-2
      nn_y(90)=-2
      nn_z(90)= 0
      nn_x(91)= 0
      nn_y(91)=-2
      nn_z(91)=-2
      nn_x(92)=-2
      nn_y(92)= 0
      nn_z(92)=-2

c     8nn

      nn_x(93)= 1
      nn_y(93)= 2
      nn_z(93)= 2
      nn_x(94)=-1
      nn_y(94)= 2
      nn_z(94)= 2
      nn_x(95)= 1
      nn_y(95)=-2
      nn_z(95)= 2
      nn_x(96)= 1
      nn_y(96)= 2
      nn_z(96)=-2
      nn_x(97)=-1
      nn_y(97)=-2
      nn_z(97)= 2
      nn_x(98)=-1
      nn_y(98)= 2
      nn_z(98)=-2
      nn_x(99)= 1
      nn_y(99)=-2
      nn_z(99)=-2
      nn_x(100)=-1
      nn_y(100)=-2
      nn_z(100)=-2
      nn_x(101)= 3
      nn_y(101)= 0
      nn_z(101)= 0
      nn_x(102)= 0
```

```
nn_y(102)= 0
nn_z(102)= 3
nn_x(103)= 2
nn_y(103)= 1
nn_z(103)= 2
nn_x(104)=-2
nn_y(104)= 1
nn_z(104)= 2
nn_x(105)= 2
nn_y(105)=-1
nn_z(105)= 2
nn_x(106)= 2
nn_y(106)= 1
nn_z(106)=-2
nn_x(107)=-2
nn_y(107)=-1
nn_z(107)= 2
nn_x(108)=-2
nn_y(108)= 1
nn_z(108)=-2
nn_x(109)= 2
nn_y(109)=-1
nn_z(109)=-2
nn_x(110)=-2
nn_y(110)=-1
nn_z(110)=-2
nn_x(111)=-3
nn_y(111)= 0
nn_z(111)= 0
nn_x(112)= 0
nn_y(112)= 0
nn_z(112)=-3
nn_x(113)= 2
nn_y(113)= 2
nn_z(113)= 1
nn_x(114)=-2
nn_y(114)= 2
nn_z(114)= 1
nn_x(115)= 2
nn_y(115)=-2
nn_z(115)= 1
nn_x(116)= 2
nn_y(116)= 2
nn_z(116)=-1
nn_x(117)=-2
nn_y(117)=-2
```

```
      nn_z(117)= 1
      nn_x(118)=-2
      nn_y(118)= 2
      nn_z(118)=-1
      nn_x(119)= 2
      nn_y(119)=-2
      nn_z(119)=-1
      nn_x(120)=-2
      nn_y(120)=-2
      nn_z(120)=-1
      nn_x(121)= 0
      nn_y(121)= 3
      nn_z(121)= 0
      nn_x(122)= 0
      nn_y(122)=-3
      nn_z(122)= 0

c     9nn

      nn_x(123)= 3
      nn_y(123)= 1
      nn_z(123)= 0
      nn_x(124)= 3
      nn_y(124)= 0
      nn_z(124)= 1
      nn_x(125)= 1
      nn_y(125)= 3
      nn_z(125)= 0
      nn_x(126)= 1
      nn_y(126)= 0
      nn_z(126)= 3
      nn_x(127)= 0
      nn_y(127)= 1
      nn_z(127)= 3
      nn_x(128)= 0
      nn_y(128)= 3
      nn_z(128)= 1
      nn_x(129)=-3
      nn_y(129)= 1
      nn_z(129)= 0
      nn_x(130)=-3
      nn_y(130)= 0
      nn_z(130)= 1
      nn_x(131)=-1
      nn_y(131)= 3
      nn_z(131)= 0
```

```
nn_x(132)=-1
nn_y(132)= 0
nn_z(132)= 3
nn_x(133)= 0
nn_y(133)=-1
nn_z(133)= 3
nn_x(134)= 0
nn_y(134)=-3
nn_z(134)= 1
nn_x(135)= 3
nn_y(135)=-1
nn_z(135)= 0
nn_x(136)= 3
nn_y(136)= 0
nn_z(136)=-1
nn_x(137)= 1
nn_y(137)=-3
nn_z(137)= 0
nn_x(138)= 1
nn_y(138)= 0
nn_z(138)=-3
nn_x(139)= 0
nn_y(139)= 1
nn_z(139)=-3
nn_x(140)= 0
nn_y(140)= 3
nn_z(140)=-1
nn_x(141)=-3
nn_y(141)=-1
nn_z(141)= 0
nn_x(142)=-3
nn_y(142)= 0
nn_z(142)=-1
nn_x(143)=-1
nn_y(143)=-3
nn_z(143)= 0
nn_x(144)=-1
nn_y(144)= 0
nn_z(144)=-3
nn_x(145)= 0
nn_y(145)=-1
nn_z(145)=-3
nn_x(146)= 0
nn_y(146)=-3
nn_z(146)=-1
```

```
  write (*,*) 'seed the random number'
  read (*,*) seed

  nn=6

  write (*,*) 'enter n_seed'
  read (*,*) n_seed

  return

  end

  subroutine randomize

  include 'dist9nn.cub'

integer*4 i
real*8 rand,s
real*4 rxl,ryl,rzl,sx,sy,sz
 integer*4 orient
  do x = 0, xlim - 1
          do y = 0, ylim - 1
        do z= 0, zlim - 1

       xtal(x,y,z)=100
        xtal_check(x,y,z)=xtal(x,y,z)

       enddo

          enddo
  enddo

do i=1, n_seed

  rxl=xlim-1
  ryl=ylim-1
  rzl=zlim-1

   sx=xlim*rand()
  sy=ylim*rand()
   sz=zlim*rand()

  x=min1(sx, rxl)
  y=min1(sy, ryl)
```

```
  z=min1(sz, rzl)

   s=n_orient*rand()+1
    orient=min1(s,real(n_orient))
  xtal(x,y,z)=orient

enddo

  return

  end


  subroutine grow

  include 'dist9nn.cub'

  integer*4 i
real*8 rand,sx,sy,sz

real*4 rxl,ryl,rzl

 real*4 modx(6),mody(6),modz(6)
rxl=xlim-1
ryl=ylim-1
rzl=zlim-1

sx=xlim*rand()
sy=ylim*rand()
sz=zlim*rand()

  x = min1(sx, rxl)
  y = min1(sy, ryl)
z = min1(sz, rzl)

  do i = 1, nn

    modx(i)=mod(x+nn_x(i)+xlim,xlim)
   mody(i)=mod(y+nn_y(i)+ylim,ylim)
    modz(i)=mod(z+nn_z(i)+zlim,zlim)

 if (xtal(x,y,z) .eq. 100) then

   goto 66

 endif
```

```
    if (xtal(modx(i),mody(i),modz(i)) .eq. 100) then

      xtal(modx(i),mody(i),modz(i))=xtal(x, y, z)

    endif

  enddo

66   return

    end

    subroutine update(mcs)

    include 'dist9nn.cub'

    integer*4 mcs, ns(100), nst

  real*4 tr, mr

    integer*4 nyz,ni,i, j, k, l, n1, n2, n3

   integer*4 n, n_liquid, n_gb

   integer*4 modx(0:xlim-1), m1(146),m2(146),m3(146)

  do i=1, 100
    ns(i)=0
  enddo

  do nyz=0, ylim-1

  ni = 0
  n = 1

100  if (ni .eq. xlim-1) then

    goto 200

  endif


    modx(ni)=mod(ni+1+xlim,xlim)
  if (xtal(ni,nyz,nyz) .ne. xtal(modx(ni),nyz,nyz)) then
```

```
         ns(n)=ns(n)+1
        n =1

      endif

       if (xtal(ni,nyz,nyz) .eq. xtal(modx(ni),nyz,nyz)) then

          n=n+1

      endif

       ni=ni+1

      goto 100

200   enddo

       n_liquid=0
      n_gb=0

      do i= 0, xlim-1
         do j=0, ylim-1
           do k=0, zlim-1

            if (xtal(i,j,k) .eq. 100) then

               n_liquid=n_liquid+1

            endif

             do l=1, 146

                m1(l)=mod(i+nn_x(l)+xlim,xlim)
                m2(l)=mod(j+nn_y(l)+ylim,ylim)
                m3(l)=mod(k+nn_z(l)+zlim,zlim)

               if (xtal(i,j,k) .ne. xtal(m1(l),m2(l),m3(l))) then

                xtal_check(i,j,k)=0

              endif
             enddo

              if (xtal_check(i,j,k) .eq. 0) then
               n_gb=n_gb+1
```

```
      endif


    enddo
  enddo
enddo

nst=0
tr=0.0

do i=1,100

   nst=nst+ns(i)

   write(12,*) 'i=',i,' ','ns=',ns(i)
 tr=tr+i*ns(i)

enddo

mr=tr/nst

   write(12,*) 'n_liquid=',n_liquid,' ','n_gb=',n_gb
   write(12,*) 'mean radius=',mr,' ','n_seed=',n_seed

do n1=0, xlim-1
  do n2=0, ylim-1
    do n3=0, zlim-1

      xtal_check(n1,n2,n3)=1

    enddo
  enddo
enddo

  return

  end
```

Appendix D Phase diagrams

This appendix includes the equilibrium phase diagrams of Cr-Fe, Fe-Ti, Ni-Fe and Fe-Mn (1).

Cr-Fe

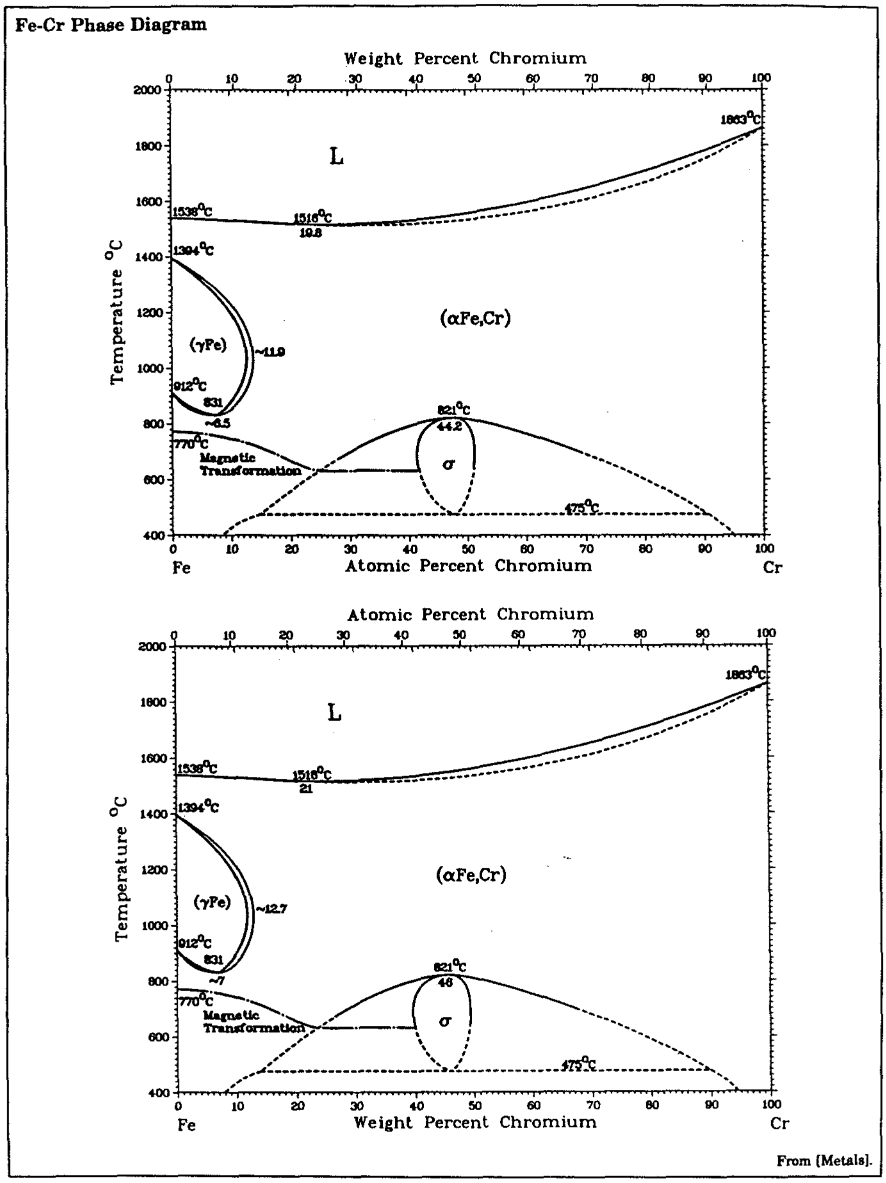

From [Metals].

Binary Alloy Phase Diagrams

Figure D.1. The phase diagram of Cr-Fe.

Fe-Ti

Assessed Ti-Fe Phase Diagram

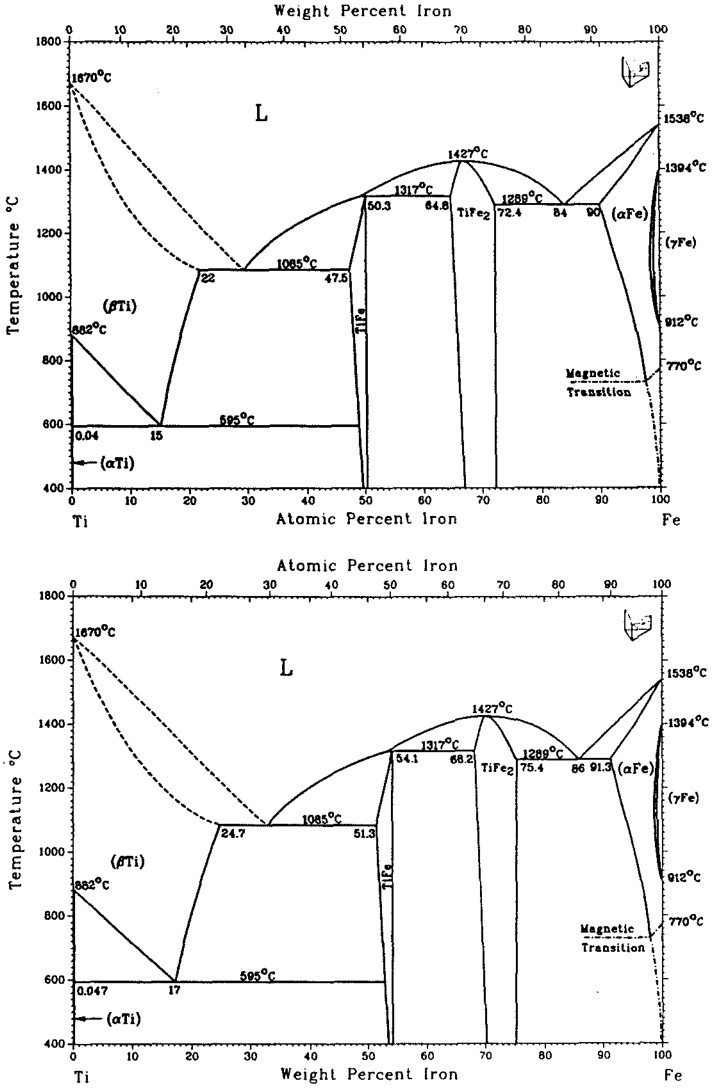

J.L. Murray, submitted to the APD Program.

Binary Alloy Phase Diagrams

Figure D.2. The phase diagram of Fe-Ti.

Fe-Ni

Fe-Ni Phase Diagram

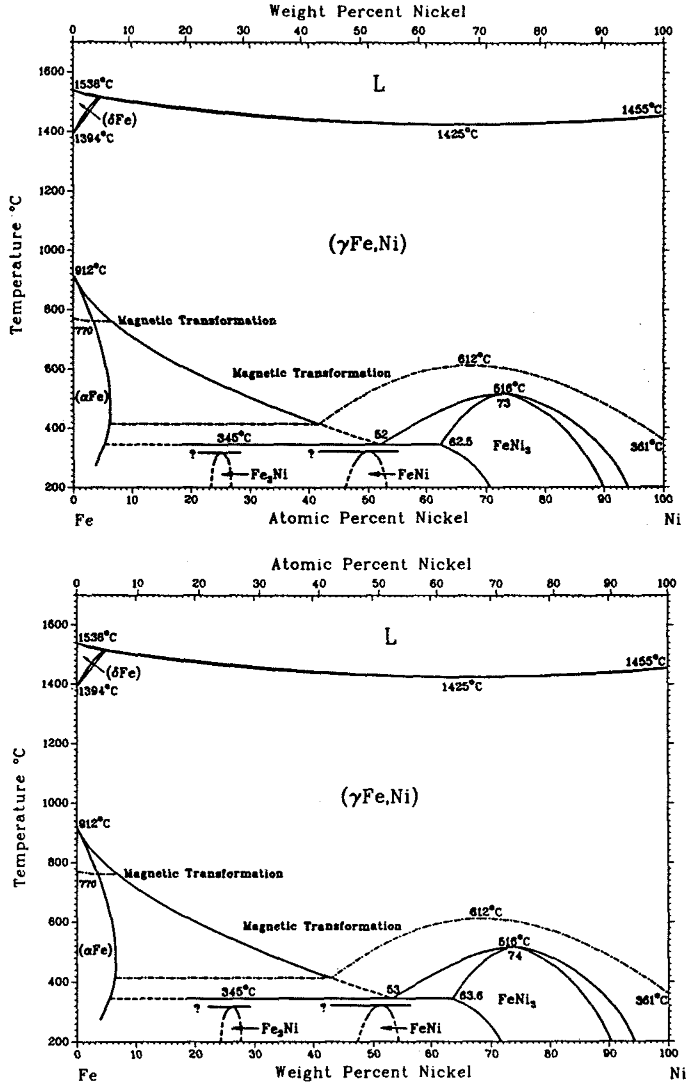

From [Kubaschewski].

Binary Alloy Phase Diagrams

Figure D.3. The phase diagram of Ni-Fe.

Fe-Mn

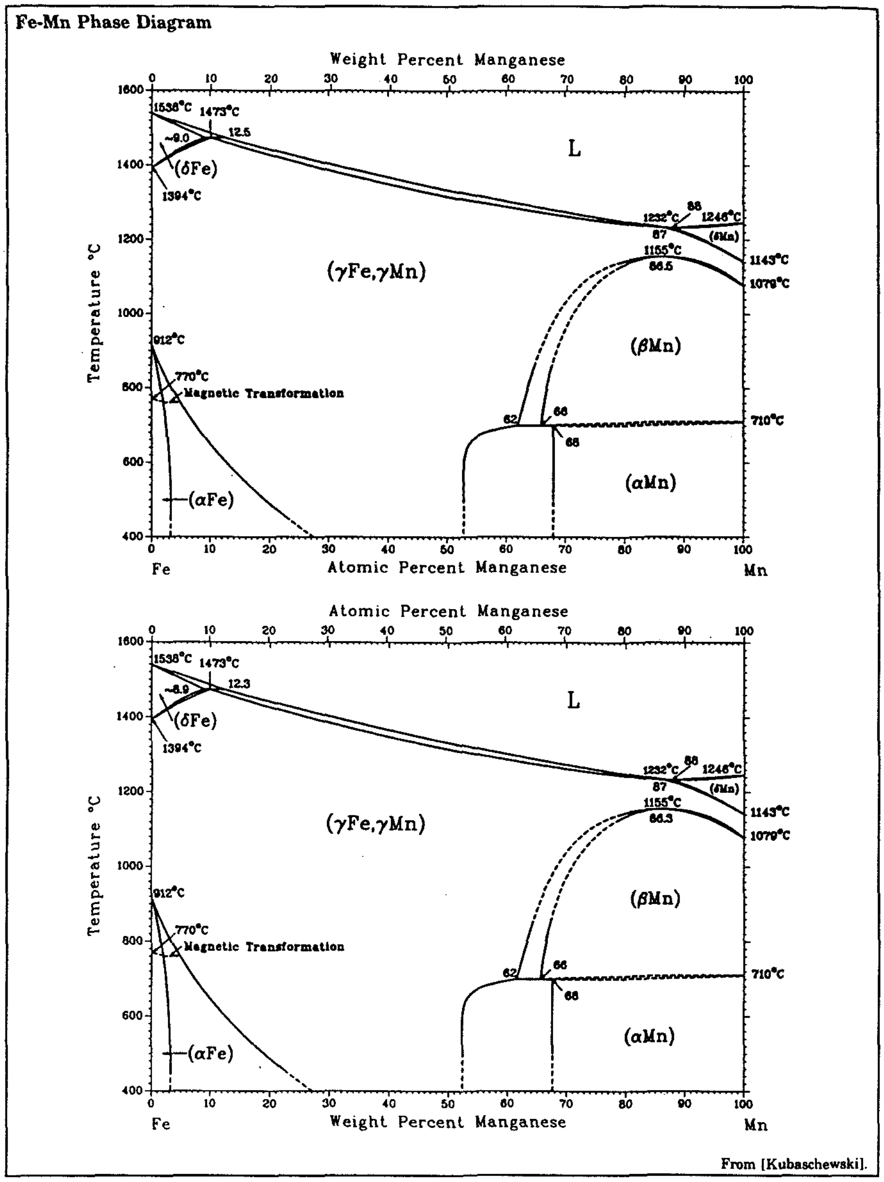

Fe-Mn Phase Diagram

From [Kubaschewski].

Binary Alloy Phase Diagrams

Figure D.4. The phase diagram of Fe-Mn.

Reference

1. Editor Thaddeus B. Massalski, Binary Alloy Phase Diagrams (American Society for Metals, Metal Park, Ohio 44073, 1986).